



Smith, Aimee (2018) *Volatile elements in Martian apatite: Insights from new meteorites NWA 7034 and NWA 8159*. MSc(R) thesis.

<https://theses.gla.ac.uk/8968/>

Copyright and moral rights for this work are retained by the author

A copy can be downloaded for personal non-commercial research or study, without prior permission or charge

This work cannot be reproduced or quoted extensively from without first obtaining permission in writing from the author

The content must not be changed in any way or sold commercially in any format or medium without the formal permission of the author

When referring to this work, full bibliographic details including the author, title, awarding institution and date of the thesis must be given

Enlighten: Theses

<https://theses.gla.ac.uk/>
research-enlighten@glasgow.ac.uk

**Volatile Elements in Martian Apatite:
Insights from New Meteorites NWA 7034
and NWA 8159**

Aimee Smith

2028320

Submitted in fulfilment of the requirements for the Degree
of Masters in Science by Research MSc(R)



School of Geographical and Earth Sciences
College of Science and Engineering
University of Glasgow

April, 2018

© Aimee Smith, 2018

Abstract

Measurements of volatile abundances at the martian surface (e.g. H₂O, Cl, CO₂, CH₄) are a priority for the latest generation of martian rovers (*Curiosity* and *ExoMars*) due to the astrobiological importance of these compounds. Mars is a prime candidate to find water as recent Mars orbiter and lander missions have revealed evidence for the presence of liquid water early in Mars's history (e.g., Nochian ~3.9 to 4.5 Ga). Geomorphological features (e.g., fluvial valleys), water rich sediments and minerals (e.g. clays) and evaporates (e.g. gypsum) all indicate hydrological activity has occurred on Mars. However, rovers are limited to surface exploration and therefore are unable to provide insight to the volatile content of the martian interior. Martian meteorites identified on Earth consist largely of volcanic basaltic material. Therefore, the volatile contents of primary igneous minerals within these martian basalts can indicate the volatile content of the source regions at depth in the martian interior.

The discovery of Northwest Africa (NWA) 7034 (and pairings) and NWA 8159 has expanded the diversity of the martian meteorites from the common Shergottite, Nakhlite, Chassignite (SNC) types observed. NWA 7034 is a polymict basaltic breccia, whereas NWA 8159 is an augite basalt. This study investigates the apatite volatile content of these two unique martian meteorites.

The apatite volatile content in NWA 8159 relates to the volatile abundances of the parental melt, hence providing insight into a previously unstudied martian volcanic province. The discovery of F-rich apatites in NWA 8159 in this study is a particularly important find since F-rich apatites, are not characteristic of martian meteorites, which typically have Cl-rich apatite compositions. This rare finding along with previous F-rich apatite discoveries (Slaby et al., 2016, 2017) highlights that a F-rich source region for martian magma is present. This F-rich parental source region has, until recently, been unstudied due to the sample bias in the martian meteorite suite.

Results from this study confirm the presence of more Mars typical Cl-rich apatites within NWA 7034 and reveal a significant OH component within individual apatite grains. The volatile content of NWA 7034 is in fact uncharacteristically uniform for a polymict breccia (i.e., no groupings of apatite can be seen in terms of

their volatile abundances (Cl: F: OH)), indicating post-crystallisation processes—possibly a thermal event have overprinted the original Cl, F and OH contents of these apatite grains.

Three distinct groupings of apatites can be noted on the basis of hydrogen isotope composition, water content and texture of NWA 7034 apatite. This implies that there are at least two different apatite histories that have been recorded. Group 1 is characterised by high δD values paired with low water contents, and inferred to be the result of devolatilisation during shock and/or thermal heating. Group 2 consists of intermediate δD values and high water contents, which could be controlled by hydrothermal alteration. Group 3 is characterised by low δD values and high water contents, probably caused by terrestrial contamination, but possibly representative of a martian mantle signature.

Acknowledgments

I would firstly like to thank Professor Martin Lee for offering me the opportunity to undertake this research masters. I would also like to thank my supervisor, Dr. Lydia Hallis for being so informative and helpful throughout my masters. It's greatly appreciated, I learned a lot!

Thanks also to Peter Chung for providing SEM time and expertise at the ISAAC Facility University of Glasgow and to Dr. Tobais Slage at the Natural History Museum, London, for giving up your time to collaborate.

I would like to express my gratitude to two funding bodies: The PhD Mobility Scholarship and The Michael Golden Fund who awarded me with the funds to conduct hydrogen isotope analysis at the University of Hawaii.

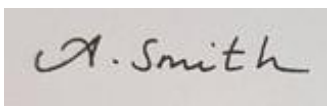
Many thanks goes to Professor Gary Huss and Dr. Kazu Nagashima at the W. M. Keck Cosmochemistry Laboratory at the University of Hawaii, for providing instrument time and expertise on hydrogen isotope analysis, it was much appreciated and a great experience!

I would also like to thank Shazia Ali for giving me her brains through osmosis in higher physics. Without her kind gift, I would never have achieved what I have today.

Last but certainly not least, I would like to give a special thanks to Benjamin Ellan Farrant for initially urging me to take on this research masters (despite my cabbageness) and providing his unwavering support throughout this year. Thanks for keeping me less stressed by saying it's only a masters, no biggie. If I ever let you read this don't point out any mistakes!

Author's Declaration

I declare that this thesis, except where acknowledged to others, represents my own work carried out in the School of Geographical and Earth Sciences, University of Glasgow. The research presented here has not been submitted for any other degree at the University of Glasgow, nor at any other institution. Any published or unpublished work by other authors has been given full acknowledgment in the text.

A rectangular box containing a handwritten signature in black ink that reads "A. Smith".

Aimee Smith

Definitions and Abbreviations

Al	Aluminium
ALH	Alan Hills
An	Anorthite
Ar	Argon
BSE	Backscatter electron
Ca	Calcium
$\text{Ca}_5(\text{PO}_4)_3(\text{F}, \text{Cl}, \text{OH})$	Calcium phosphate apatite chemical formula
Cl	Chlorine
cps	Counts per second
Cs	Caesium
EDS	Energy-dispersive X-ray Analysis
EET	Elephant Moraine
D	Deuterium
D/H	Deuterium/Hydrogen ratio (hydrogen isotope composition)
F	Fluorine
Fa	Fayalite
Fe	Iron
$f\text{O}_2$	Oxygen fugacity
Fs	Ferrosilite
g	Grams
Ga	Billion years ago
GPa	Gigapascals
H	Hydrogen
In	Indium
ISAAC	Imaging Spectroscopy and Analysis Centre
K	Potassium
kbar	Kilobar
kV	Kilovolts
HED's	Howardites, Eucrites and Diogenites meteorites

H ₂ O	Water
Ma	Million years ago
Mg	Magnesium
Mn	Manganese
nA	Nano amps
Na	Sodium
N/A	Not applicable
Nd	Neodymium
nM	Nanometres
NWA	Northwest Africa
NWA 7034(Epoxy)	Northwest Africa 7034 mounted in epoxy
NWA 7034(In)	Northwest Africa 7034 mounted in indium
O	Oxygen
OH	Hydroxyl
-O=F	Oxygen equivalent for fluorine
-O=Cl	Oxygen equivalent for chlorine
P	Phosphorous
Pb	Lead
ppm (‰)	Parts per million
ROI	Region of interest
Rb	Rubidium
REE	Rare Earth Elements
RVA	Relative Volatile Abundance
s	Seconds
S	Sulphur
SEM	Scanning Electron Microscopy
SHRIMP	Sensitive High Resolution Ion Microprobe
Si	Silicon
SiC	Silicon Carbide
SIMS	Secondary Ion Mass Spectrometer
Sm	Samarium
SNC	Shergottite, Nakhlite, Chassignite martian meteorites

Sr	Strontium
Std run	Standard run
Ti	Titanium
U	Uranium
UH	University of Hawaii
UoG	University of Glasgow
VSMOW	Vienna Standard Mean Ocean Water
WD	Working distance
wt. %	Weight percent
Z	Atomic number
δ / Δ	Delta
μm	Microns

Contents

Abstract	1
Acknowledgments.....	3
Author's Declaration.....	4
Definitions and Abbreviations	5
Chapter 1 Introduction	19
1.1 Introduction to the Project.....	19
1.2 Introduction to Martian Meteorites	20
1.2.1 Martian Origin.....	21
1.2.2 Shergottite, Nakhlite, Chassignite Martian Meteorites	23
1.2.2.1 Shergottites.....	24
1.2.2.2 Nakhrites	24
1.2.2.3 Chassignites	25
1.2.3 Martian Orthopyroxenite ALH 84001	25
1.2.4 Northwest Africa (NWA) 7034.....	26
1.2.5 Northwest Africa (NWA) 8159.....	29
1.3 Introduction to Apatite	30
1.3.1 Structure of Apatite.....	30
1.3.2 Volatile Content within Martian Apatite	31
1.3.3 Volatile Content within Apatite in NWA 7034	32
1.3.4 Determining Volatile Abundances of Parental Magma from Apatite.....	34
1.4 Introduction to Hydrogen Isotopes (Deuterium/Hydrogen Ratios)	35
1.4.1 Martian Water Reservoirs	35
1.5 Project Aims and Objectives	38
Chapter 2 Methodology.....	41
2.1 Preparation of Samples.....	41
2.2 Scanning Electron Microscopy (SEM).....	41
2.2.1 Scanning Electron Microscopy- Backscatter Imaging.....	42
2.2.2 Energy-Dispersive X0ray Analysis (EDS) - Imaging.....	42
2.2.3 Energy-Dispersive X-ray Analysis (EDS)- Quantitative Chemical Analysis.....	44
2.3 Problems with Measuring Volatiles	44
2.3.1 Fluorine Migration	44
2.3.2 Scanning Electron Microscopy at the Natural History Museum	45

2.3.3 Stoichiometry Calculations of Volatile Abundances	46
2.4 Cameca ims 1280 Ion Microprobe	48
2.4.1 Secondary Ion Mass Spectrometry- Analytical Protocol	48
Chapter 3 Volatile Abundance Apatite Data.....	55
3.1 Volatile Content within Apatite in NWA 7034.....	55
3.1.1 Targeted Apatites for Volatile Abundance Analysis	61
3.1.2 Plotted Volatile Abundances for Stoichiometry Calculated OH Component.....	65
3.2 Volatile Content within Apatite in NWA 8159	70
3.2.1 Apatites in NWA 8159.....	70
3.2.2 Volatile Abundances from Triplot Data.....	73
Chapter 4 Hydrogen Isotope Data.....	77
4.1 Deuterium/Hydrogen Ratios from NWA 8159	77
4.2 NWA 7034 Targets for Hydrogen Isotope Analysis.....	77
4.2.1 Pit Images from Targeted Apatites	80
4.2.2 Pit Images from Anhydrous Minerals	89
4.3 NWA 7034 Hydrogen Isotope Results.....	91
4.3.1 Measured OH Component for Volatile Abundance Triplot.....	91
4.3.2 Cameca ims 1280 Hydrogen Isotope Analyses.....	93
Chapter 5 Discussion	96
5.1 Volatile Abundances in NWA 7034.....	96
5.2 Volatile Abundances in NWA 8159	97
5.3 Hydrogen Isotope Results from NWA 7034	98
5.3.1 Factors Affecting Deuterium/Hydrogen Ratios	98
5.3.2 Apatite Groupings	98
5.3.3 Effect of Terrestrial Contamination	102
5.3.4 Deuterium/Hydrogen Values from Anhydrous Minerals in NWA 7034.....	102
Chapter 6 Conclusions	103
6.1 Summary	103
6.2 Future Work	104
6.2.1 Northwest Africa 7034.....	104
6.2.2 Northwest Africa 8159.....	105
References	106

List of Figures

- Figure 1: Ages of selected SNC martian meteorites and ungrouped martian meteorites. Shergottites in red, nakhlites in blue, Chassigny in green, ALH 84001 in black, NWA 7034 in purple and NWA 8159 in yellow (adapted from Papike et al., 2009).21
- Figure 2: Oxygen isotope values for the Earth-Moon system (indicated by the green circle), chondrites and the SNC meteorites (highlighted by red outline). The insert enlarges the region associated with the differentiated meteorites such as the HEDs (howardites, eucrites and diogenites) and the SNC meteorites (adapted from Lodders and Fegley, 1997).23
- Figure 3: Apatites were analysed by SHRIMP-RG for U-Pb dating on Cl-rich apatite in NWA 7034. The results are plotted on a Tera-Wasserburg Concordia diagram and give a date of 1.49 ± 0.09 Ga. Ellipses are 1 sigma errors on the measurements (dashed ellipses are not date measurements) (McCubbin et al., 2016).28
- Figure 4: The atomic structure of apatite. T sites are indicated in yellow; M1 in red; M2 in orange. Column anions (F, Cl and OH) are displayed in green (Hughes and Rakovan, 2015).31
- Figure 5: Volatile abundances of Cl, F and OH from martian and terrestrial apatites. Martian apatites tend to be Cl-rich and OH-poor. Outliers represent more fluorine rich apatites (Filiberto and Treiman, 2009).32
- Figure 6: Volatile abundances from apatite from clasts and the matrix of NWA 7034. Different coloured regions indicate different relative abundances of Cl, F and OH in the melt in which the apatites crystallised from. Green: Cl rich melt (Cl>OH>F), Blue: OH rich melt (OH>Cl>F), Light purple: OH rich melt (OH>F>Cl) and dark purple: F rich melt (F>Cl>OH) (Santos et al., 2013).33
- Figure 7: The hydrogen isotope (δD) values of solar system bodies and water reservoirs on Mars. It can be noted that the δD composition of chondrite bodies and the martian mantle is similar. Three distinct martian water reservoirs are displayed in this diagram: martian mantle, near surface water/ice and ground ice/hydrated crust (i.e., the intermediate reservoir) (Usui et al., 2015).36
- Figure 8: Proposed model from Usui et al., 2015 showing the location of the proposed intermediate water reservoir on Mars through cross sections. (a) Hydrated crust model and (b) Ground ice model. The hydrated crust model suggests that the intermediate reservoir is contained within hydrous sediments and minerals on the martian surface. Whereas, the ground ice model implies that the intermediate reservoir is contained within sediments interbedded with ground ice.38

Figure 9: The Carl Zeiss Sigma Variable Pressure Analytical Scanning Electron Microscope at the Imaging Spectroscopy and Analysis Centre (ISAAC) Facility, University of Glasgow.42

Figure 10: A schematic of the structure of an atom, indicating the nucleus and electron orbitals (K, L and M). Each orbital has a distinct energy level (i.e., K is an electron in ground state, which when excited by a beam, will become excited and move to a higher energy level (L or M)). Electrons from a higher energy level can fill in a vacancy when an electron from a lower energy level has been knocked from its orbital, which releases a characteristic X-ray. Adapted from Oxford labs (2017) and Robinson (2000).43

Figure 11: Schematic of the Cameca ims 1280 ion microprobe at the University of Hawaii. The main features of this ion microprobe are the sample chamber and air lock (purple); primary ion column (yellow); Secondary Ion Mass Spectrometer (green); detectors (blue) (HGIP, 2017). The sample chamber operates with a vacuum of $\sim 1 \times 10^{-9}$ torr and allows for one sample in the chamber at a time, and a reserve sample in the airlock. The SIMS detector is double focussing, with an electrostatic and magnetic sector in a forward geometry (i.e., the electrostatic sector is before the magnetic sector). This geometry allows for the reduction of energy of the secondary ions (via the electrostatic sector) prior to separation to single ion beams in the magnetic sector (Shimizu, 1997).50

Figure 12: A simplified schematic of the sputtering and rastering process, which occurs during analysis. The primary ion beam is rastered over a $25 \times 25 \mu\text{m}$ area for 200s to remove the carbon coating over the apatite and surface contamination (b), the raster area is then reduced to an area of $15 \times 15 \mu\text{m}$ (c) and then to an $8 \times 8 \mu\text{m}$ area for analysis (d).52

Figure 13: Calibration line for apatite in NWA 7034. The line is based on analysis of terrestrial standards with known water contents (table 11).54

Figure 14: Energy-dispersive X-ray analysis compositional map of NWA 7034 (indium mounted sample). Composition: Silica: blue, Magnesium: green and Iron: red. Bright green areas correspond to pyroxene, mostly present as large ($\sim 100\text{-}600 \mu\text{m}$) mono-mineralic clasts. Red areas represent magnetite, and blue areas are either plagioclase ($\sim 200\text{-}500 \mu\text{m}$) or silica rich glass produced via shock. Some of the various clast types present in NWA 7034 are displayed in the above figure: protobreccia clasts (yellow dashed line), melt clast (pink dashed line) and mineral clasts (plagioclase in the white dashed line and pyroxene in the light blue dashed line).56

Figure 15: Energy-dispersive X-ray analysis compositional map of NWA 7034 (epoxy mounted sample). Composition: Calcium: blue, Aluminium: green and Phosphorus: red. Bright blue areas correspond to pyroxene, present as $\sim 100\text{-}500 \mu\text{m}$ mono-mineralic clasts. Dark green areas are predominantly plagioclase, with large phenocrysts ranging from $\sim 200\text{-}300 \mu\text{m}$. Dark pink areas represent small apatite grains ($\sim 25 \mu\text{m}$). Various clast types present can be noted in the above figure: protobreccia clasts (yellow dashed line), a coarse

igneous clast (red dashed line) and mineral clasts (Pigeonite in the black dashed line, plagioclase in the white dashed line and pyroxene in the light blue dashed line).57

Figure 16: Energy-dispersive X-ray analysis compositional map of NWA 7034 (In). Composition: Phosphorous: red and chlorine: green. Apatite grains are highlighted in yellow due to the false colour overlay of phosphorus (red) and chlorine (green), two diagnostic elements that make up apatite.58

Figure 17: Energy-dispersive X-ray analysis compositional map of NWA 7034 (Epoxy). Composition: Phosphorous: red. Thus, red grains indicated in the EDS map are apatite....59

Figure 18: Energy-dispersive X-ray analysis compositional map of an apatite (ROI_1a) within NWA 7034 (Epoxy) showing signs of shock blackening (see black arrow). Composition: Chlorine: green, Phosphorous: purple, Iron: red, Calcium: orange, Silica: blue and Magnesium: yellow.60

Figure 19: Energy-dispersive X-ray analysis compositional Fe map of an apatite (ROI_1a) within NWA 7034 (Epoxy) showing signs of shock blackening. Lines of interest are iron rich.....60

Figure 20: BSE images of apatites of interest in NWA 7034 (In). Yellow dashes outline the grain boundary of the apatite to surrounding minerals and matrix material. Each apatite was selected as a “region of interest” (ROI). Spectrum labels indicate where previous SEM-EDS point analysis was conducted. (A) Highlights ROI_1 and 2 apatites contained within a pyroxene clast. The results of SEM-EDS analysis of ROI_2 are not displayed in the triplot below due to low overall totals (< 96%), however this apatite was selected for hydrogen isotope analysis.(B) Shows ROI_4, which is a free apatite grain within the matrix. (C) Highlights ROI_8, a euhedral, free apatite grain within the matrix. A prominent fracture is shown through the apatite, however the surface on either side is relatively clean. The results of SEM-EDS analysis of this apatite are not displayed in the triplot below due to low overall totals (< 96%), however this apatite was selected for hydrogen isotope analysis. (D) Indicates Std run 10, an anhedral free apatite grain. (E) Highlights Std run 11, a euhedral apatite positioned at the sample edge. (F) Shows Std run 12, an anhedral free apatite grain.62

Figure 21: BSE images of apatites of interest in NWA 7034 (Epoxy). Yellow dashes outline the grain boundary of the apatite to surrounding minerals and matrix material. Each apatite was selected as a “region of interest” (ROI). Spectrum labels indicate where previous SEM-EDS point analysis was conducted. (G) Highlights ROI_1a, a euhedral apatite grain with a prominent crack along the surface. Thin white veins can be seen on the surface of the apatites (previously explained in section 1.2.4). (H) shows ROI_2a, an anhedral free apatite grain within the matrix. (I) Highlights ROI_3, a prominent feature of this apatite is the fracture across the surface. White inclusions (possibly silicates) are present to the left side of the fracture, whereas the surface to the right side of the fracture

appears relatively clean. (J) Shows ROI_4a, an anhedral apatite that appears to have been broken up. (K) Highlights ROI_5, again this apatite as a dominant fracture, with silica inclusions present on both sides of the fracture. (L) Displays ROI_6a, an anhedral apatite grain within the matrix of NWA 7034.63

Figure 22: BSE images of apatites of interest in NWA 7034 (Epoxy). Yellow dashes outline the grain boundary of the apatite to surrounding minerals and matrix material. Each apatite was selected as a “region of interest” (ROI). Spectrum labels indicate where previous SEM-EDS point analysis was conducted. (M) Highlights ROI_7, a fractured anhedral apatite grain within the matrix. (N) Shows ROI_8a, a euhedral apatite located in the rim of a pigeonite mineral clast. (O)- (Q) Highlights ROI_11, 12 and 13. All euhedral free apatite grains within the matrix.....64

Figure 23: Plotted volatile abundances on a relative volatile abundance (RVA) diagram form apatites in NWA 7034. The values used in this plot (tables 5, 6 and 7) were calculated using stoichiometry methods previously discussed in section 2.3.3. The spreadsheet for this triplot can be viewed on the supplementary disk.66

Figure 24: RVA diagram showing NWA 7034 apatite data overlain with the spread of apatite data from Santos et al. (2013). The data from this study fits relatively well with Santos et al. (2013) data. However, apatites from this study plot predominantly in the green area of the triplot (Cl>OH>F), with a few minor apatites plotting in the blue area (OH>Cl>F melt).....70

Figure 25: Energy-dispersive X-ray analysis compositional map of NWA 8159. Composition: Phosphorous: red. The red grains indicated in the EDS map are apatite. Because this meteorite contains very small apatite (<20µm) it is hard to detect them. The red box in the figure indicates the area containing the larger apatites within this sample...71

Figure 26: BSE image of apatites of interest in NWA 8159. Yellow dashes outline the grain boundary of the apatite to surrounding minerals and matrix material. Each apatite was selected as a “region of interest” (ROI). (A)-(H) Highlight the anhedral and altered appearance of apatites within NWA 8159.72

Figure 27: Plotted volatile abundances on a relative volatile abundance (RVA) diagram form apatites in NWA 8159. The values used in this plot were calculated using stoichiometry methods previously discussed in section 2.3.3 and displayed in table 8. The spreadsheet for this triplot can be viewed on the supplementary disk.74

Figure 28: BSE image of NWA 7034 (Indium mounted sample) taken by the SEM @ ISAAC Facility, University of Glasgow. The red boxes indicated the regions containing the targeted apatites for hydrogen isotope analysis at the University of Hawaii.78

Figure 29: BSE image of NWA 7034 (epoxy mounted sample) taken by the SEM @ ISAAC Facility, University of Glasgow. The red boxes indicated the regions containing the targeted apatites for hydrogen isotope analysis at the University of Hawaii.	79
Figure 30: A Secondary Electron image (A) and a BSE image (B) of pit produced in apatite ROI_1 NWA 7034 (In). The edge of the pit may have incorporated matrix material into the analysis.	81
Figure 31: A Secondary Electron image (A) and a BSE image (B) of the pit produced in apatite ROI_2 NWA 7034 (In).	82
Figure 32: A Secondary Electron image (A) and a BSE image (B) of the pit produced in apatite ROI_4 NWA 7034 (In).	83
Figure 33: A Secondary Electron image (A) and a BSE image (B) of the pit produced in apatite ROI_8 NWA 7034 (In).	84
Figure 34: A Secondary Electron image (A) and a BSE image (B) of the pit produced in apatite ROI_3 NWA 7034 (Epoxy). A hole can be observed in the bottom of the pit (indicated by the red arrow), indicating that matrix material may have been incorporated at the end of the analysis as the beam penetrated further into the apatite.	85
Figure 35: A Secondary Electron image (A) and a BSE image (B) of the pits produced in apatite ROI_5 NWA 7034 (Epoxy). Two pits can be seen in this figure as during analysis it was discovered that the matrix (pit 5a) had been targeted instead of the apatite and therefore a second pit was made (pit 5b).	86
Figure 36: A Secondary Electron image (A) and a BSE image (B) of the pit produced in apatite ROI_7 NWA 7034 (Epoxy).	87
Figure 37: A Secondary Electron image (A) and a BSE image (B) of a pit produced in apatite ROI_8a NWA 7034 (Epoxy).	88
Figure 38: BSE image of the pyroxene pit from NWA 7034 (In).	89
Figure 39: A Secondary Electron image (A and B) and a BSE image (C) of the pyroxene pit from NWA 7034 (Epoxy). The loose fragment on the right of the pit is a result of re-polishing after hydrogen isotope analysis. On the right hand side of the pit it appears that the beam may have penetrated the matrix (indicated by red dashed line).	90
Figure 40: Plotted volatile abundances on a relative volatile abundance (RVA) diagram form apatites in NWA 7034. Blue diamonds represent apatites which OH components were measured by SIMS analysis. Red diamonds (previously shown in figure 21) represent	

apatites where the OH component was calculated using stoichiometry methods previously discussed in section 2.3.3.92

Figure 41: Groupings of apatite based on δD versus water content (H₂O wt.%). Group 1 (ROI_4,8 and 8a) is contained within the green region, Group 2 (ROI_1, 2 and 7) in the blue region and Group 3 (ROI_3 and 5) in the orange region. These colours relate to the information from table 12. 2σ uncertainties are shown as error bars in the graph above, these errors can be viewed in table 11 and in the supplementary disk provided.95

Figure 42: (A) The water content (H₂O wt. %) versus δD for apatites from Hallis et al. (2016) (see paper for the range of martian meteorites measured) and (B) apatite data from this study of NWA 7034. The orange region represents martian mantle and terrestrial values (i.e., <275‰). Group 3 apatites all plot within this orange region, indicating that they record either martian mantle or terrestrial signatures. Group 1 apatites all plot above the orange region, indicating shock implantation of hydrogen. Most of Group 2 apatites plot above the orange region, however ROI_2 partially falls into it. This may suggest some terrestrial contamination in this apatite.101

List of Tables

Table 1: A summary of the main clast types (igneous, sedimentary, impact origin) present in NWA 7034 as described by Santos et al. (2015).	27
Table 2: Geo MK II Block standards used during SEM-EDS analysis to achieve quantitative results at the ISAAC Facility, University of Glasgow. The table lists which standard was used for each element.	44
Table 3: Astimex standards used during SEM-EDS analysis at the Natural History Museum, London. The table lists which standard was used for each element.	46
Table 4: Measurement times for selected elements for analysis. Since Deuterium (^2H or D) is less abundant than Hydrogen (^1H) it is measured over a longer period of time (e.g., 40 seconds) compared to hydrogen, which is measured for a shorter time (3 seconds). Since ^{18}O is abundant it was measured over a short time (2 seconds) similar to ^1H	51
Table 5: Stoichiometry calculations from SEM-EDS data from apatites within NWA 7034(In). (A) Displays the oxide wt. % of each element analysed, along with the oxygen equivalent (-O=F and -O=Cl, previously discussed in section 2.3.3). Values of Cl and F wt. % abundances from each analysis are highlighted in blue. (B) Displays the structural formula based on 13 anions for each analysed element. The Cl, F and OH values, calculated from stoichiometry, are highlight in yellow. These values are plotted in figure 23.....	67
Table 6: Stoichiometry calculations from SEM-EDS data from apatites within NWA 7034(Epoxy). (A) Displays the oxide wt. % of each element analysed, along with the oxygen equivalent (-O=F and -O=Cl, previously discussed in section 2.3.3). Values of Cl and F wt. % abundances from each analysis are highlighted in blue. (B) Displays the structural formula based on 13 anions for each analysed element. The Cl, F and OH values, calculated from stoichiometry, are highlight in yellow. These values are plotted in figure 23.....	68
Table 7: Stoichiometry calculations from SEM-EDS data from apatites within NWA 7034(Epoxy). (A) Displays the oxide wt. % of each element analysed, along with the oxygen equivalent (-O=F and -O=Cl, previously discussed in section 2.3.3). Values of Cl and F wt. % abundances from each analysis are highlighted in blue. (B) Displays the structural formula based on 13 anions for each analysed element. The Cl, F and OH values, calculated from stoichiometry, are highlight in yellow. These values are plotted in figure 23.....	69
Table 8: Stoichiometry calculations from SEM-EDS data from apatites within NWA 8159. (A) Displays the oxide wt. % of each element analysed, along with the oxygen equivalent (-O=F and -O=Cl, previously discussed in section 2.3.3). Values of Cl and F wt. %	

abundances from each analysis are highlighted in blue. (B) Displays the structural formula based on 13 anions for each analysed element. The Cl, F and OH values, calculated from stoichiometry, are highlight in yellow. These values are plotted in figure 27.....75

Table 9: Elemental abundances of NWA 8159 matrix material in ROI_5 from SEM-EDS analysis. Spectrum (Spec) 2 and 3 where two separate spot analyses on the matrix. No F was measured in the these analyses indicating a F-poor matrix.76

Table 10: The wt. % abundances of Cl, F and H₂O for each analysed apatite in NWA 7034. The wt. % values for Cl and F were measured using SEM-EDS analysis. The H₂O wt. % values was directly measured using the SIMS at UH. These values are plotted as blue diamonds in figure 40 above.92

Table 11: Hydrogen isotope data from all analysed standards, apatites and anhydrous minerals. δD is represented in ‰. H₂O is represented in both wt. % and ppm(‰). The 2σ uncertainties for δD and H₂O values are also displayed. All numbers have been rounded to 2 decimal places, with the exception of the H₂O wt. % column which has been rounded to 3 decimal places. The calculations involved in this table can be viewed in the supplementary disk provided.93

Table 12: Groupings of apatite within NWA 7034 based on δD , water content (H₂O) and texture. Group 1 is highlighted in green, Group 2 is highlighted in blue and Group 3 is highlighted in orange. For uncertainty values refer to table 11.95

List of Equations

- Equation 1: The calculation for the Vienna Standard Mean Ocean Water (VSMOW), given in parts per million (‰) (Hallis et al., 2017).35
- Equation 2: Oxygen equivalent calculations for Cl and F based on work by Deer et al. (1992) and McCubbin et al. (2013) where: $-O=F$ and $-O=Cl$ is the oxygen equivalent for F and Cl, respectively; and 16 is the atomic mass of O. Since O has a charge of -2 and Cl and F have a charge of -1, the calculation involves two times the atomic mass of F and Cl, and only 1 times the atomic mass of O (which is 16).47
- Equation 3: The molecular proportion of oxides calculation (Deer et al., 1992; McCubbin et al., 2013). This calculation should be applied to all elements analysed.47
- Equation 4: Calculation for the atomic proportion of O from each molecule (Deer et al., 1992; McCubbin et al., 2013).47
- Equation 5: The calculation for the structural formula based on 13 anions(Deer et al., 1992; McCubbin et al., 2013).....47
- Equation 6: The calculation for the true total (Deer et al., 1992; McCubbin et al., 2013). .47
- Equation 7: Normalisation factor for 13 anions calculation (Deer et al., 1992; McCubbin et al., 2013) This is required as the apatite chemical formula contains 13 oxygens.....48
- Equation 8: The calculation of the structural formula based on 13 anions (Deer et al., 1992; McCubbin et al., 2013). By adding the results from this calculation a total number of anions in the X-site of the apatite can be determined (it should equal 1). A value <1 indicates a missing component (i.e., OH).48
- Equation 9: The water content of the unknown apatites where $1H-/18O-$ ratio and the slope of the $1H/18O$ vs. H_2O wt. % standard calibration line estimated the unknown water content (Hallis et al., 2012).53
- Equation 10: Reproducibility of apatite water content and δD values, where estimated is the estimated H_2O or δD value of each apatite standard and true is the H_2O or δD value of each apatite standard (Hallis et al., 2012).53
- Equation 11: The 2σ error for H_2O and δD of each apatite (Hallis et al., 2012).....53

Chapter 1 Introduction

1.1 Introduction to the Project

Until recently, Alan Hills (ALH) 84001 (martian orthopyroxenite) was the only martian meteorite that did not fit within one of the three groups- shergottite, nakhlite or chassignite (SNC). However, the discovery of Northwest Africa (NWA) 7034 (along with paired stones: NWA 7533, NWA 7475, NWA 7906, NWA 7907, NWA 8114, NWA 8171)(Santos et al., 2015), as well as NWA 8159 has expanded the diversity of the martian meteorite inventory on Earth beyond the SNC groups (Wright et al., 2011; Agee et al., 2013; Cartwright et al., 2014; Simon et al., 2014; Shearer et al., 2015).

NWA 7034 was found in Morocco in 2011. It is a fresh find that was nicknamed 'Black Beauty' on account of its fresh black, glassy, fusion crust (a sign of minimal terrestrial weathering). NWA 7034 is a polymict basaltic breccia- reportedly formed via impact melting and welding of an area of martian regolithic soil (Agee et al., 2013; Muttik et al., 2014; Goderis et al., 2016). This unique meteorite is water-rich compared to the other known martian meteorites, with ~600 ppm of extraterrestrial H₂O released during stepped heating (Agee et al., 2013). The high water content may be partly due to the presence of hydrous apatite, as NWA 7034 contains numerous apatite grains within various lithological clasts, as well as free apatite grains within the groundmass (Muttik et al., 2014). As NWA 7034 is a polymict breccia it has yielded a range of dates between ~1.5 Ga to 4.4 Ga, representative of various crystallisation and resetting events (Agee et al., 2013; Lin et al., 2016; McCubbin et al., 2016). U-Pb dating of apatite, zircon and phosphates record ages of ~1.5 Ga which indicate a resetting event (McCubbin et al., 2016). Rb-Sr whole rock data gives an age of 2.089 ± 0.081 Ga (Agee et al., 2013), but in-situ zircon grain U-Pb ages of 4.42-4.46 Ga have been recorded (Lin et al., 2016).

NWA 8159 was discovered in Morocco, 2013. It contains evidence of terrestrial weathering- calcite veins (Agee et al., 2014a; Agee et al., 2014b). This meteorite is classed as an augite basalt, with small (<20 μ m) apatite grains in the mesostasis. It is reported to have formed as either an eruptive flow or shallow intrusion on Mars (Agee, 2014). NWA 8159 has a Sm-Nd crystallisation age of 2.37 ± 0.25 Ga (Herd et al., 2017), which represents the early Amazonian period of Mars' history. This period is not represented by any other martian meteorite. As NWA 8159 is newly discovered there are currently no peer

reviewed publications focused on the petrology and mineralogy of this meteorite. However, there are several non peer-reviewed conference abstracts that do provide some data.

Apatite ($\text{Ca}_5(\text{PO}_4)_3(\text{F}, \text{Cl}, \text{OH})$) is the main volatile bearing phase in most martian meteorites (Greenwood et al., 2003; McCubbin et al., 2015b; Howarth et al., 2015), being a major sink for fluorine (F), chlorine (Cl) and water (OH). Therefore, the ratio of these three elements in meteorite apatite can indicate their abundance in martian parental melts. In planetary science apatite is commonly used as a tool for the quantification of H₂O within planetary bodies (e.g., the Moon and Mars) (Santos et al., 2013; McCubbin and Jones, 2015).

The aim of this project was to determine the apatite volatile content for both NWA 7034 and NWA 8159. For the latter, apatite volatile content should relate to the volatile content of the parental melt, hence providing information about a previously unstudied martian volcanic province. For NWA 7034, apatite volatile data could provide information about various clast parental melts, or the event that welded this breccia together. NWA 7034 apatite grains are large enough for the collection of in-situ hydrogen isotope (D/H) data, which will indicate the source of water in each grain (e.g., parental melt water sourced from the martian interior, crustal water sourced from the cryosphere, or atmospheric water). Unfortunately, apatites in NWA 8159 are too small (<25 μm) for this type of analysis

1.2 Introduction to Martian Meteorites

Currently there are ~ 85 known martian meteorites (National Geographic, 2017; Martian Meteorite Compendium, 2017), which appear to show mineralogical and textural similarities with terrestrial ultramafic and basaltic rocks (McSween, 1984; Hutchinson, 2004), providing a record of martian volcanism (Papike et al., 2009). The shergottites, nakhlites and chassignites (SNC's) make up the three main groups, with the addition of the three ungrouped meteorites ALH 84001 (orthopyroxenite), NWA 7034 (breccia), and NWA 8159 (basalt). The SNC's fall into two age groups (figure 1). The shergottites crystallised at ~165- 475 Ma, whereas the nakhlites and chassignites crystallised at ~1300 Ma (Papike et al., 2009). The orthopyroxenite, ALH 84001 is the oldest martian meteorite

having crystallised at ~ 4.5 Ga (Papike et al., 2009). The polymict breccia, NWA 7034 has yielded a range of dates between ~ 1.5 Ga to 4.4 Ga, representative of various crystallisation and resetting events (Agee et al., 2013; Lin et al., 2016; McCubbin et al., 2016). NWA 8159 crystallised at ~ 2.3 Ga (Kayzar, 2015; Herd et al., 2017), representing the early Amazonian period of Mars, which no previous martian meteorite has recorded (figure 1). Each one of these distinctive age groupings likely represents a distinct volcanic episode on Mars. However, NWA 7034 is a breccia, therefore can represent much more than one area/age/volcanic episode on Mars. Mars is likely to have experienced more than four individual volcanic episodes and therefore figure 1 reflects the bias of our sample suite of martian meteorites and that they may not be representative samples of the surficial igneous rocks on Mars.

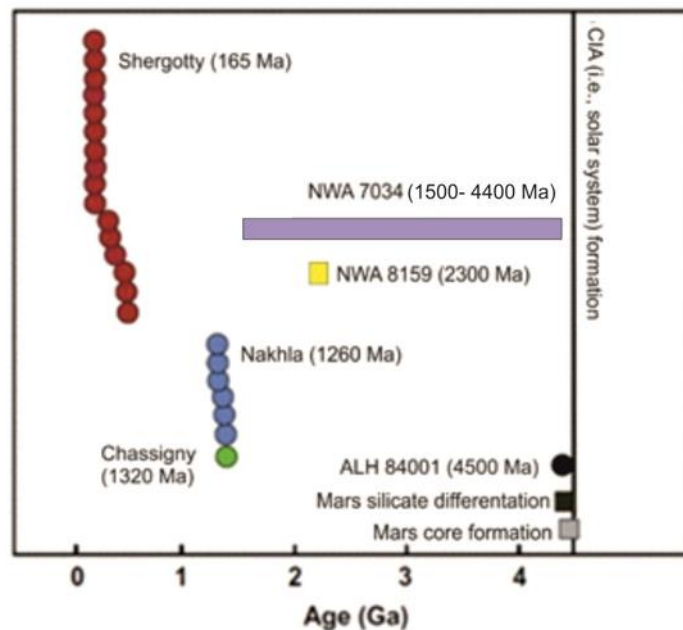


Figure 1: Ages of selected SNC martian meteorites and ungrouped martian meteorites. Shergottites in red, nakhlites in blue, Chassigny in green, ALH 84001 in black, NWA 7034 in purple and NWA 8159 in yellow (adapted from Papike et al., 2009).

1.2.1 Martian Origin

Initially, the notion that the SNC meteorites were of martian origin was founded on their young crystallisation ages, which range from ~ 1.3 Ga to 180 Ma (McSween, 1994; Papike et al., 2009). Young crystallisation ages imply geologically recent igneous activity has occurred which therefore, rule out a lunar origin as the Moon was “dead” by ~ 2.5 Ga

(Bogard and Johnson, 1983; Hutchinson, 2004). Young crystallisation ages also rule out an asteroidal origin, as igneous activity on an asteroid body late in solar system history is highly unlikely. Asteroids are also too small to have undergone the required fractionation needed to produce the petrological and geochemical properties that are observed within these meteorites (McSween, 1984; McSween 1994; Treiman et al., 2000). Alteration minerals and carbonate phases in the nakhlites and in ALH 84001 also rule out a lunar origin (Papike et al., 2009). Despite evidence for aqueous alteration among asteroids, SNC meteorites indicate geologically recent alteration, which matches with Mars as a parent body due to the presence of an atmosphere, polar caps and surface evidence of relatively recent fluvial activity (Treiman et al., 2000).

Further definitive evidence of a martian origin comes from the analysis of the martian atmosphere conducted by NASA's *Viking* landers (*Viking 1* and *Viking 2*) in 1976. This atmospheric composition was compared, to trapped pockets of gas, contained in shocked glass within the suspected martian meteorites. Research conducted by Bogard and Johnson (1983) on the Shergottite Elephant Moraine (EET) 79001 deduced that isotopic measurements of Argon (Ar) trapped within the shocked glass of this meteorite matched the atmospheric data for noble gases from the *Viking* landers. The composition of the martian atmosphere is unique in the solar system and therefore the evidence (chemical and isotopic signatures) of its presence within the SNC meteorites strongly links them to Mars (McSween, 1994; Treiman et al., 2000; Hutchinson, 2004; Day et al., 2006; Aoudjehane et al., 2012).

Additional evidence for a martian origin for these meteorites is their $\Delta^{17}\text{O}$ isotopic ratio (Clayton and Mayeda, 1996; Lodders and Fegley, 1997; Franchi et al., 1999). All bodies within the solar system have a distinctive $\Delta^{17}\text{O}$ isotopic ratio as indicated by figure 2. Oxides and anhydrous silicates within the SNC meteorites all contain similar $\Delta^{17}\text{O}$ isotopic ratios and are therefore inferred to have been formed by the same parent body (i.e. known to be Mars from *Viking* and more recent missions) (Clayton and Mayeda, 1996; Treiman et al., 2000).

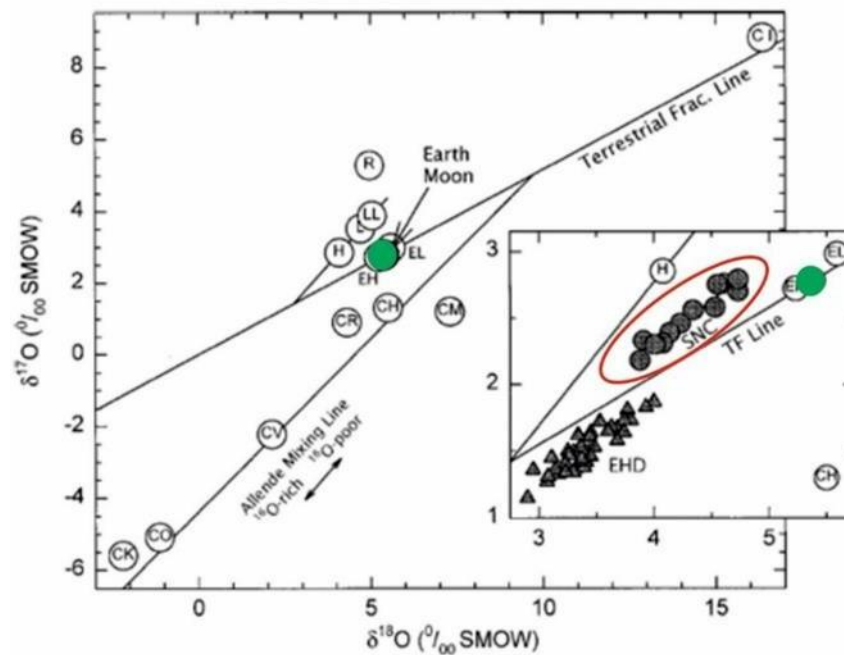


Figure 2: Oxygen isotope values for the Earth-Moon system (indicated by the green circle), chondrites and the SNC meteorites (highlighted by red outline). The insert enlarges the region associated with the differentiated meteorites such as the HEDs (howardites, eucrites and diogenites) and the SNC meteorites (adapted from Lodders and Fegley, 1997).

1.2.2 Shergottite, Nakhlite, Chassignite Martian Meteorites

Shergotty, Nakhla and Chassigny were the first martian meteorites discovered. All of which were observed falls occurring in 1865, 1911 and 1815, respectively (Hutchinson, 2004; Papike et al., 2009). These findings led to the categorisation (SNC grouping) of martian meteorites; shergottites (basalts and Iherzolites), nakhrites (clinopyroxenes), chassignites (dunites). Until recently – before the hugely successful martian orbiter and rover missions of the past ~15 years- the SNC's and ALH 84001 (orthopyroxenite, discovered in 1984) formed the bases of our understanding of the geology of Mars (McSween, 1994; Treiman et al., 2000; Hutchinson, 2004; Day et al., 2006; Papike et al., 2009; McCubbin et al., 2012). The SNC meteorites are essentially a group of unbrecciated ultramafic and mafic achondrites, which display igneous textures (Treiman et al., 2000). The SNC meteorites differ from other differentiated achondrites in terms of their petrological, chemical and isotopic similarities (McSween, 1994; Treiman et al., 2000; Hutchinson, 2004; Day et al., 2006).

1.2.2.1 Shergottites

The shergottites are the youngest and most common type of martian meteorite; accounting for ~70% of all finds (Borg and Drake, 2005; Day et al., 2006). These meteorites are pyroxene, plagioclase (\pm) olivine basalts and basaltic cumulates which can be separated into three subgroups: pyroxene-phyric basalts, olivine-phyric basalts and Iherzolites (Papike et al., 2009). Shergottites are reportedly the result of partial melting in the martian mantle, and, therefore, contain a record of the mantle chemistry of Mars (Smith et al., 1984; Borg and Draper, 2003; McCubbin et al., 2012). Geochemical differences, including rare Earth element (REEs) contents, within the group result in a range from depleted to enriched (Borg et al., 1997; Herd et al., 2002; Borg and Draper, 2003; Herd, 2003; Symes et al., 2008; McCubbin et al., 2012). Depleted shergottites, characterised by low light REEs contents, represent the martian mantle with no partial melting or alteration occurring since the differentiation of Mars (Borg et al., 1997; McCubbin et al., 2012). Enriched shergottites, characterised by flat REE patterns, are the result of assimilation or mixing with either a geochemically enriched crustal or mantle source (i.e., Borg and Draper, 2003; Borg et al., 1997; Herd et al., 2002; Sarbadhikari et al., 2009, 2011; McCubbin et al., 2012). There is evidence of impact shock in all shergottites, resulting in maskelynized plagioclase, indicating that they experienced ~300 kbar of shock (Wood and Ashwal, 1981; Bogard and Johnson, 1983; Hutchinson, 2004). Cosmic ray exposure ages of the shergottites ($\sim 0.7 \pm 0.3$ Ma) indicate that they were all ejected during the same impact event (Aoudjehane et al., 2012), suggesting a common site on Mars.

1.2.2.2 Nakhrites

The nakhlite group all show textural and chemical similarities. Nakhrites are calcium-rich clinopyroxene cumulates composed predominantly of augite with minor olivine in a fine-grained mesostasis (Lentz et al., 1999; Papike et al., 2009). Augites present within the nakhlites preserve an orientation, which is interpreted to have formed during an extrusive lava flow or shallow intrusion (Lentz et al., 1999; Hutchinson 2004). Aqueous alteration within the nakhlites is interpreted to have occurred on the martian surface, based on isotopic and textural evidence (Lentz et al., 1999; Hutchinson 2004). For example, magmatic inclusions within olivines contain products of alteration indicating the presence of water (Wood and Ashwal, 1981; Hutchinson, 2004), and alteration veins are

vesiculated and cross cut by the fusion crust (Gooding et al., 1991; Hallis, 2013). The nakhlites differ from other martian meteorites in that there is little to no evidence of shock within them. Unlike the shergottites, the plagioclase in the nakhlites has not been converted into maskelynite and there is no shock-produced glass present (Hutchinson, 2004; Papike et al., 2009)

1.2.2.3 Chassignites

The chassignites are olivine-rich dunites, which are petrologically similar to the nakhlites. Feldspar compositions in particular, are nearly identical to nakhlites (Wood and Ashwal, 1981; Treiman et al., 2000; Papike et al., 2009). Olivine crystals within these meteorites are typically euhedral-anhedral, characteristically meeting at 120° triple junctions. Chassignites display poikilitic textures where calcium rich pyroxene encloses olivine (McSween, 1994; Hutchinson, 2004). Crystal settling in a magma chamber is inferred to be the formation mechanism of the chassignites due to the olivine rich cumulate texture of these meteorites (Wood and Ashwal, 1981; Hutchinson, 2004). The chassignites show evidence of experiencing moderate shock through the deformation of minerals such as fractured olivine, recrystallisation of pyroxene and olivine undulatory extinction (Wood and Ashwal, 1981; Hutchinson, 2004). The common age (~1.3 Ga) represented by the chassignites and nakhlites, as well as a similar cosmic ray exposure age for Chassigny and Nahkla ($8.5 \pm 0.5 \times 10^6$ years, $8 \pm 0.8 \times 10^6$ years, respectively) (Lancet and Lancet, 1971; Podosek, 1973; Wood and Ashwal, 1981) suggests that chassignites come from the nakhlite impact site.

1.2.3 Martian Orthopyroxenite ALH 84001

Alan Hills (ALH) 84001 is a unique meteorite among the martian meteorite suite as it is the only orthopyroxenite from Mars (Papike et al., 2009). Currently, it is the oldest known martian meteorite, with a crystallisation age of ~4.5 Ga (figure 1), and represents igneous activity early in Mars' history. ALH 84001 is predominantly composed of highly shocked orthopyroxenes displaying a triple junction texture with interstitial maskelynite (Romanek et al., 1994; Hutchinson, 2004; Papike et al., 2009). ALH 84001 is a highly shocked meteorite with possibly five separate deformation events occurring in its history, which are characterised by crush zones, fractures, shearing, replacement of plagioclase, melt veins, and impact related shock (Treiman, 1998; Hutchinson, 2004). Carbonate clasts

are also present as globules, suggesting this meteorite was exposed to a shallow water environment after crystallisation (Hutchinson, 2004).

1.2.4 Northwest Africa (NWA) 7034

NWA 7034 (nicknamed Black Beauty) is a single stone, ~320g martian meteorite discovered in Morocco in 2011 (Agee et al, 2013). This meteorite was not an observed fall and therefore terrestrial contamination may have occurred, the full extent of this is unknown. However, the presence of a fresh black, glassy fusion crust indicates minimal terrestrial contamination has occurred. Noble gas measurements and Fe/Mn ratios of pyroxenes confirm that NWA 7034 is of martian origin (Santos et al., 2015; see Agee et al., 2013 and Cartwright et al., 2014). Oxygen isotopes are a critical tool used to characterise different meteorite groups. Martian meteorites display their own unique oxygen $\Delta^{17}\text{O} = 0.15\text{--}0.35\text{‰}$ as previously described in section 1.2.1. However, analysis of oxygen isotope systematics of NWA 7034 reveal that it has an anomalously higher $\Delta^{17}\text{O}$ than the other martian meteorites, $\Delta^{17}\text{O} = 0.58 \pm 0.05\text{‰}$ (Agee et al., 2013). Bulk composition analysis of NWA 7034 has linked this meteorite with composition of the martian crust as well as the rocks and soils measured from the Gusev Crater (via *Curiosity*) (McSween et al., 2009; Taylor and McLennan, 2009; Agee et al, 2013; Tartèse et al., 2014; Santos et al., 2015). This unique meteorite is also water-rich compared to the other known martian meteorites, with ~600 ppm of extraterrestrial H_2O released during stepped heating (Agee et al., 2013). The high water content may be partly due to the presence of hydrous apatite, as NWA 7034 contains numerous apatite grains within various lithological clasts, as well as free apatite grains within the groundmass (Muttik et al., 2014).

The texture of NWA 7034 makes it unique, as it is texturally dissimilar to any of the SNC meteorites. Basaltic breccias originating from the Moon and HED meteorites are common but not represented in our martian sample suite until now (Wright et al., 2011; Agee et al., 2013). The clastic nature of NWA 7034 means it contains a range of crystallisation ages up to 4 Ga, with a Rb-Sr whole rock age of 2.089 ± 0.081 Ga (Agee et al., 2013) and U-Pb zircon grain ages of 4.42-4.46 Ga which record the formation of crustal rock early in Mars history (Lin et al., 2016).

NWA 7034 can be described as a polymict basaltic breccia dominated by phenocryst fragments of low-calcium pyroxene, plagioclase, and pigeonite set in a very fine-grained groundmass (Agee et al., 2013). Agee et al. (2013) stated that the most

abundant phase is plagioclase (~40%) followed by low Ca-pyroxene (~25%), clinopyroxene (~18%), iron oxides (~9%), alkali feldspars (~5%), and apatite (~3%), which is consistent with EDS images (chapter 3). Cl-rich apatite is present within various lithological clasts as well as free apatite grains within the matrix (Muttik et al., 2014). A diverse set of lithologies (igneous, sedimentary and impact origin) are contained within NWA 7034 resulting in numerous clast types such as: igneous clasts, protobreccia clasts and melt clasts (table 1). The igneous clasts present in NWA 7034 vary in compositions, indicating that either: they are not related, originating from separate igneous sources or there was compositional variation within a shared parent source during formation (Santos et al., 2015). Protobreccia clasts are interpreted to have formed prior to the formation of NWA 7034 within a pre-existing regolith (Santos et al., 2015; McCubbin et al., 2016).

Clast type (number of observations)	Distinguishing characteristics
Proto-breccia	Fine grained matrix surrounding coarser grained mineral fragments and other types of clasts; distinct texturally or compositionally from bulk matrix. Matrix may contain different proportions and distributions of silicate phases, phosphates, and Fe-Ti oxides than bulk matrix
Melt clasts	Contains devitrified glassy material or skeletal/plumose crystals, may contain relict grains. Devitrified mesostasis may contain numerous small Fe-Ti oxides, olivine may be present as skeletal/plumose crystals, common plagioclase and pyroxene crystals
Igneous clasts	Interlocking mineral grains lacking matrix material. This clast group is subdivided into four separate groups listed below
Basalt clasts	Basalt bulk composition. Textures include subophitic (with either strongly anhedral grains, subhedral grains, or irregular grains) and granulitic. Dominated by plagioclase and pyroxene with minor apatite and Fe-Ti oxides. Mg#s 53-62, $Fe^{3+}/\sum Fe$ 0.06-0.35
Trachyandesite clasts	Trachyandesite bulk composition. Contain poikilitic texture and subophitic texture with irregular grain boundaries. Contain abundant K-feldspar typically poikilitically enclosing plagioclase. Mg#s 54-57, $Fe^{3+}/\sum Fe$ 0.08-0.29
Basaltic andesite clasts	Basaltic andesite bulk composition. Granulitic texture. Very minor amounts of apatite and Fe-Ti oxides. Mg#s 57, 28, $Fe^{3+}/\sum Fe$ 0.03, 0.1
FTP clasts	Basaltic texture. Relatively large apatite and Fe-Ti oxide grains tending towards euhedral morphologies; frequently lack pyroxene. P_2O_5 rich, Mg#~52 when containing pyroxene, ~10 when lacking pyroxene; $Fe^{3+}/\sum Fe$ ~0.24-0.38

Table 1: A summary of the main clast types (igneous, sedimentary, impact origin) present in NWA 7034 as described by Santos et al. (2015).

The assembly of NWA 7034 is poorly understood as its petrogenesis is hard to synthesise due to the many different components it contains. However, it is evident that the formation of this breccia was not a single stage process (Santos et al., 2015). McCubbin et al. (2016) conducted the most recent study on the formation of NWA 7034, focusing on the clast types, as well as zircon and apatite dating. Their study provided evidence of a breccia wide thermal event at 1.5 ± 0.1 Ga. Evidence for a thermal event was presented by

submicron textural evidence within the bulk matrix where partial equilibration had occurred (Muttik et al., 2014), resulting in crystals (e.g., pyroxene, plagioclase, apatite) meeting at 120° triple junctions. Further evidence for a breccia wide thermal event was discovered using U-Pb dating on apatite. All of the apatite grains within their sample recorded a date of 1.49 ± 0.09 Ga (figure 3) which was inferred to coincide with the heating that would have accompanied lithification of the breccia (Muttik et al., 2014). McCubbin et al. (2016) constrained this heating event to 500-800°C.

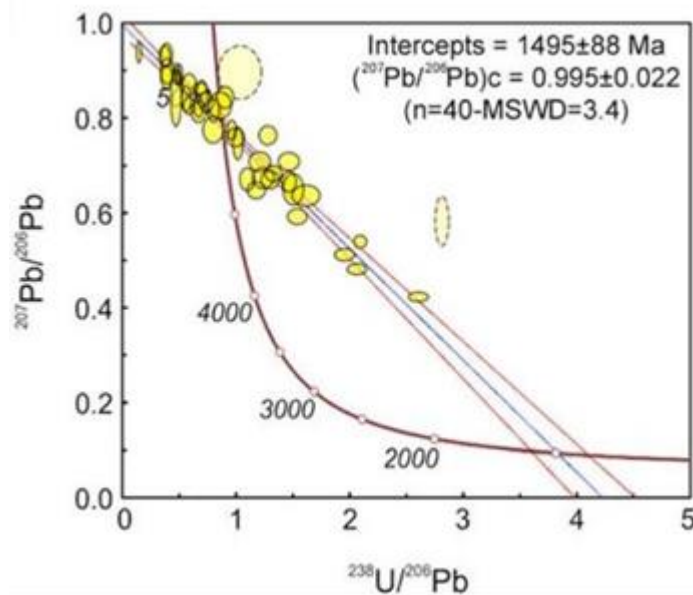


Figure 3: Apatites were analysed by SHRIMP-RG for U-Pb dating on Cl-rich apatite in NWA 7034. The results are plotted on a Tera-Wasserburg Concordia diagram and give a date of 1.49 ± 0.09 Ga. Ellipses are 1 sigma errors on the measurements (dashed ellipses are not date measurements) (McCubbin et al., 2016).

The components of NWA 7034 are inferred to have been deposited during a volcanic (pyroclastic eruption) and/or impact event(s) due to clast size and distribution (Humayun, 2013; Agee et al., 2013; McCubbin et al., 2016). However, impact processes are the favoured mechanism of formation due to the ancient components (4.42-4.46 Ga zircon grains) and the disturbance of Osmium isotope systematics at ~ 1.4 Ga within NWA 7034 (Goderis et al., 2016; McCubbin et al., 2016). It is also important to note that it is possible that this impact event resulted in the formation of a hydrothermal system (Goderis et al., 2016).

Strong evidence of hydrothermal activity was investigated in one of the protobreccia clasts by McCubbin et al. (2016). The evidence they provided showed veining

of magnetite, intergrowths of pyrite and pyroxene and secondary Fe-oxides present in both the matrix and groundmass. The timing of the hydrothermal alteration was interpreted by the magnetite veins, as they are contained within the protobreccia and crosscut existing clasts within the protobreccia. McCubbin et al. (2016) uses this evidence to claim that the hydrothermal alteration occurred before the protobreccia clasts were incorporated into the matrix of NWA 7034 and therefore occurred when the protobreccia was lithified. Characteristics of the hydrothermal fluid could have been overprinted by the thermal event (McCubbin et al., 2016). Other studies of NWA 7034 also indicate that secondary fluids may have altered this meteorite, thus primary information could be obscured (Filiberto et al., 2016).

1.2.5 Northwest Africa (NWA) 8159

NWA 8159 is a unique, newly classified, fine-grained augite basalt, which further expands the diversity of the martian meteorites. This non-SNC type martian meteorite has oxygen isotopes and Fe/Mn ratios which geochemically link it to the SNCs (particularly the nakhlites) yet, its mineralogy and texture uniquely separates it from the SNCs (Simon et al., 2014; Shearer et al., 2015). Terrestrial contamination has affected this meteorite, as it was not a fresh find and veins of terrestrial carbonate are present. NWA 8159's sole pyroxene phase is augite, which has not previously been noted in the other martian meteorites (Agee et al., 2014a; Agee et al., 2014b). Agee et al. (2014) described the dominant mineralogy in NWA 8159 as ~50% augite, ~40% plagioclase (An₅₀₋₆₅), ~5% olivine (Fa₆₁₋₇₆), ~3% magnetite and ~2% orthopyroxene (Fs₅₆₋₈₀) (Sharp et al., 2015). Minor phases present in NWA 8159 include merrillite, ilmenite, Cr-spinel (Agee et al., 2014a), and minor apatite grains (<20 µm). Shock pressures experienced by this meteorite are estimated to be > 15 GPa and <23 GPa, which converted approximately half of the plagioclase to maskelynite (Agee et al., 2014b). NWA 8159 is reported to have formed as either an eruptive flow or shallow intrusion on Mars (Agee et al., 2014b). NWA 8159 has a unique Sm-Nd crystallisation age of 2.37 ± 0.25 Ga (Herd et al., 2017) which represents the early Amazonian period of Mars' history, which no other martian meteorite has previously represented.

NWA 8159 is a newly classified martian meteorite and therefore a broad range of research has not been conducted thus far. The majority of current studies focus on the

alteration present in the cores of olivine grains, which are interpreted to be martian alteration (Shearer et al., 2015; Hallis et al., 2016; Vaci et al., 2016).

1.3 Introduction to Apatite

The mineral apatite ($\text{Ca}_5(\text{PO}_4)_3(\text{F}, \text{Cl}, \text{OH})$) is a common accessory mineral in extraterrestrial rocks (McCubbin and Jones, 2015, and references therein). Meteorites containing apatite are vital to understand the volatile (e.g. Cl, F and OH) distribution throughout the Solar System. The robust structure of apatite has allowed it to be used as a tool to study and quantify the amount of H_2O present in numerous planetary bodies (e.g., the Moon and Mars) as well as examining magmatic volatile contents and alteration/hydrothermal fluids in these planetary bodies (McCubbin and Jones, 2015; Harlov, 2015; Santos et al., 2013).

1.3.1 Structure of Apatite

The apatite mineral group shares a common structure, however the most common of the apatites (the calcium phosphate apatite ($\text{Ca}_5(\text{PO}_4)_3(\text{F}, \text{Cl}, \text{OH})$)) has an additional structural site (the X-crystallographic site), which accommodates the volatile elements F, Cl and OH. The dominant volatile species result in three possible end members: Chlorapatite, fluorapatite and hydroxylapatite (McConnell, 1973). In order to determine the volatile content of parental melts or alteration fluids within apatite, it is necessary to understand how anions behave within the structure of the mineral. The atomic arrangement of apatite (figure 4) consists of three cation sites: tetrahedral (T), M1, and M2. The M2 site is particularly significant as it aides in the accommodation of F, Cl and OH. These three anions are termed the “column anions” as they exist along the edges of the apatite structure (Hughes and Rakovan, 2015). It is also important to note that REEs have the capability to occupy the X-site within apatites along with Cl, F and OH (Hughes and Rakovan, 2015).

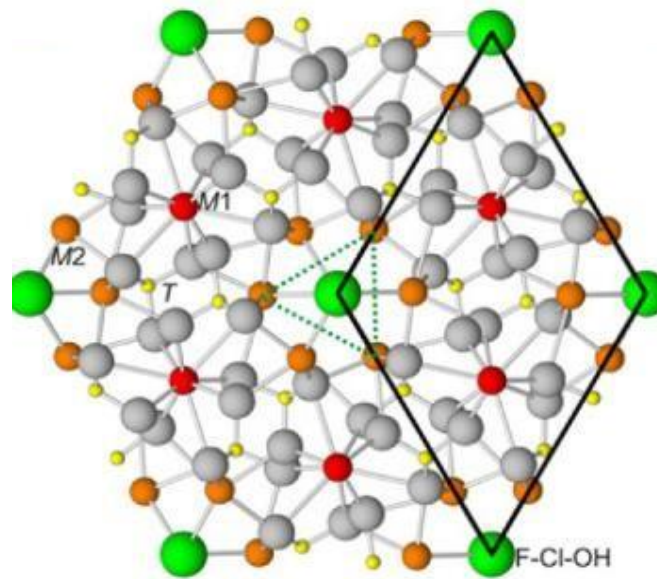


Figure 4: The atomic structure of apatite. T sites are indicated in yellow; M1 in red; M2 in orange. Column anions (F, Cl and OH) are displayed in green (Hughes and Rakovan, 2015).

1.3.2 Volatile Content within Martian Apatite

Martian magmas are $\sim 2.5 \times$ enriched in Cl compared to terrestrial magmas; therefore, Cl is thought to be the dominant volatile in martian magmatics (Filiberto and Treiman, 2009). Orbiter and lander analysis of the martian surface indicate a Cl enrichment at the planet's surface. Furthermore, Cl-rich apatites are common in the majority of the martian meteorites that have been studied (Greenwood, 2005; Patino Douce and Roden, 2006; McCubbin and Nekvasil, 2008; Patino Douce et al., 2011; McCubbin et al., 2013). Terrestrial apatites tend to be F and/or OH-rich and any Cl enrichment is attributed to hydrothermal fluids. As a result of this, Greenwood (2005) has claimed that secondary alteration at the martian surface is responsible for Cl-rich martian meteorites. However, Filiberto and Trieman (2009) attribute the Cl enrichment as a result of a Cl-rich mantle on Mars. Therefore, it is undetermined whether Cl enrichment is a mantle property or from a non-mantle source (McCubbin et al., 2013). However, since Mars has a distinct geochemical signature from other planetary bodies it is likely that Cl enrichment is diagnostic of martian apatite. This assumption is consistent with geochemical models of Mars (McCubbin and Jones, 2015). However it is important to note that more recent studies on martian meteorites (NWA 2975 (shergottite)) conducted by Slaby et al. (2016; 2017), have suggested that primary apatite in martian magmas could also be F-rich.

Apatite is the major volatile bearing phase in martian meteorites (McCubbin et al., 2015c; Howarth et al., 2015; Greenwood et al., 2003). Martian apatites typically contain little OH and on average have a Cl: F: OH ratio of ~5:3:2 (figure 5) (McCubbin and Nekvasil, 2008; Filiberto and Treiman, 2009). However, there are outliers within the martian apatite compositions, which are more enriched in F (figure 5). The high halogen and low water content of the martian basalts indicates that either: parental martian magmas degassed during eruption resulting in a loss of magmatic water but retention in halogens, or the martian mantle is depleted in water (Gross et al., 2013). When these apatites are compared to terrestrial apatites from basaltic rocks (figure 5) it is evident that terrestrial apatites are depleted in Cl and have fluctuating F: OH ratios (Filiberto and Treiman, 2009).

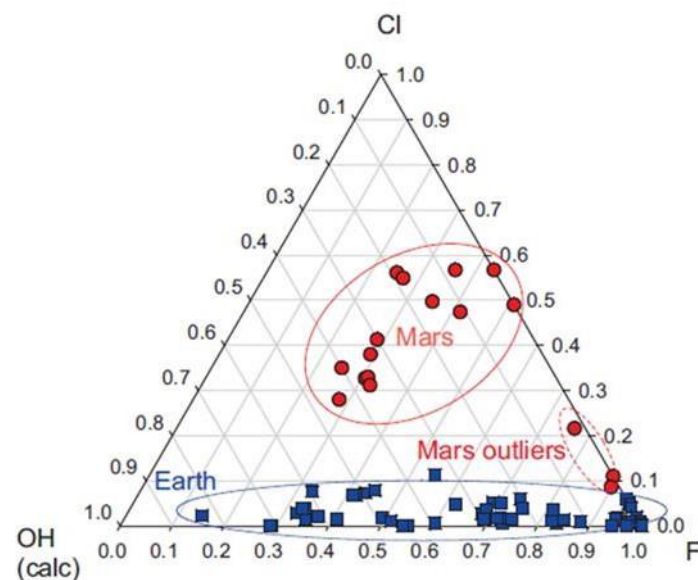


Figure 5: Volatile abundances of Cl, F and OH from martian and terrestrial apatites. Martian apatites tend to be Cl-rich and OH-poor. Outliers represent more fluorine rich apatites (Filiberto and Treiman, 2009).

1.3.3 Volatile Content within Apatite in NWA 7034

Santos et al. (2013) conducted a study on the volatile content of apatites within NWA 7034. They classified apatites based on whether they were found in clasts or in the matrix of NWA 7034 and identified three main clast types, with two containing apatite. The main classifications Santos et al. (2013) devised were gabbroic clast apatite, phosphate clast apatite and matrix grain apatite. Using a JEOL 8200-electron microprobe the volatile content within apatites from each group were analysed, their results are displayed below in

figure 6. Santos et al. (2013), divided their triplot into 4 distinct areas representing different abundances of F, Cl and OH. The green area indicates apatites which have formed from a volatile abundance ratio where $Cl > OH > F$. The blue area comprises of apatites which have formed from a OH rich melt, with a volatile abundance ratio of $OH > Cl > F$. The light purple area indicates apatites have formed from an OH rich melt, but contain more F compared to Cl. Finally, the dark purple area indicates apatites which have formed from a volatile abundance ratio where $F > Cl > OH$. The Santos et al. (2013) data is well spread between the green and blue areas of the triplot, indicating that apatites either formed from two distinct melts (one Cl-rich and one OH-rich) or that apatites formed from the same parental melt that underwent changes resulting in a difference of volatile dominance. McCubbin et al. (2016) also conducted volatile abundance work on apatites within NWA 7034. Their results indicate Cl ranging from 3.42 to 5.31 wt. % and F ranging from 0.51 to 1.42 wt %.

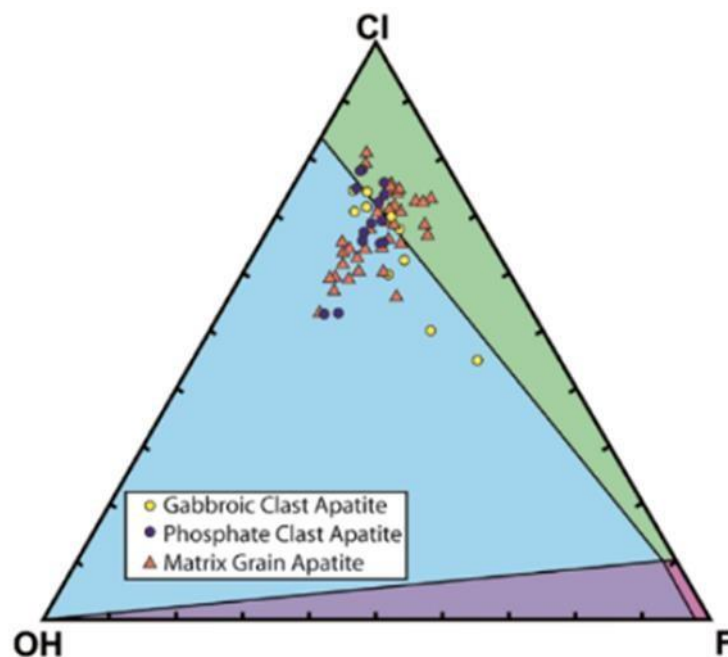


Figure 6: Volatile abundances from apatite from clasts and the matrix of NWA 7034. Different coloured regions indicate different relative abundances of Cl, F and OH in the melt in which the apatites crystallised from. Green: Cl rich melt ($Cl > OH > F$), Blue: OH rich melt ($OH > Cl > F$), Light purple: OH rich melt ($OH > F > Cl$) and dark purple: F rich melt ($F > Cl > OH$) (Santos et al., 2013).

1.3.4 Determining Volatile Abundances of Parental Magma from Apatite

Apatite records F, Cl and OH during martian volcanism. The ratios of these three elements can be used to determine the pre-eruptive abundance of volatile content in magmas and hence their source regions (Filiberto et al., 2016; Gross et al., 2013; Patiño Douce et al., 2011; Filiberto and Treiman, 2009; Patiño Douce and Roden, 2006; Mathez and Webster 2005). Differentiation and eruptive characteristics of martian magmas is strongly influenced by the volatile elements within the melt making their abundances vital in the understanding of martian magmatic systematics (McCubbin and Nekvasil, 2008; Usui et al., 2012).

However, there are difficulties with constraining the volatile abundances in apatites because of secondary processes (i.e. degassing, assimilation, martian surface processes, terrestrial contamination), which can disturb the pre-eruptive volatile content preceding the crystallization of apatite (Gross et al 2013; McCubbin et al, 2011). Since F and Cl are both incompatible elements, their concentrations tend to fluctuate with magmatic fractionation (Aoki et al., 1981; Jambon et al., 1995; Patino Douce and Roden, 2006). However, during more simple igneous processes, the Cl: F ratio should not be adversely effected (Filiberto et al., 2016). However, degassing will affect the Cl: F ratio as F is more compatible with melts whereas Cl will readily degas. Fluorine tends to partition into silicate melts whereas Cl partitions into more hydrous fluids, which can again effect the Cl: F: OH ratio (Patino Douce and Roden, 2006). The systematics of mineral formation can also effect the volatile abundances within minerals. Apatite, that has formed via fractional crystallisation, can overestimate the water content of the source region, therefore effecting the overall Cl: F: OH ratio (Boyce et al., 2014). Martian surface processes (e.g., hydrothermal fluids, alteration) can obscure the original Cl: F: OH due to overprinting thus obscuring parental magma information but instead yielding information relating to alteration fluids at the surface of Mars (Filiberto et al., 2016).

1.4 Introduction to Hydrogen Isotopes (Deuterium/Hydrogen Ratios)

Deuterium/Hydrogen (D/H) ratios are measured and standardised relative to the Vienna Standard Mean Ocean Water (VSMOW). VSMOW is represented by the following equation:

$$\delta D (\text{‰}) = [((D/H)_{\text{Sample}} / (D/H)_{\text{VSMOW}}) - 1] \times 1000$$

Equation 1: The calculation for the Vienna Standard Mean Ocean Water (VSMOW), given in parts per million (‰) (Hallis et al., 2017).

VSMOW has a $\delta D = 0\text{‰}$ (Usui et al., 2012; Hallis et al., 2017). This notation will be used throughout this Chapter when referencing the D/H ratios of martian meteorites. Mars and Earth may have had similar D/H ratios during their formation. However, as a result of the preferential loss of hydrogen in space via Jeans escape (relative to the heavier hydrogen isotope deuterium) in the upper martian atmosphere, the current martian atmosphere is deuterium enriched (Watson et al., 1994; Villanueva et al., 2015). Current martian ratios range from a low δD (0-2000‰) in Polar Regions to high δD (7000‰) in Equatorial Regions (Villanueva et al., 2015). Hydrogen isotope ratios can trace surface water evolution and atmospheric interactions as well as track the source of water (e.g., martian mantle, crustal sedimentary contamination, atmospheric, or groundwater/ice) within meteorites (Hallis et al., 2012; Usui et al., 2015). Due to the capacity for apatite to contain water and for its abundance within martian meteorites, it is commonly used for hydrogen isotope studies.

1.4.1 Martian Water Reservoirs

The presence of water within our Solar System, is a primary focus in planetary science due to the astrobiological significance of this compound. Mars is a prime candidate to find water as recent Mars orbiter and lander missions have revealed evidence for the presence of liquid water early in Mars's history (e.g., Nochian ~3.9 to 4.5 Ga). Geomorphological features (e.g., fluvial valleys), water rich sediments and minerals (e.g. clays) and evaporates (e.g. gypsum) all indicate hydrological activity has occurred on Mars (McCubbin et al., 2012; Kurokawa et al., 2014; Usui et al., 2015). The physical state of water currently present on Mars has been studied by orbiters (e.g. European Mars Express

mission) which have discovered deposits of subsurface ice. Understanding the physical state of surficial water on Mars throughout its history will aid in the interpretation of how this planet's climate evolved as well as if life had the potential to flourish in these climates (McCubbin et al., 2012).

Mars has at least two separate hydrogen isotope reservoirs (figure 7), possibly three (Usui et al., 2015). The first is contained within the martian mantle and displays a δD value $<275\text{‰}$, which is similar to Earth surface values and chondrites (primitive meteorites) with δD values between -230 to 340‰ (Alexander et al., 2012; Usui et al., 2015). The second is near surface water/ice which exhibits δD values between 3000 - 5880‰ (Greenwood et al., 2008; Usui et al., 2012). Although near surface water/ice deposits have not directly been measured until recently, the values are thought to be comparable with atmospheric values because over a geologically short period, the atmosphere and surface water can interact, therefore reservoirs can be mixed. (Leshin et al., 1996; Jakosky and Jones, 1997; Usui et al., 2015). This hypothesis is supported by recent hydrogen isotope measurements of the atmosphere ($\delta D = 4950 \pm 1080\text{‰}$) and near surface ($\delta D = 5880 \pm 60\text{‰}$) which were conducted by the *Curiosity* rover (Webster et al., 2013). Unlike the Earth, Mars has no plate tectonics and therefore recycling of atmospherically equilibrated material into the mantle does not occur. This means that both the atmospheric reservoir and the mantle reservoir have remained completely separated over geological time.

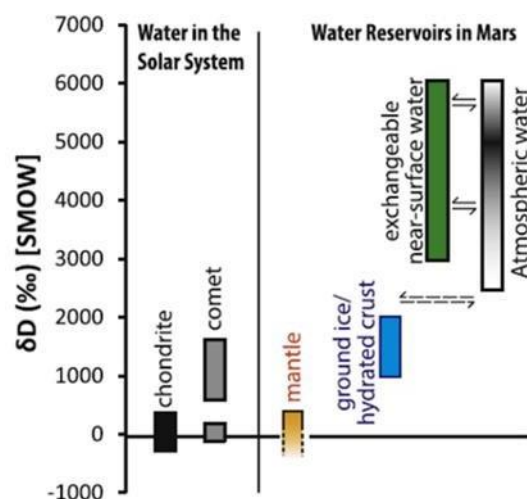


Figure 7: The hydrogen isotope (δD) values of solar system bodies and water reservoirs on Mars. It can be noted that the δD composition of chondrite bodies and the martian mantle is similar. Three distinct martian water reservoirs are displayed in this diagram: martian mantle, near surface water/ice and ground ice/hydrated crust (i.e., the intermediate reservoir) (Usui et al., 2015).

However, Usui et al. (2015) proposed that a third, intermediate reservoir, ($\delta D=1000-2000\text{‰}$) exists based on the study of certain meteorites. It was originally unclear whether these studies had directly sampled an intermediate reservoir or whether terrestrial contamination occurred. However, new data from shergottites (Usui et al., 2015) indicates that an intermediate D/H reservoir is required.

Usui et al. (2015) proposed two possible models for the existence of an intermediate δD reservoir: the Hydrated Crust Model and the Ground Ice Model (figure 8). The Hydrated Crust Model is proposed based on the observations from Mars orbiters and rovers of hydrous sediments and minerals on the martian surface. This combined with hydrous minerals discovered in martian meteorites implies that weathering and hydrothermal activity/alteration has occurred. An intermediate δD composition for hydrated crust could have possibly resulted in these crustal materials interacting with an intermediate source or from interacting with ancient surface water that have a differing δD composition to the current high D/H ratio of Mars. Sediments, interbedded with ground ice (i.e., The Ground Ice Model) could be another possible source for an intermediate reservoir.

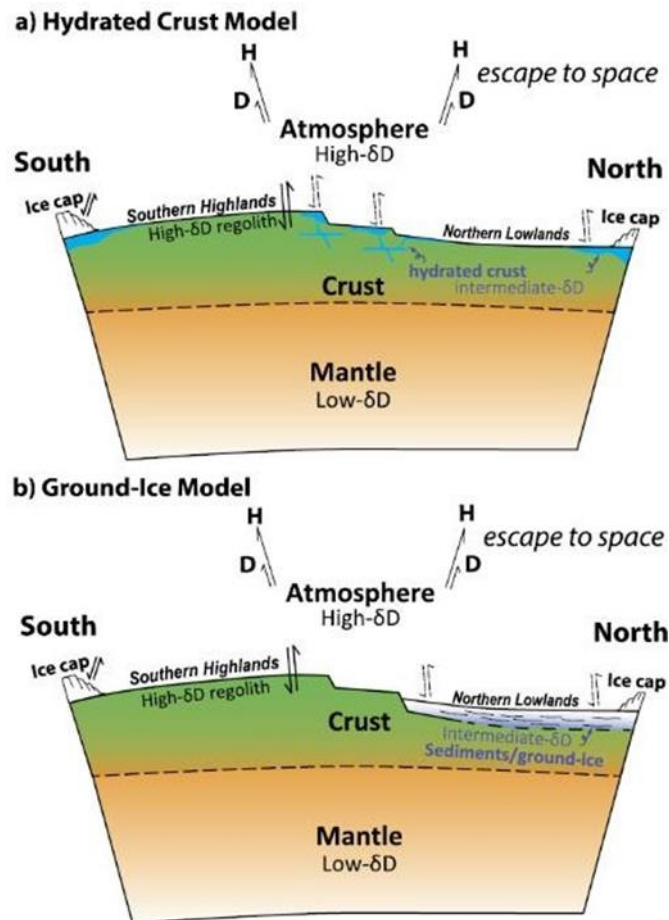


Figure 8: Proposed model from Usui et al., 2015 showing the location of the proposed intermediate water reservoir on Mars through cross sections. (a) Hydrated crust model and (b) Ground ice model. The hydrated crust model suggests that the intermediate reservoir is contained within hydrous sediments and minerals on the martian surface. Whereas, the ground ice model implies that the intermediate reservoir is contained within sediments interbedded with ground ice.

1.5 Project Aims and Objectives

The aim of this project was to determine the apatite volatile content for both NWA 7034 and NWA 8159. The apatite volatile content in NWA 8159 should relate to the volatile abundances of the parental melt, hence providing insight into a previously unstudied martian volcanic province. Since igneous clasts present in NWA 7034 vary in compositions, indicating that either: they are not related and therefore are from separate igneous sources or there was compositional variation within a shared parent source during formation (Santos et al., 2015), the volatile content from apatites in NWA 7034 could possibly yield information on the parental melts from the various clasts. Alternatively,

since NWA 7034 is reported to have been formed as a result of an impact event (Goderis et al., 2016; McCubbin et al., 2016), thermal and hydrothermal alteration may have occurred. A thermal event is confirmed to have occurred in NWA 7034 at ~1.5Ga (McCubbin et al., 2016), therefore, it is possible that original volatile contents within apatite will be overprinted. This should result in all the apatites having closely related Cl: F: OH ratios (which would be uncharacteristic for a polymict breccia). McCubbin et al. (2016) provided previous evidence of hydrothermal alteration, however it was only recorded in protobreccia clasts within NWA 7034 as hydrothermal alteration of apatite was not studied. If it is discovered that hydrothermal alteration of apatite has occurred, then this will also result in the original volatile content within the apatite being overprinted. Previous studies of NWA 7034 report that martian secondary processes may have also effected this meteorite (Filiberto et al., 2016), therefore primary information on the parental source of various clasts may also be obscured.

NWA 7034 apatite grains are large enough for the collection of in-situ hydrogen isotope (D/H) data, which will indicate the source of water in each grain (e.g., parental melt water sourced from the martian interior, crustal water sourced from the cryosphere or atmospheric water). However, due to the thermal event at ~1.5 G, reported by McCubbin et al. (2016) reported, it is important to investigate if all apatites yield the same D/H ratio. If all the apatites do produce similar δD values then it is likely that the thermal event has overprinted their original δD values (as suggested by McCubbin et al. (2016)), meaning it will not be possible to track the source of water within them. Alternatively, if evidence of hydrothermal alteration can be found and similar D/H values are recorded, it may indicate hydrothermal alteration has effected all of the apatites. This would allow for a δD value of surface hydrothermal fluid on Mars at 1.5 Ga to be constrained. Currently there are no hydrogen isotope measurements conducted for this time period. This information combined with measurements of the current D/H ratio of Mars (*Curiosity* data) and other meteorites can collate a picture of the D/H ratio of the martian atmosphere over time. This information in turn will allow for calculations of martian atmospheric stripping. Furthermore, comparing results of the D/H of near surface hydrothermal activity at ~1.5 Ga could also help constrain the D/H ratio of the nakhlite alteration fluid on Mars (estimated to be ~700 Ma (Swindle and Olson, 2004)). Nakhrites contain phyllosilicates, which are notoriously difficult to analyse accurately and are often terrestrial contamination. However, if a nakhlite D/H ratio could be determined accurately in an un-terrestrially

altered sample and if it was found that it was similar to the D/H ratios from NWA 7034 in this study, it may suggest that the nakhlite alteration occurred earlier than 700 Ma and closer to the nakhlite crystallisation age at 1.3 Ga (Swindle and Olson, 2004). However, if the apatites show different δD values then it is possible that the thermal event has not fully effected either all or some of the apatites, which means it will be possible that they will contain their original D/H and thus an apatite mantle source region could be preserved. Any very high D/H values will probably be shock related processes after apatite crystallisation (Hallis et al., 2016). Unfortunately, apatites in NWA 8159 are too small (<25 μm) for this type of analysis.

Chapter 2 Methodology

2.1 Preparation of Samples

Three samples were studied for this research- two samples of NWA 7034 and one sample of NWA 8159. The first NWA 7034 sample had previously been prepared by mounting in an epoxy block, which was then polished using 0.3 μ m aluminium oxide paste mixed with water. Methanol was used to clean the sample after polishing. A second sample of NWA 7034 had been mounted in pure indium and placed in a steel bullet. This sample was polished using dry silicon carbide (SiC) paper down to 6 μ m followed by diamond paste to finish the polishing. Methanol was used to clean the sample after polishing. This sample was selected to be mounted in indium to protect against terrestrial water contamination, in anticipation of future hydrogen isotope (D/H) analysis. One sample of NWA 8159 was prepared. This sample was mounted in an epoxy block, which was subsequently polished using 0.3 μ m aluminium oxide paste mixed with water. Methanol was then used once again to clean the sample after polishing.

2.2 Scanning Electron Microscopy (SEM)

Apatite within the two samples of NWA 7034 and the one sample of NWA 8159 was analysed using the Carl Zeiss Sigma Variable Pressure Analytical Scanning Electron Microscope (SEM) at the Imaging Spectroscopy and Analysis Centre (ISAAC) Facility, University of Glasgow (UoG) (Figure 9). Prior to SEM analyses, the samples were carbon coated (~15nm) to increase conductivity across the sample. Carbon coating is used as it does not have a great effect on the intensity of X-rays and therefore does not interfere with X-ray spectrum measurements. To enhance the conductivity of the samples once they are placed in the sample holder, aluminium tape was attached to link the edge of the sample and the sample holder. The SEM was used to locate, characterise and image apatite in all samples, as well as providing insight into their lithological context. Energy-dispersive X-ray Spectroscopy (EDS) point and map analysis was conducted on all samples, using both Aztec 2.2 software and INCA software to determine the major and minor (including F and Cl) element concentrations of apatite. Elemental distribution maps of all samples were also produced to aide in the location of individual apatite grains.

2.2.1 Scanning Electron Microscopy- Backscatter Imaging

The Scanning Electron Microscopy (SEM) technique requires a focused electron beam to hit the surface of the sample. Interaction between the sample and electrons from the beam produces secondary electrons, which through elastic scattering are reflected (i.e. backscattered). Back scattered electrons (BSE) are detected by the backscatter detector which displays the data as a greyscale BSE image. BSE images show compositional differences in the sample. Atomic number (Z) has a strong influence on the quantity of electrons that are backscattered. Since the BSE detector is sensitive to high Z values, more electrons with high Z 's will be backscattered compared to those with a lower Z . Therefore if an area of the sample contains elements with a high Z (e.g., Fe ($Z \approx 26$)) it will appear brighter on the BSE image and elements with a lower Z (e.g., Si ($Z \approx 14$)) will appear darker (Reed, 2010).

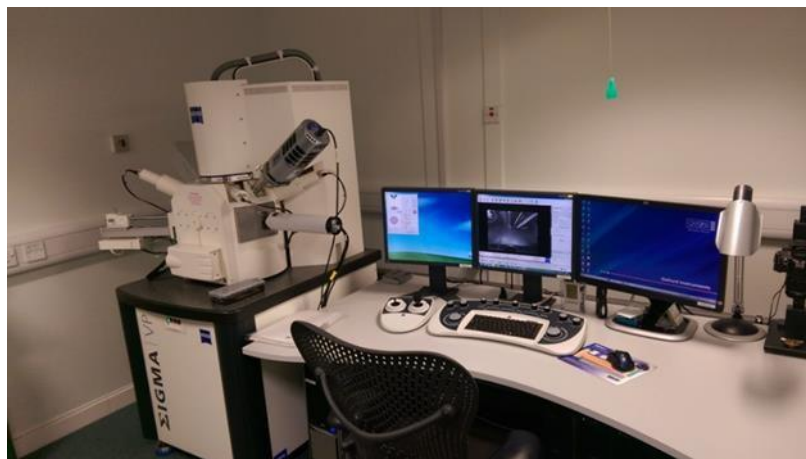


Figure 9: The Carl Zeiss Sigma Variable Pressure Analytical Scanning Electron Microscope at the Imaging Spectroscopy and Analysis Centre (ISAAC) Facility, University of Glasgow.

2.2.2 Energy-Dispersive X-Ray Analysis (EDS) - Imaging

Elemental compositions of samples can be determined by using an Energy-dispersive X-Ray spectrometer (EDS). The EDS at the ISAAC Facility at the University of Glasgow is an 80mm silicon-drift detector.

The EDS allows for the emission of characteristic X-rays from a sample by bombarding the sample with high energy electrons via the electron beam. Prior to electron bombardment, an atom within the sample will contain unexcited electrons in distinct

energy levels/shells (electron orbitals) around the nucleus. An electron beam hitting the sample will result in electron excitation and may cause an electron to be knocked out of its orbital around the nucleus, thus producing a ‘hole’ at the electrons former position. An electron from an outer orbital (higher energy level) will fall into this hole to re-establish equilibrium (e.g., an electron in an inner shell (K shell) is ejected and an electron in a higher energy level (L shell) fills the vacancy, as illustrated in figure 10) (Brownlow; 1996; Oxford Labs, 2017; Robinson, 2000). This difference in energy is emitted in the form of an X-ray. The EDS then measures the number and energy of emitted X-rays from the sample and since X-ray energies are characteristic of certain elements, elemental compositions of the sample can thus be determined by assigning false colours to elements measured (Reed, 2005). Elemental maps for a whole sample can be built up, therefore identifying the relative abundance of selected elements within the whole sample or a selected area. Elemental mapping of both NWA 7034 and NWA 8159 was conducted to highlight apatites and mineralogical/lithological context of both meteorites, EDS images were produced at 250× magnification with 1024 resolution (this data can be viewed in chapter 3).

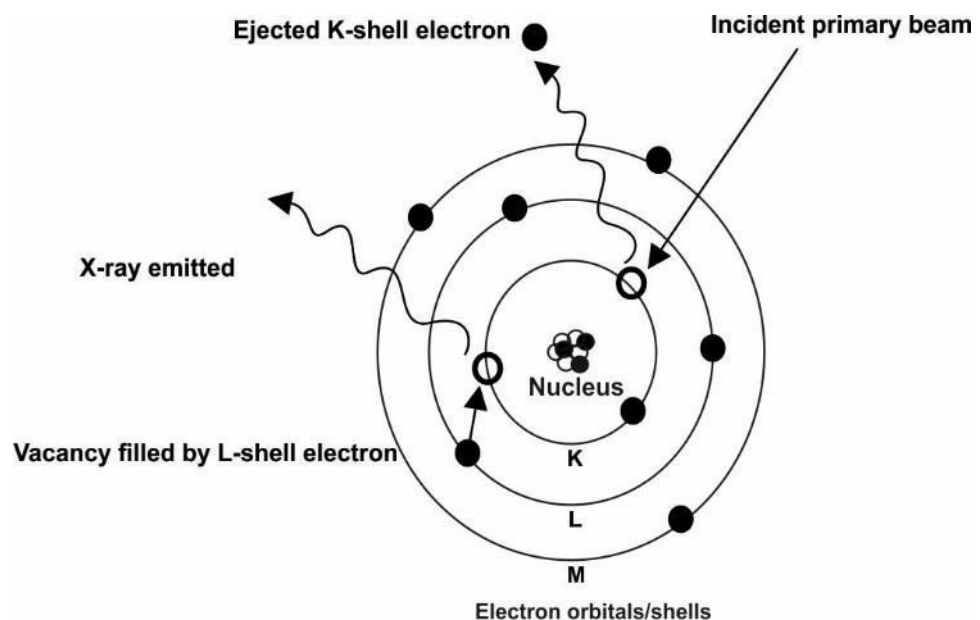


Figure 10: A schematic of the structure of an atom, indicating the nucleus and electron orbitals (K, L and M). Each orbital has a distinct energy level (i.e., K is an electron in ground state, which when excited by a beam, will become excited and move to a higher energy level (L or M)). Electrons from a higher energy level can fill in a vacancy when an electron from a lower energy level has been knocked from its orbital, which releases a characteristic X-ray. Adapted from Oxford labs (2017) and Robinson (2000).

2.2.3 Energy-Dispersive X-ray Analysis (EDS)- Quantitative Chemical Analysis

The largest and most pristine apatite grains were selected for EDS spot analysis to produce quantitative major and minor element data (Si, Al, P, K, Na Ca, Fe, Mg, S, Ti, Mn, Cl and F), with uncertainties of 0.1 wt. % (calculated from the background spectra for each analysed element).

Geo MK II Block standard materials were utilised to ensure the precision of these analyses (table 2). Conditions in the SEM during these quantitative analyses were as follows: 15kV voltage, 8.5mm working distance (WD), 60 μ m aperture. During SEM-EDS point analysis the beam current was ~ 2.22 nA and a spot size of ~10 μ m was used.

Element	Standard
F	Fluorite
Cl	Tugtupite
Mn	Rhodonite
K	Orthoclase
Na and Al	Jadeite
Ti	Rutile
Cr	Chromite
P	Apatite
Ca and Si	Wollastonite
Fe	Haematite
Mg	Periclase
S	Pyrite

Table 2: Geo MK II Block standards used during SEM-EDS analysis to achieve quantitative results at the ISAAC Facility, University of Glasgow. The table lists which standard was used for each element.

2.3 Problems with Measuring Volatiles

Apatite proves to be a problematic mineral to obtain quantitative analysis from as a result of F sensitivity to the electron beam and problems arising from crystal orientation properties. F is especially difficult to analyse accurately due to migration effects (Stormer et al., 1993; Pyle et al., 2002; Henderson, 2011).

2.3.1 Fluorine Migration

Quantitative analysis of F concentrations within apatite are primarily problematic due to the mobility of F under electron bombardment from the primary beam (Henderson, 2011). Previous studies conducted by Stormer et al. (1993) noted increased F X-ray

emissions with exposure time. They accounted these variations to be an effect of beam current and spot size but also confirmed that the crystallographic orientation of apatite has an effect on F analysis. The relationship between increased F X-ray counts and beam voltage was also studied and it was determined that low voltages (7-15 kV) has less of an effect of F migration compared to increased voltages (Henderson, 2011; Stormer et al., 1993).

Stormer et al. (1993), suggested that to obtain an accurate analysis of F concentrations within apatite, multiple timed analysis on the same spot with a note of the beam value at the start of the analysis is favoured rather than a single analyses. This then allows a correction to be applied to your data. McCubbin et al. (2011) modified their data for the variations of F X-ray counts by using a correction in PFE software. The crystallographic orientation of apatite is a more difficult aspect to control. However, McCubbin et al. (2011) determined that changes in the F X-ray count rate did not correlate with the orientation of selected apatites during their analysis. Therefore, it is possible that crystallographic orientation is less of a controlling factor in F migration.

2.3.2 Scanning Electron Microscopy at the Natural History Museum

To attempt to account for F migration (previously discussed) during analysis, collaboration with Dr. Tobias Salge at the Natural History Museum (NHM) was undertaken. A new technique using EDS is being developed at the NHM to try to resolve the F migration problem. Both NWA 7034 samples were analysed using Bruker (Quantax Quad) Esprit 2.1 software via SEM-EDS to collect Cl and F data. Astimex standards were used prior to analysis (listed in table 3). The sample was analysed over small timescales (10 seconds measurement time) with a low beam voltage (6kV). However, the results produced exceptionally high totals (105 wt. %) for both samples of NWA 7034. Previously when the standards had been analysed they had produced totals <100 wt. %. The reason for this difference in total wt. % between the standards and samples was a result of a sample preparation error. The carbon coats on the samples were of a different thickness compared to the standards carbon coating (15nm on samples and 25nm on standards). Therefore, more X-rays from the samples were able to get to the detector compared to the standards, thus resulting in totals that were artificially high. Unfortunately, there was no time to return to the NHM to conduct another study using Dr. Tobias Salges' technique. Therefore, F

migration in the final results could only be accounted for through stoichiometry, described below.

Element	Standard
F	Topaz
Cl	Tugtupite
Si and Mg	Diopside
Ca	Calcite

Table 3: Astimex standards used during SEM-EDS analysis at the Natural History Museum, London. The table lists which standard was used for each element.

2.3.3 Stoichiometry Calculations of Volatile Abundances

SEM-EDS analysis cannot directly measure OH. However, by measuring F and Cl accurately, the missing component (assumed to be OH) can be inferred via stoichiometry (McCubbin et al., 2011). Using guidance from Deer et al. (1992) and McCubbin et al. (2013) stoichiometry from the conducted analysis with wt. % totals ranging from 98.5% - 101% was calculated. Four main steps were used to determine stoichiometry accurately. In apatite, F, Cl and OH are present as anions, as well as the more common O anion. This adds an extra step (step 1) to the stoichiometry calculations, which is to calculate the oxygen equivalent. Since Cl and F are both anions, the amount equivalent to O needs to be calculated (equation 2). Step 2 involves calculating the molecular proportion of oxides for each analysed element (equation 3) followed by Step 3 - which involves calculating the atomic proportion of O from each molecule (equation 4) and the structural formula based on 13 anions (equations 5). The final step (Step 4) involves calculating the structural formula for F and Cl based on 13 anions is required. To do this the true total is needed (equation 6) and the normalisation factor for 13 anions (equation 7) before Step 4 can be applied (equation 8). Once the structural formula for F and Cl based on 13 anions is calculated, a column can be made to add up all the cations and anions for each analysis. For apatite, the total number of cations should equal 8, with Ca and P cations being equal to 5 and 3 respectively. The total number of anions calculated should equal 1. Any value less than 1 will indicate that there is a missing component (i.e., OH). For more insight into this stoichiometry, method refer to Deer et al. (1992) and McCubbin et al. (2013).

Step 1:

$$-O = F = 16 \div 2 \times \text{Atomic mass of F} \times F \text{ oxide wt. \% from analysis}$$

$$-O = F = 16 \div 2 \times \text{Atomic mass of Cl} \times Cl \text{ oxide wt. \% from analysis}$$

Equation 2: Oxygen equivalent calculations for Cl and F based on work by Deer et al. (1992) and McCubbin et al. (2013) where: $-O=F$ and $-O=Cl$ is the oxygen equivalent for F and Cl, respectively; and 16 is the atomic mass of O. Since O has a charge of -2 and Cl and F have a charge of -1, the calculation involves two times the atomic mass of F and Cl, and only 1 times the atomic mass of O (which is 16).

Step 2:

$$\begin{aligned} & \text{Oxide wt. \% in analysis} \div \text{No. of oxygen in analysed oxide} \\ & \times \text{Atomic mass of} + \text{No. of cations in the oxide} \times \text{Atomic mass of} \\ & \text{corresponding cation} \end{aligned}$$

Equation 3: The molecular proportion of oxides calculation (Deer et al., 1992; McCubbin et al., 2013). This calculation should be applied to all elements analysed.

Step 3:

$$\text{Molecular proportion of oxide from an analysed element} \times \text{number of cations in oxide}$$

Equation 4: Calculation for the atomic proportion of O from each molecule (Deer et al., 1992; McCubbin et al., 2013).

$$\begin{aligned} & \text{Atomic proportion of O from each molecule} \times \text{Normalisation factor for 13 anions} \\ & \times (\text{No. of cations} \div \text{No. of oxygen in oxide}) \end{aligned}$$

Equation 5: The calculation for the structural formula based on 13 anions (Deer et al., 1992; McCubbin et al., 2013).

$$\begin{aligned} & \text{Sum of all atomic proportions of O} - \text{Molecular proportion oxide Cl} \\ & + \text{Molecular proportion oxide F} \div 2 \end{aligned}$$

Equation 6: The calculation for the true total (Deer et al., 1992; McCubbin et al., 2013).

$$13 \div \textit{True total}$$

Equation 7: Normalisation factor for 13 anions calculation (Deer et al., 1992; McCubbin et al., 2013)
This is required as the apatite chemical formula contains 13 oxygens.

Step 4:

$$F = \textit{Atomic proportion of O from each molecule} \times \textit{Normalisation factor}$$

$$Cl = \textit{Atomic proportion of O from each molecule} \times \textit{Normalisation factor}$$

Equation 8: The calculation of the structural formula based on 13 anions (Deer et al., 1992; McCubbin et al., 2013). By adding the results from this calculation a total number of anions in the X-site of the apatite can be determined (it should equal 1). A value <1 indicates a missing component (i.e., OH).

2.4 Cameca ims 1280 Ion Microprobe

Apatites >25 μ m from NWA 7034(In) and NWA 7034(Epoxy) were analysed for hydrogen isotope compositions using the Cameca ims 1280 Ion Microprobe at the W.M. Keck Cosmochemistry Laboratory, University of Hawaii (UH). Prior to analysis, the two samples of NWA 7034 were placed at 60°C in a vacuum oven for 48 hours. This method of analysis was selected based on its high accuracy, low contamination, spatial resolution and capability to measure isotopic compositions in situ with a precision and reproducibility of $\pm 0.5\%$ (Hallis et al., 2012a; HIGP, 2017).

2.4.1 Secondary Ion Mass Spectrometry- Analytical Protocol

An ion microprobe (also known as a Secondary Ion Mass Spectrometer (SIMS)) produces a focused primary Cs⁺ beam, which sputters atoms from the sample. During the sputtering process, some of the atoms are ionised, thus producing secondary ions. These secondary ions are then transferred from the sample chamber through an electromagnetic field and to the mass spectrometer, where they are identified at the detector based on their mass/charge ratio (Peres et al., 2008). The sputtering process produces ions of every element and therefore the SIMS must have a high mass resolving power to cope with this as it must be sufficient enough to be able to separate interfering molecules to yield high precision data (Hallis et al., 2012b; HIGP, 2017). The Cameca ims 1280, at UH (figure 11) has a mass resolving power of 6000, therefore is ideal for high precision measurements.

Collection of high precision isotopic analysis on the Cameca ims 1280 is conducted in microprobe mode. When conducting hydrogen isotope (D/H) analyses, the primary ion column generates the Cs⁺ beam, which is used to measure elements that have negative ions (negative ions are measured as they are the resultant of the ionisation from a positively charged beam) (SERC, 2017). There are 3 main detectors of ions on the Cameca ims 1280: a Faraday Cup, a multicollector and the SCAPS detector (HIGP, 2017).

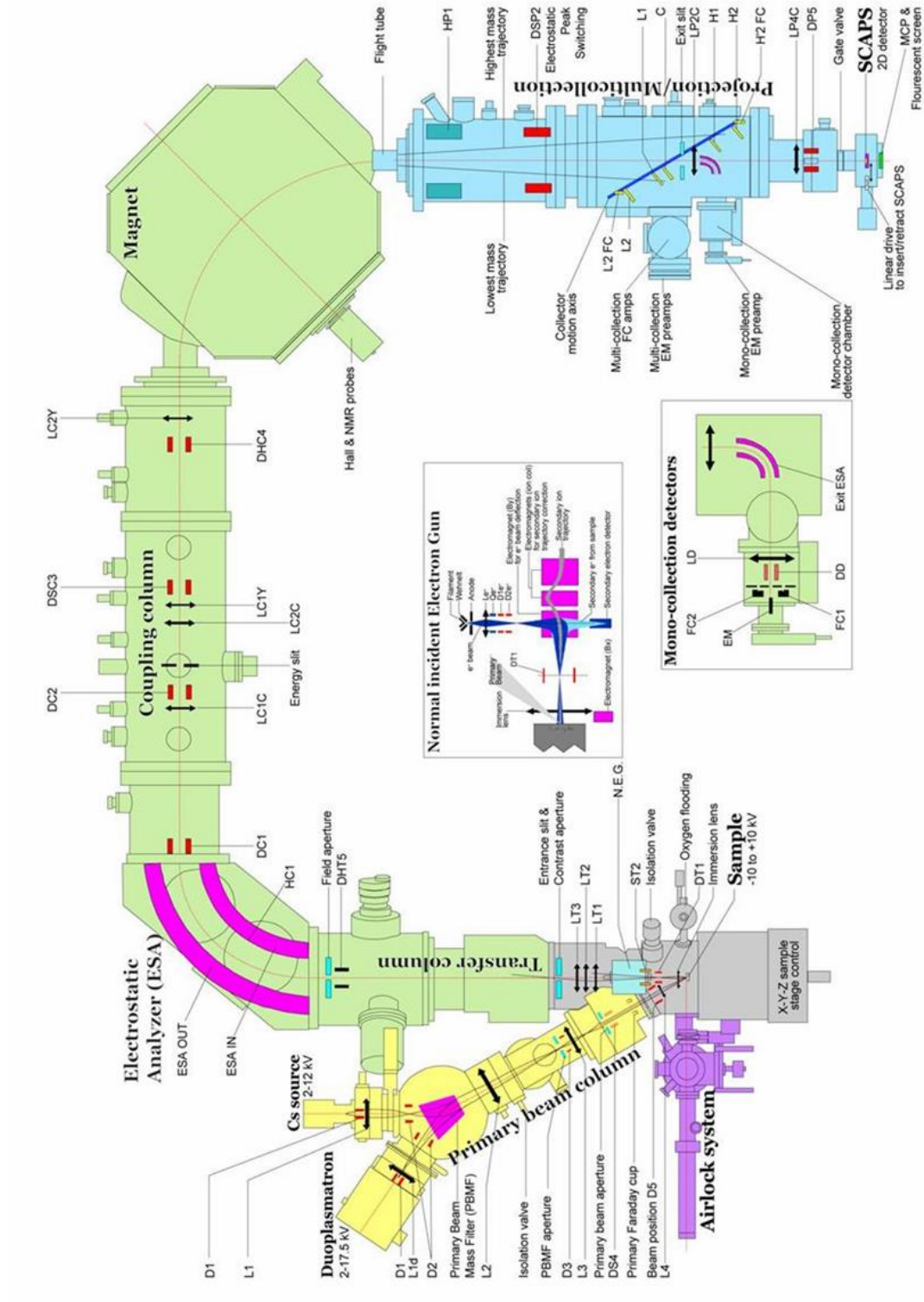


Figure 11: Schematic of the Cameca ims 1280 ion microprobe at the University of Hawaii. The main features of this ion microprobe are the sample chamber and air lock (purple); primary ion column (yellow); Secondary Ion Mass Spectrometer (green); detectors (blue) (HGIP, 2017). The sample chamber operates with a vacuum of $\sim 1 \times 10^{-9}$ torr and allows for one sample in the chamber at a time, and a reserve sample in the airlock. The SIMS detector is double focussing, with an electrostatic and magnetic sector in a forward geometry (i.e., the electrostatic sector is before the magnetic sector). This geometry allows for the reduction of energy of the secondary ions (via the electrostatic sector) prior to separation to single ion beams in the magnetic sector (Shimizu, 1997).

In-situ H isotopic compositions of apatite were analysed using the Cameca ims 1280 Ion Microprobe at the W.M. Keck Cosmochemistry Laboratory, UH. A focused Cs⁺ primary ion beam with a current of 4nA produced ions of H, D and ¹⁸O. The measurement protocol involved the primary ion beam being rastered over an area of 25 × 25µm for 200s. This process ensured the removal of surface contamination on the sample as well as removing the 15nm carbon coat covering the apatite. The raster area was then reduced to an analysis area of 15 × 15µm. The final spot size that data was collected from was 8 × 8µm, due to the presence of an egate excluding ions from the outer regions of the 15µm analysis raster (Hallis et al., 2015). This rastering and sputtering process is illustrated in figure 12. The collection of data occurred over a period of 40 cycles with element measurement times displayed in table 4. H is more abundant than D and therefore H was measured over a shorter time and D measured over a longer time to ensure D counts were above the detection limits. The 40 cycles were separated into background data and real data. In cycles 1-9 and 36-40, the beam was blanked and therefore during these cycles the background H and D was measured. In cycles 10-35 the beam was turned on and collected data from the sample.

Element	Measurement Time
¹ H	3 seconds
² H (D)	40 seconds
¹⁸ O	2 seconds

Table 4: Measurement times for selected elements for analysis. Since Deuterium (²H or D) is less abundant than Hydrogen (¹H) it is measured over a longer period of time (e.g., 40 seconds) compared to hydrogen, which is measured for a shorter time (3 seconds). Since ¹⁸O is abundant it was measured over a short time (2 seconds) similar to ¹H.

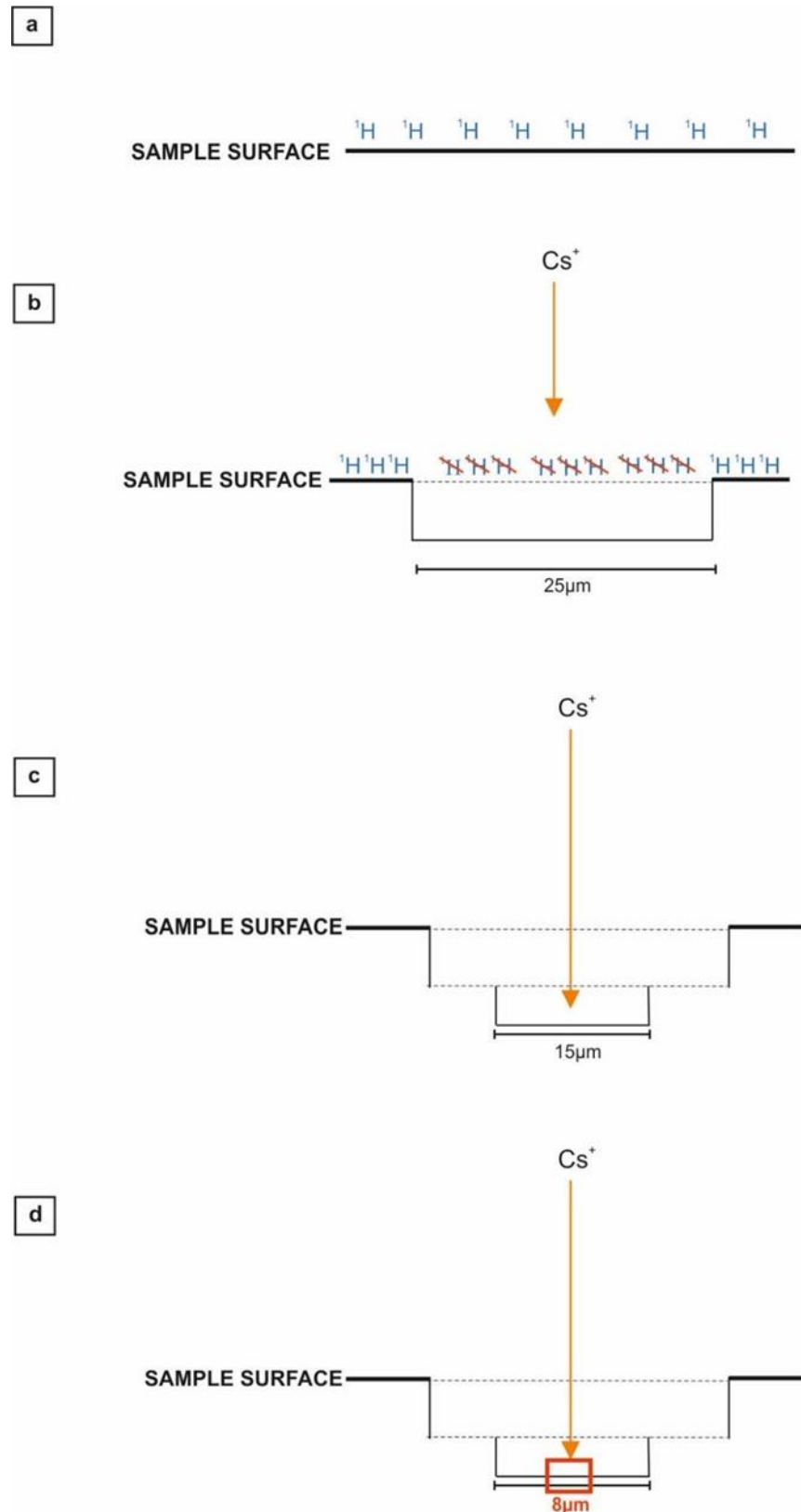


Figure 12: A simplified schematic of the sputtering and rastering process, which occurs during analysis. The primary ion beam is rastered over a $25 \times 25\mu\text{m}$ area for 200s to remove the carbon coating over the apatite and surface contamination (b), the raster area is then reduced to an area of $15 \times 15\mu\text{m}$ (c) and then to an $8 \times 8\mu\text{m}$ area for analysis (d).

Ion probe data is recorded in counts per second (cps). This raw data is corrected for both deadtime and background. Background was measured during the first 10 and last 5 cycles of each measurement as previously stated, which was subtracted from the isotopic data, measured during cycles 10 and 35. To correct for instrumental mass fraction, three terrestrial standards were used. Two of which were apatite standards: Crystal Lode ap005 and Russia ap018 and the other standard used was San Carlos olivine. The San Carlos olivine standard contains no H (olivine is an anhydrous mineral) therefore by measuring the H content of the standard the level of H in the vacuum can be estimated. Standards were re-measured after analysis to ensure the conditions in the vacuum were constant during data collection. McCubbin et al. (2010, 2012) previously measured the δD value and water content of these standards as shown in table 10. Since each of these standards have varying water contents, a calibration line can be produced (figure 13), which was used to estimate the water content of the unknowns based on the unknowns 1H-/18O- ratio, and the slope of the relevant 1H/18O vs. H₂O wt.% standard calibration line, using the following equation:

$$H_2O \text{ wt. \%} = ({}^1H^-/{}^{18}O^-) \times \text{line slope}$$

Equation 9: The water content of the unknown apatites where 1H-/18O- ratio and the slope of the 1H/18O vs. H₂O wt. % standard calibration line estimated the unknown water content (Hallis et al., 2012).

The reproducibility of apatite water content analysis, determined through the uncertainty associated with the standard calibration line, was $\pm 19.5\%(2\sigma)$.

Following this, 2σ errors for H₂O and δD of each apatite were calculated using the equation:

$$Error = 2 \times \text{standard deviation}(\text{estimated} - \text{true})$$

Equation 10: Reproducibility of apatite water content and δD values, where estimated is the estimated H₂O or δD value of each apatite standard and true is the H₂O or δD value of each apatite standard (Hallis et al., 2012).

$$2\sigma \text{ error} = 2 \times \sqrt{\text{measurement error}^2 + \text{reproducibility of standards}^2}$$

Equation 11: The 2σ error for H₂O and δD of each apatite (Hallis et al., 2012).

The H₂O detection limit was calculated using the $^1\text{H}/^{18}\text{O}$ ratios from anhydrous minerals. The detection limit for NWA 7034(In) was ~465 ppm and ~190ppm for NWA 7034(Epoxy).

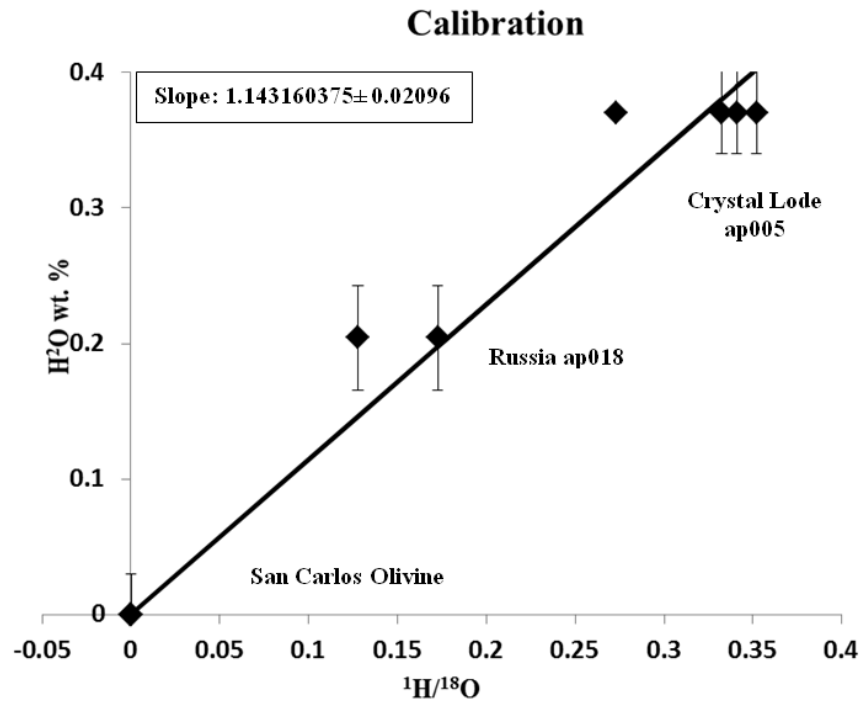


Figure 13: Calibration line for apatite in NWA 7034. The line is based on analysis of terrestrial standards with known water contents (table 11).

Chapter 3 Volatile Abundance Apatite Data

3.1 Volatile Content within Apatite in NWA 7034

EDS false colour X-ray images indicate the various minerals and clasts present within two samples of NWA 7034 (figure 14 and 15). Figure 14 highlights the lithological context of NWA 7034 (Indium mounted sample), showing its clastic nature with protobreccia clasts, melt clasts and mineralogical clasts present. Figure 15 also highlights this for NWA 7034 (Epoxy mounted sample). From Energy dispersive false colour X-ray images (figures 14 and 15), it is clear that there is abundant phenocrysts of plagioclase (~200- 500 μ m) and pyroxene (~100-600 μ m) present within NWA 7034 (plagioclase indicated blue in figure 14 and indicated by dark green in figure 15).

The location and lithological context of the apatites in NWA 7034 was determined using EDS mapping. Figure 16 indicates the location of apatites within NWA 7034(In) and figure 17 indicates the location of apatites within NWA 7034(Epoxy).

Further EDS mapping was conducted on an individual apatite grain (ROI_1a) of interest (figures 18 and 19) from NWA 7034 (Epoxy). This apatite displayed white veining on its surface on a BSE image so EDS mapping was conducted to determine the composition of the veins. EDS maps indicated the veining present was Fe-rich, which has not been previously noted by other studies (figure 18 and 19). It is possible that this veining is a result of hydrothermal alteration. Some of the Fe-rich veins are offset by the fracture in ROI_1a, indicating that hydrothermal alteration occurred prior to the formation and/or ejection of NWA 7034. Hydrothermal alteration prior to incorporation into NWA 7034 is consistent with McCubbin et al. (2016), and implies that the whole rock of NWA 7034 may have experienced hydrothermal alteration. However, a more likely explanation for the Fe-rich veins is shock blackening (Baziotis et al., 2013; Summerson et al., 2013).

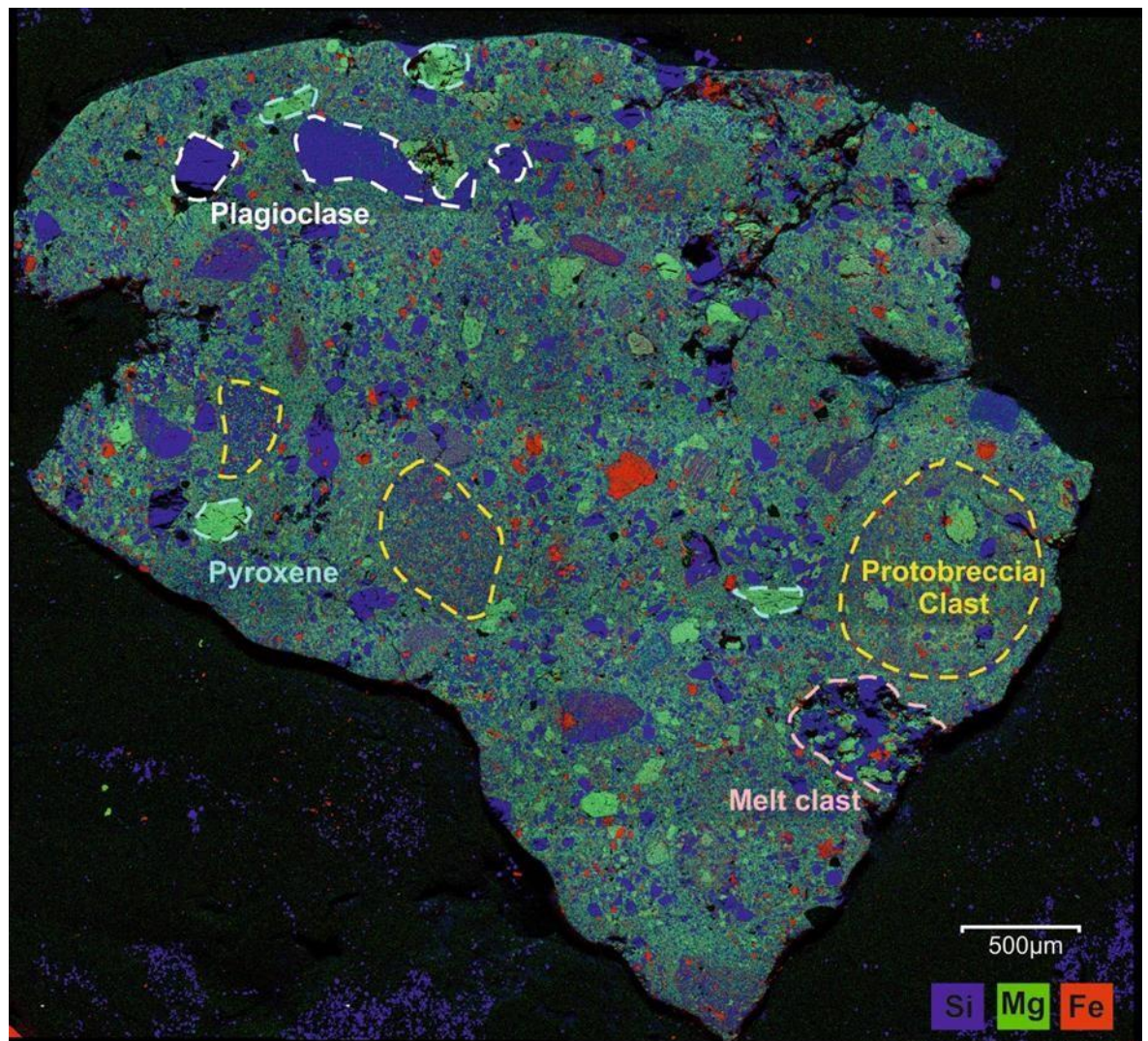


Figure 14: Energy-dispersive X-ray analysis compositional map of NWA 7034 (indium mounted sample). Composition: Silica: blue, Magnesium: green and Iron: red. Bright green areas correspond to pyroxene, mostly present as large (~100-600µm) mono-mineralic clasts. Red areas represent magnetite, and blue areas are either plagioclase (~200-500µm) or silica rich glass produced via shock. Some of the various clast types present in NWA 7034 are displayed in the above figure: protobreccia clasts (yellow dashed line), melt clast (pink dashed line) and mineral clasts (plagioclase in the white dashed line and pyroxene in the light blue dashed line).

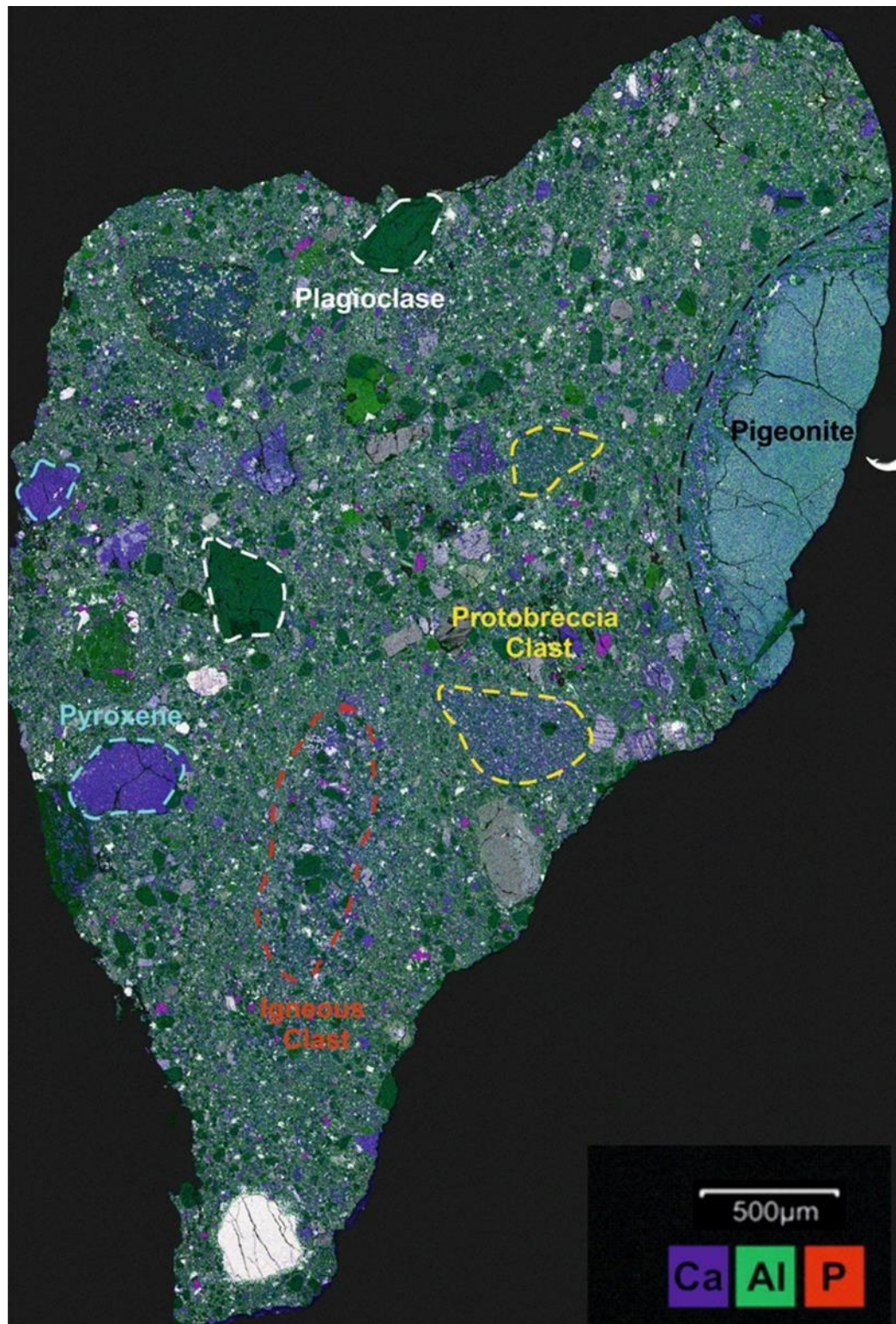


Figure 15: Energy-dispersive X-ray analysis compositional map of NWA 7034 (epoxy mounted sample). Composition: Calcium: blue, Aluminium: green and Phosphorus: red. Bright blue areas correspond to pyroxene, present as ~100-500 μm mono-mineralic clasts. Dark green areas are predominantly plagioclase, with large phenocrysts ranging from ~200-300 μm. Dark pink areas represent small apatite grains (~25 μm). Various clast types present can be noted in the above figure: protobreccia clasts (yellow dashed line), a coarse igneous clast (red dashed line) and mineral clasts (Pigeonite in the black dashed line, plagioclase in the white dashed line and pyroxene in the light blue dashed line).

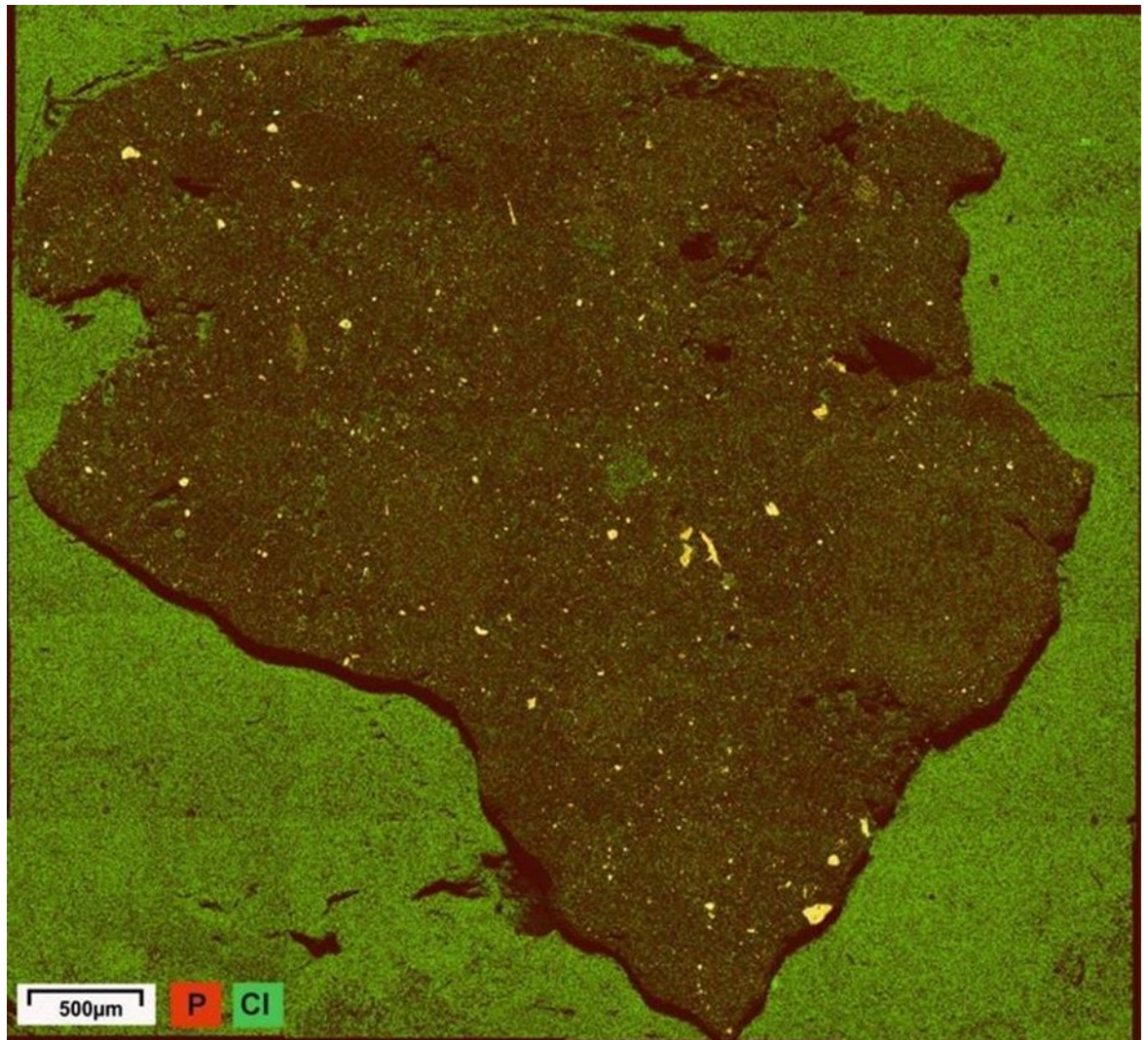


Figure 16: Energy-dispersive X-ray analysis compositional map of NWA 7034 (In). Composition: Phosphorous: red and chlorine: green. Apatite grains are highlighted in yellow due to the false colour overlay of phosphorus (red) and chlorine (green), two diagnostic elements that make up apatite.

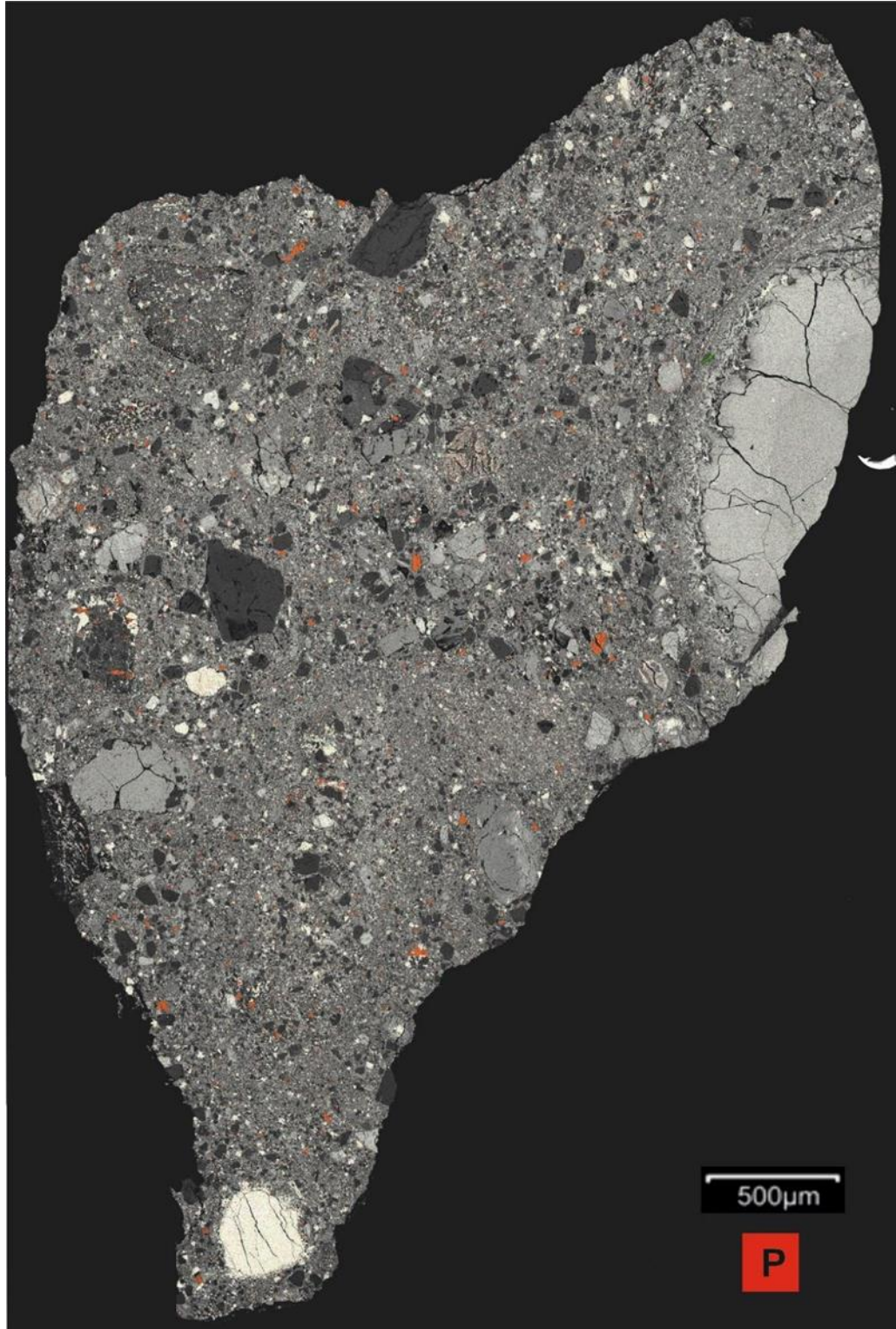


Figure 17: Energy-dispersive X-ray analysis compositional map of NWA 7034 (Epoxy). Composition: Phosphorous: red. Thus, red grains indicated in the EDS map are apatite.

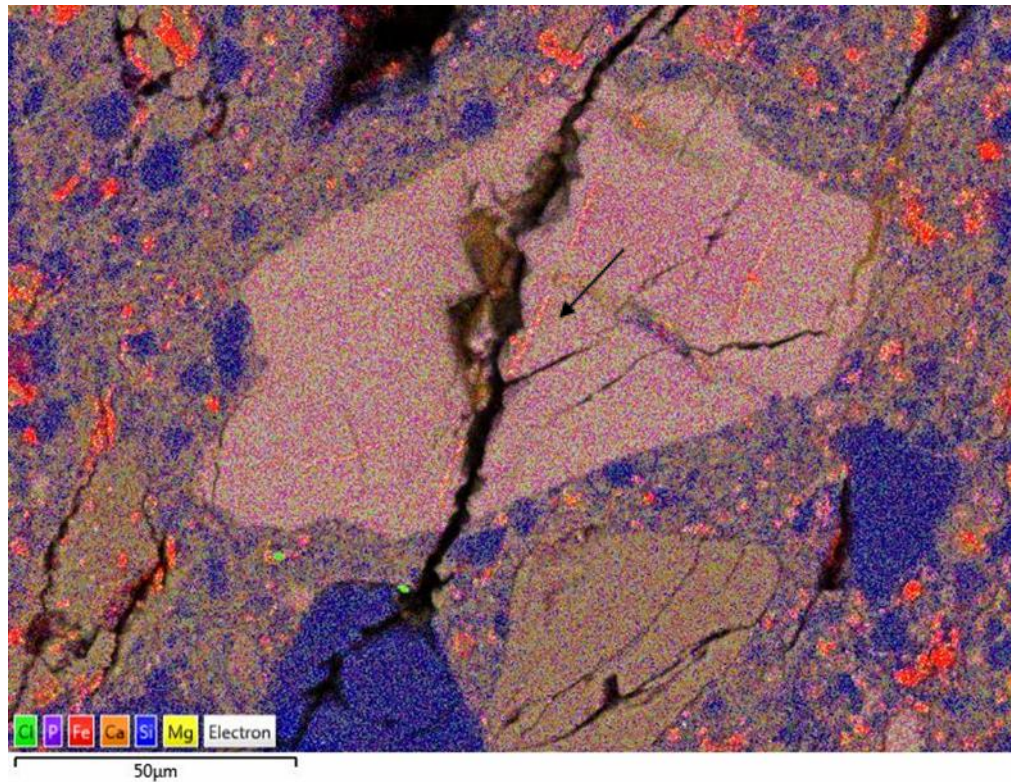


Figure 18: Energy-dispersive X-ray analysis compositional map of an apatite (ROI_1a) within NWA 7034 (Epoxy) showing signs of shock blackening (see black arrow). Composition: Chlorine: green, Phosphorous: purple, Iron: red, Calcium: orange, Silica: blue and Magnesium: yellow.

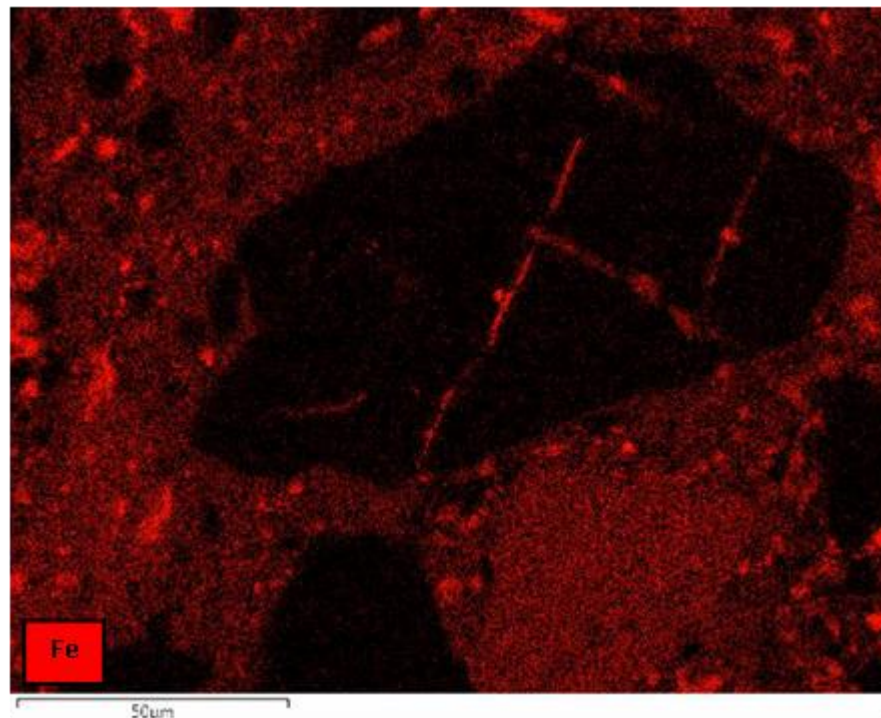


Figure 19: Energy-dispersive X-ray analysis compositional Fe map of an apatite (ROI_1a) within NWA 7034 (Epoxy) showing signs of shock blackening. Lines of interest are iron rich.

3.1.1 Targeted Apatites for Volatile Abundance Analysis

The apatites selected for SEM-EDS analysis are displayed in figures 20 to 22 (with the exception of ROI_2 and ROI_8 in figure 20- these apatite grains were selected for hydrogen isotope analysis (see Chapter 4)). Figure 20 shows the apatites selected from NWA 7034 (In). The texture of these apatites varies from spongy (ROI_1 and 2), anhedral (ROI_4, Std run 10, and 12) and euhedral (ROI_8 and Std run 11) ROI_1 and 2 appear to be included in a pyroxene mineral clast. Both of these apatites display a spongy texture and seem to have grown from the matrix around the pyroxene. The rest of the apatites analysed in the NWA 7034(In) sample were free grains within the matrix. Figures 21 and 22 show apatites selected from NWA 7034 (Epoxy). Texturally, the apatites in this sample are predominately euhedral (ROI_1a, 3, 5, 8a, 11, 12 and 13) with some anhedral (ROI_2a, 4a, 6a, and 7). In this sample all apatites analysed were in the matrix on the sample, with exception to ROI_8a which was contained within a rim of a pigeonite mineral clast. All targeted apatites were $>25\mu\text{m}$ to avoid matrix incorporation during analysis.

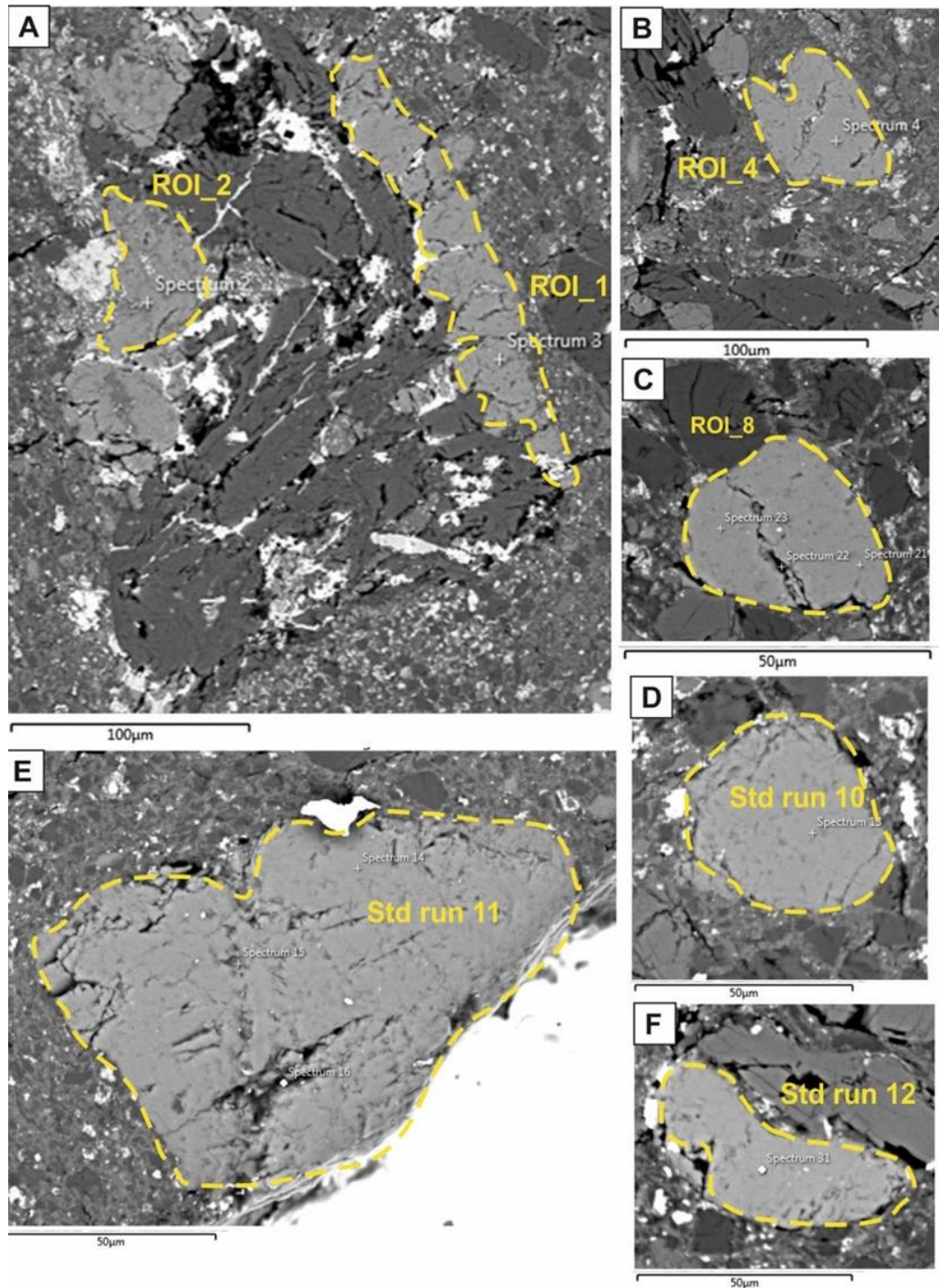


Figure 20: BSE images of apatites of interest in NWA 7034 (In). Yellow dashes outline the grain boundary of the apatite to surrounding minerals and matrix material. Each apatite was selected as a “region of interest” (ROI). Spectrum labels indicate where previous SEM-EDS point analysis was conducted. (A) Highlights ROI_1 and 2 apatites contained within a pyroxene clast. The results of SEM-EDS analysis of ROI_2 are not displayed in the triplot below due to low overall totals (< 96%), however this apatite was selected for hydrogen isotope analysis. (B) Shows ROI_4, which is a free apatite grain within the matrix. (C) Highlights ROI_8, a euhedral, free apatite grain within the matrix. A prominent fracture is shown through the apatite, however the surface on either side is relatively clean. The results of SEM-EDS analysis of this apatite are not displayed in the triplot below due to low overall totals (< 96%), however this apatite was selected for hydrogen isotope analysis. (D) Indicates Std run 10, an anhedral free apatite grain. (E) Highlights Std run 11, a euhedral apatite positioned at the sample edge. (F) Shows Std run 12, an anhedral free apatite grain.

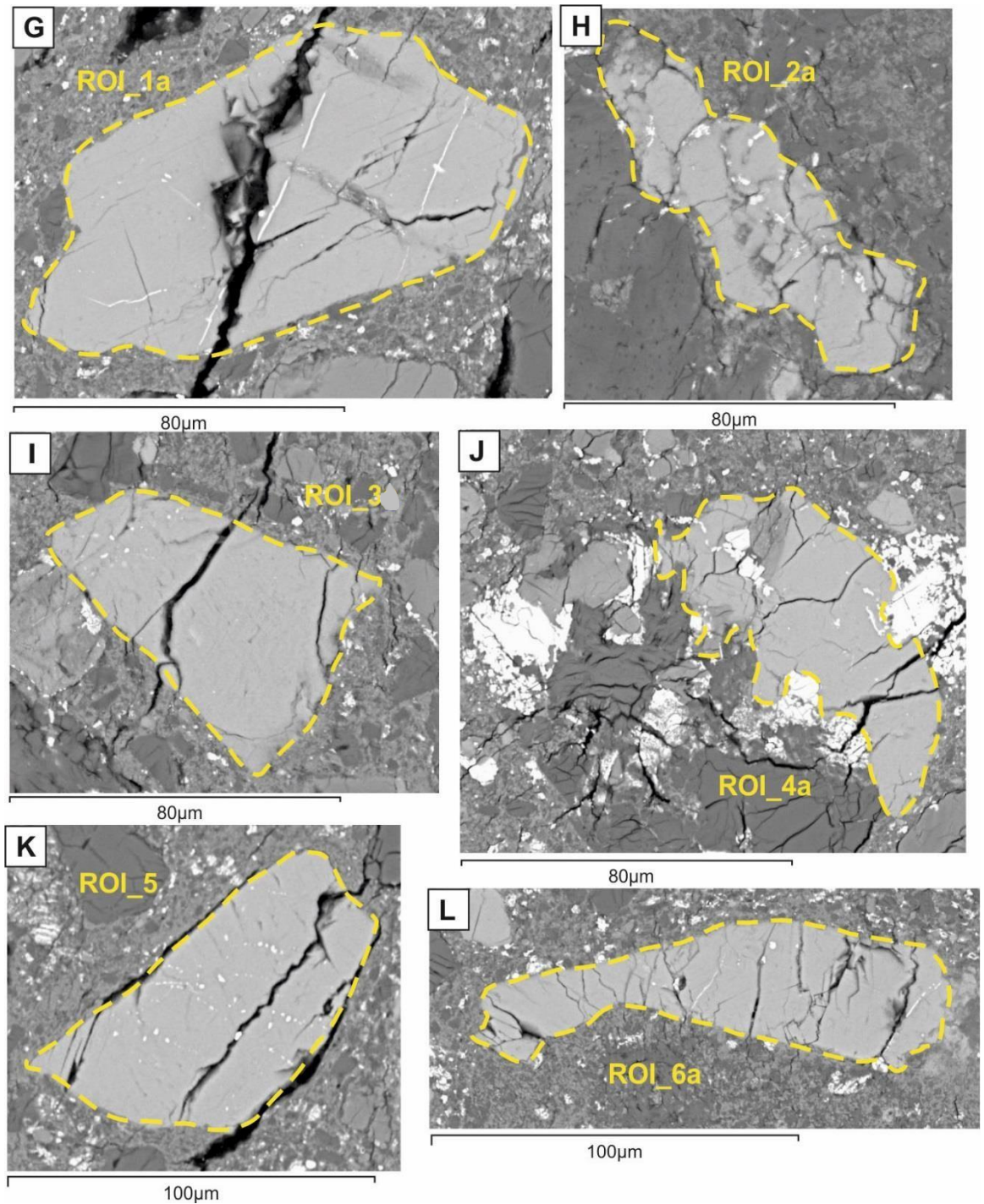


Figure 21: BSE images of apatites of interest in NWA 7034 (Epoxy). Yellow dashes outline the grain boundary of the apatite to surrounding minerals and matrix material. Each apatite was selected as a “region of interest” (ROI). Spectrum labels indicate where previous SEM-EDS point analysis was conducted. (G) Highlights ROI_1a, a euhedral apatite grain with a prominent crack along the surface. Thin white veins can be seen on the surface of the apatites (previously explained in section 1.2.4). (H) shows ROI_2a, an anhedral free apatite grain within the matrix. (I) Highlights ROI_3, a prominent feature of this apatite is the fracture across the surface. White inclusions (possibly silicates) are present to the left side of the fracture, whereas the surface to the right side of the fracture appears relatively clean. (J) Shows ROI_4a, an anhedral apatite that appears to have been broken up. (K) Highlights ROI_5, again this apatite as a dominant fracture, with silica inclusions present on both sides of the fracture. (L) Displays ROI_6a, an anhedral apatite grain within the matrix of NWA 7034.

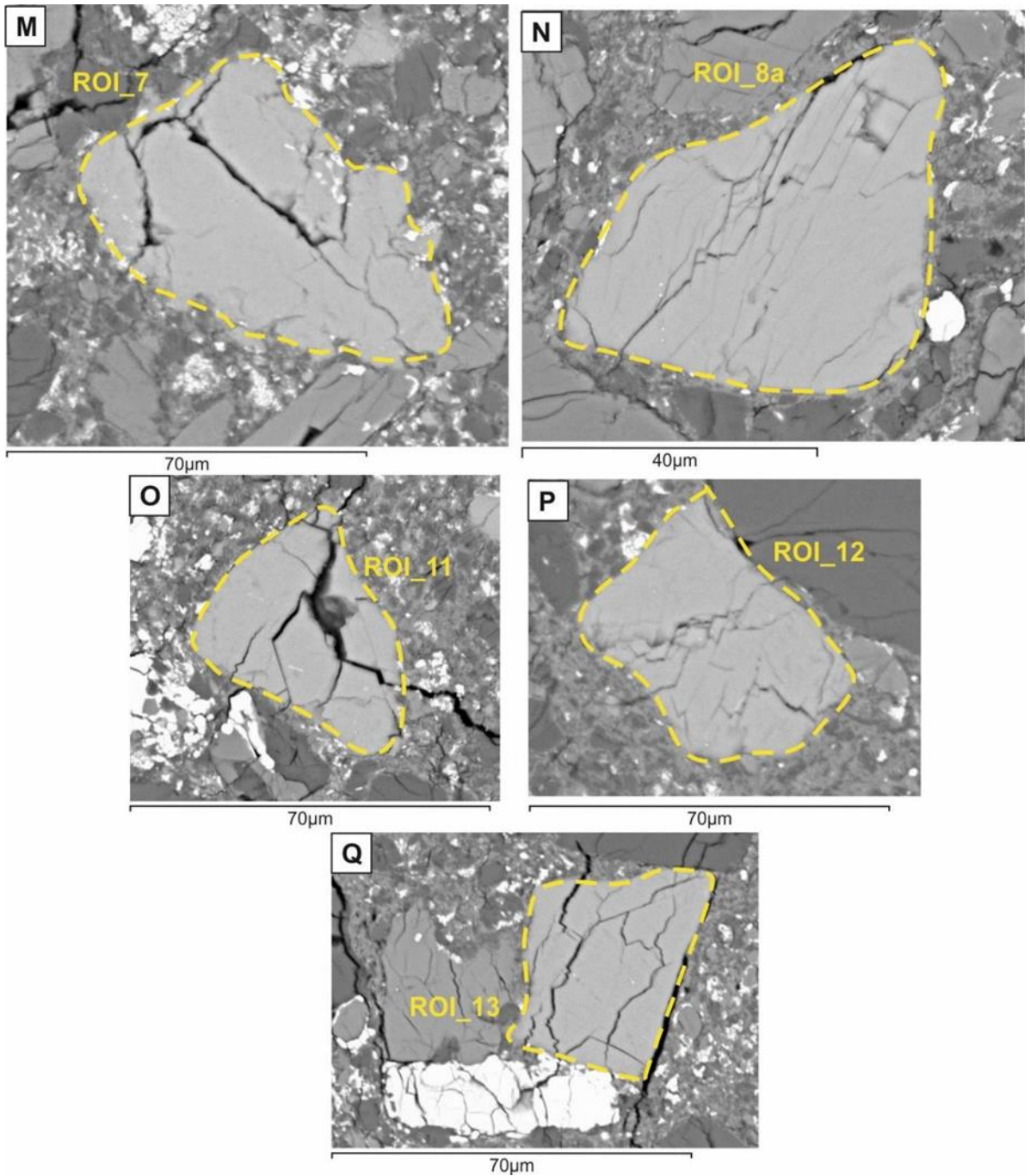


Figure 22: BSE images of apatites of interest in NWA 7034 (Epoxy). Yellow dashes outline the grain boundary of the apatite to surrounding minerals and matrix material. Each apatite was selected as a “region of interest” (ROI). Spectrum labels indicate where previous SEM-EDS point analysis was conducted. (M) Highlights ROI_7, a fractured anhedral apatite grain within the matrix. (N) Shows ROI_8a, a euhedral apatite located in the rim of a pigeonite mineral clast. (O)- (Q) Highlights ROI_11, 12 and 13. All euhedral free apatite grains within the matrix.

3.1.2 Plotted Volatile Abundances for Stoichiometry Calculated OH Component

The volatile abundance results from analysis via SEM-EDS are displayed in figure 23. The data presented in the triplot has been calculated using stoichiometry (previously discussed in section 2.3.3) and therefore represents a proportional ratio of the Cl: F: OH components within the apatite. The data used in the triplot is highlighted in yellow in tables 5, 6 and 7.

Since NWA 7034 is a breccia it was expected that different populations of apatite would exist however, NWA 7034 is uncharacteristically uniform for a polymict breccia (i.e., no groupings of apatite can be seen in terms of their volatile abundances (Cl: F: OH)). NWA 7034 apatites dominantly occupy the Cl-rich region of the triplot, which is consistent with the literature (Santos et al., 2013). A variation can be noted in the OH component of the apatites (highlighted yellow in tables 5, 6 and 7) which has resulted in the spread of data in figure 23. When these results are compared to the results from Santos et al. (2013) the data fits reasonably well (figure 24), with some apatites from this study plotting just outside of the spread of Santos et al. (2013) data. Apatites from this study predominantly plot in the green area of the Santos et al. (2013) triplot. This implies that these apatites formed from a melt which had a volatile abundance of Cl>OH>F. The apatites, which plot in the blue area of the triplot, are inferred to have crystallised from an OH rich melt (OH>Cl>F). McCubbin et al. (2016) previously recorded values of Cl and F abundances within apatite in NWA 7034. Their values indicated Cl ranging from 3.42 to 5.31 wt. % and F ranging from 0.51 to 1.42 wt. %. Values of Cl and F wt. % abundances from this study are highlighted in blue in tables 5, 6 and 7 and are consistent with McCubbin et al. (2016) analysis.

Although electron microprobe analyses are typically performed to determine apatite Cl and F abundances, UoG SEM-EDS data is consistent with Santos et al. (2013) and McCubbin et al. (2016) indicating that SEM-EDS analysis of Cl and F measurements are valid and can yield accurate stoichiometry.

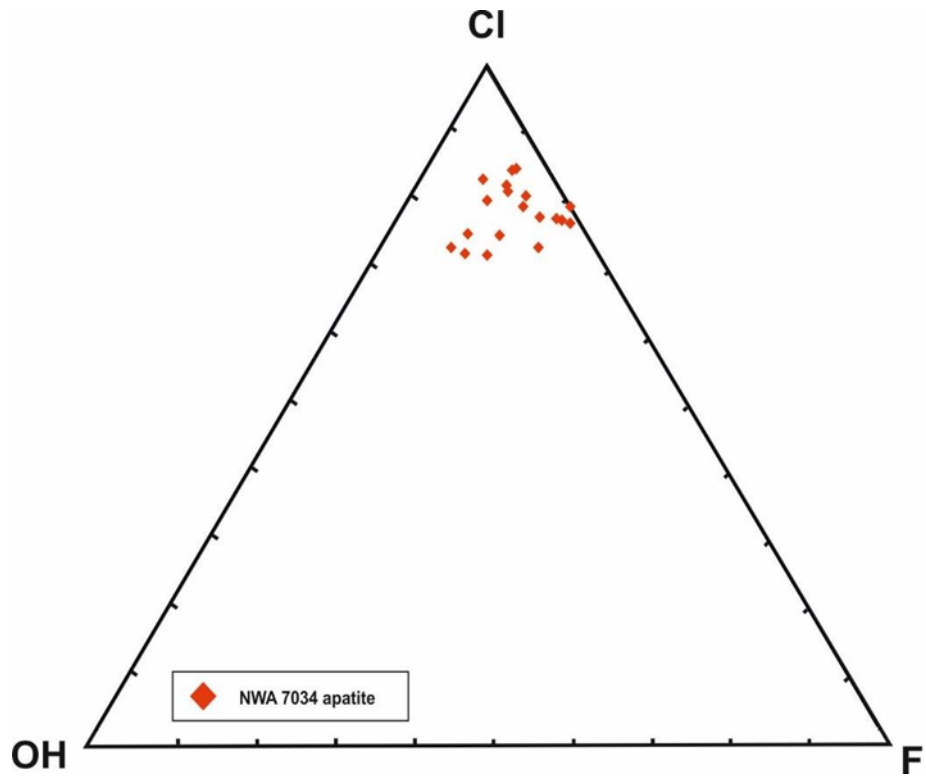


Figure 23: Plotted volatile abundances on a relative volatile abundance (RVA) diagram from apatites in NWA 7034. The values used in this plot (tables 5, 6 and 7) were calculated using stoichiometry methods previously discussed in section 2.3.3. The spreadsheet for this triplot can be viewed on the supplementary disk.

A	Oxide (wt.%)	ROI 1	ROI 4	Std run 10	Std run 11	Std run 12
	SiO ₂	0.00	0.00	0.00	0.00	0.49
	TiO ₂	0.03	0.01	0.03	0.00	0.02
	Al ₂ O ₃	0.14	0.12	0.09	0.04	0.08
	Cr ₂ O ₃	0.00	0.04	0.00	0.00	0.00
	FeO	0.95	0.53	0.52	0.50	0.72
	MnO	0.00	0.00	0.00	0.00	0.00
	MgO	0.16	0.07	0.06	0.07	0.04
	CaO	52.81	53.01	53.37	52.35	53.38
	Na ₂ O	0.21	0.21	0.18	0.22	0.24
	K ₂ O	0.04	0.01	0.01	0.02	0.04
	P ₂ O ₅	39.32	39.58	39.41	38.47	39.73
	S	0.12	0.11	0.14	0.06	0.15
	Cl	5.14	5.30	4.82	5.51	4.88
	F	0.65	0.77	0.73	0.40	0.33
	-O=F	0.27	0.33	0.31	0.17	0.14
	-O=Cl	1.16	1.20	1.09	1.24	1.10
	Total	101.00	101.28	100.77	99.06	101.32

B		ROI 1	ROI 4	Std run 10	Std run 11	Std run 12
	Si	0.00	0.00	0.00	0.00	0.04
	Ti	0.00	0.00	0.00	0.00	0.00
	Al	0.01	0.01	0.01	0.00	0.01
	Cr	0.00	0.00	0.00	0.00	0.00
	Fe	0.07	0.04	0.04	0.04	0.05
	Mn	0.00	0.00	0.00	0.00	0.00
	Mg	0.02	0.01	0.01	0.01	0.00
	Ca	5.01	5.01	5.07	5.08	5.02
	Na	0.04	0.04	0.03	0.04	0.04
	K	0.00	0.00	0.00	0.00	0.00
	P	2.95	2.96	2.96	2.95	2.95
	S	0.00	0.00	0.00	0.00	0.00
	Σ Cations	8.11	8.07	8.11	8.12	8.13
	Cl	0.77	0.79	0.72	0.84	0.73
	F‡	0.18	0.22	0.20	0.12	0.09
	Σ X-site	0.95	1.01	0.93	0.96	0.82
	OH†	0.05	0.00	0.07	0.04	0.18

Table 5: Stoichiometry calculations from SEM-EDS data from apatites within NWA 7034(In). (A) Displays the oxide wt. % of each element analysed, along with the oxygen equivalent (-O=F and -O=Cl, previously discussed in section 2.3.3). Values of Cl and F wt. % abundances from each analysis are highlighted in blue. (B) Displays the structural formula based on 13 anions for each analysed element. The Cl, F and OH values, calculated from stoichiometry, are highlight in yellow. These values are plotted in figure 23.

A	Oxide (wt.%)	ROI 1a	ROI 2a	ROI 3	ROI 4a	ROI 5
	SiO ₂	0.05	0.61	0.52	0.24	0.42
	TiO ₂	0.00	0.00	0.00	0.00	0.05
	Al ₂ O ₃	0.09	0.10	0.15	0.14	0.12
	Cr ₂ O ₃	0.01	0.00	0.00	0.06	0.03
	FeO	0.41	0.47	0.59	0.88	0.88
	MnO	0.00	0.00	0.00	0.00	0.00
	MgO	0.06	0.12	0.03	0.07	0.13
	CaO	53.21	52.43	53.05	52.43	52.11
	Na ₂ O	0.17	0.16	0.21	0.25	0.15
	K ₂ O	0.02	0.02	0.00	0.01	0.00
	P ₂ O ₅	39.34	38.30	38.03	38.76	38.07
	S	0.00	0.09	0.12	0.20	0.01
	Cl	5.43	5.16	5.05	5.55	5.28
	F	0.42	0.54	0.73	0.40	0.43
	-O=F	0.18	0.23	0.31	0.17	0.18
	-O=Cl	1.23	1.16	1.14	1.25	1.19
	Total	100.62	99.38	99.93	100.40	99.07

B		ROI 1a	ROI 2a	ROI 3	ROI 4a	ROI 5
	Si	0.00	0.05	0.05	0.02	0.04
	Ti	0.00	0.00	0.00	0.00	0.00
	Al	0.01	0.01	0.02	0.01	0.01
	Cr	0.00	0.00	0.00	0.00	0.00
	Fe	0.03	0.04	0.04	0.07	0.07
	Mn	0.00	0.00	0.00	0.00	0.00
	Mg	0.01	0.02	0.00	0.01	0.02
	Ca	5.06	5.05	5.10	5.02	5.05
	Na	0.03	0.03	0.04	0.04	0.03
	K	0.00	0.00	0.00	0.00	0.00
	P	2.96	2.92	2.89	2.93	2.91
	S	0.00	0.00	0.00	0.00	0.00
	Σ Cations	8.10	8.11	8.14	8.12	8.13
	Cl	0.82	0.79	0.77	0.84	0.81
	F‡	0.12	0.15	0.21	0.11	0.12
	Σ X-site	0.93	0.94	0.97	0.95	0.93
	OH†	0.07	0.06	0.03	0.05	0.07

Table 6: Stoichiometry calculations from SEM-EDS data from apatites within NWA 7034(Epoxy). (A) Displays the oxide wt. % of each element analysed, along with the oxygen equivalent (-O=F and -O=Cl, previously discussed in section 2.3.3). Values of Cl and F wt. % abundances from each analysis are highlighted in blue. (B) Displays the structural formula based on 13 anions for each analysed element. The Cl, F and OH values, calculated from stoichiometry, are highlight in yellow. These values are plotted in figure 23.

Oxide (wt. %)	ROI 6a	ROI 7	ROI 8a	ROI 11	ROI 12	ROI 13
SiO ₂	0.24	0.19	0.43	0.43	0.38	0.46
TiO ₂	0.00	0.00	0.00	0.00	0.01	0.02
Al ₂ O ₃	0.06	0.02	0.08	0.07	0.12	0.00
Cr ₂ O ₃	0.01	0.08	0.04	0.01	0.03	0.09
FeO	0.64	0.56	0.62	1.01	0.41	0.99
MnO	0.00	0.00	0.00	0.00	0.00	0.00
MgO	0.02	0.06	0.09	0.05	0.07	0.10
CaO	52.92	53.58	52.10	52.36	52.82	52.48
Na ₂ O	0.22	0.16	0.18	0.17	0.22	0.16
K ₂ O	0.00	0.00	0.00	0.02	0.00	0.00
P ₂ O ₅	39.40	40.23	38.64	38.73	39.52	39.16
S	0.00	0.08	0.15	0.01	0.00	0.03
Cl	5.36	4.82	4.88	5.07	4.97	5.28
F	0.53	0.52	0.51	0.75	0.37	0.36
-O=F	0.22	0.22	0.21	0.32	0.15	0.15
-O=Cl	1.21	1.09	1.10	1.14	1.12	1.19
Total	100.84	101.61	99.02	100.14	100.20	100.47

	ROI 6a	ROI 7	ROI 8a	ROI 11	ROI 12	ROI 13
Si	0.02	0.02	0.04	0.04	0.03	0.04
Ti	0.00	0.00	0.00	0.00	0.00	0.00
Al	0.01	0.00	0.01	0.01	0.01	0.00
Cr	0.00	0.01	0.00	0.00	0.00	0.01
Fe	0.05	0.04	0.05	0.08	0.03	0.07
Mn	0.00	0.00	0.00	0.00	0.00	0.00
Mg	0.00	0.01	0.01	0.01	0.01	0.01
Ca	5.02	5.02	5.02	5.01	5.01	4.99
Na	0.04	0.03	0.03	0.03	0.04	0.03
K	0.00	0.00	0.00	0.00	0.00	0.00
P	2.95	2.98	2.95	2.93	2.96	2.95
S	0.00	0.00	0.00	0.00	0.00	0.00
Σ Cations	8.09	8.10	8.11	8.09	8.11	8.10
Cl	0.80	0.71	0.74	0.77	0.75	0.80
F‡	0.15	0.14	0.14	0.21	0.10	0.10
Σ X-site	0.95	0.86	0.89	0.98	0.85	0.90
OH†	0.05	0.14	0.11	0.02	0.15	0.10

Table 7: Stoichiometry calculations from SEM-EDS data from apatites within NWA 7034(Epoxy). (A) Displays the oxide wt. % of each element analysed, along with the oxygen equivalent (-O=F and -O=Cl, previously discussed in section 2.3.3). Values of Cl and F wt. % abundances from each analysis are highlighted in blue. (B) Displays the structural formula based on 13 anions for each analysed element. The Cl, F and OH values, calculated from stoichiometry, are highlight in yellow. These values are plotted in figure 23.

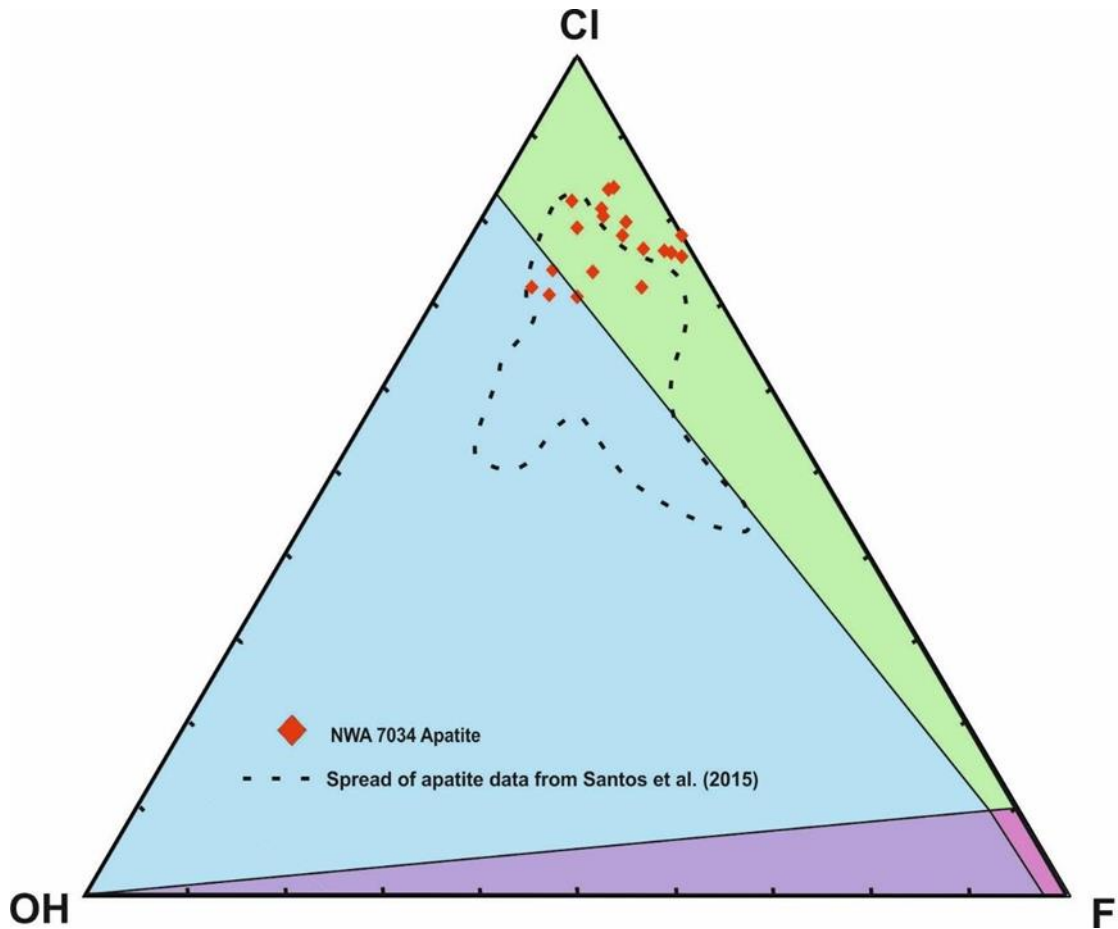


Figure 24: RVA diagram showing NWA 7034 apatite data overlain with the spread of apatite data from Santos et al. (2013). The data from this study fits relatively well with Santos et al. (2013) data. However, apatites from this study plot predominantly in the green area of the triplot (CI>OH>F), with a few minor apatites plotting in the blue area (OH>CI>F melt).

3.2 Volatile Content within Apatite in NWA 8159

NWA 8159 is a newly classified martian meteorite and therefore no previous work has been conducted on the volatile content within apatite. Apatites within this meteorite are very small (<20 μ m) and therefore quantitative analysis via the SEM-EDS is difficult.

3.2.1 Apatites in NWA 8159

Apatites were located in NWA 8159 via EDS mapping of the whole sample. Figure 25 highlights the main cluster of apatites that can be seen in the sample. The SEM was used to identify locations of interest, which are displayed in figure 26. All the selected apatites appear to be granular and anhedral with an “unclean” surface, possibly due to terrestrial contamination or alteration. Some of the apatites also have associated sulphides

(bright surrounding minerals in figure 26). The apatites appear to be locked in around large pyroxene, olivine and sulphide crystals, with minor matrix material present. EDS point analysis was then conducted on individual apatite grains to yield their major and minor element wt. % compositions.

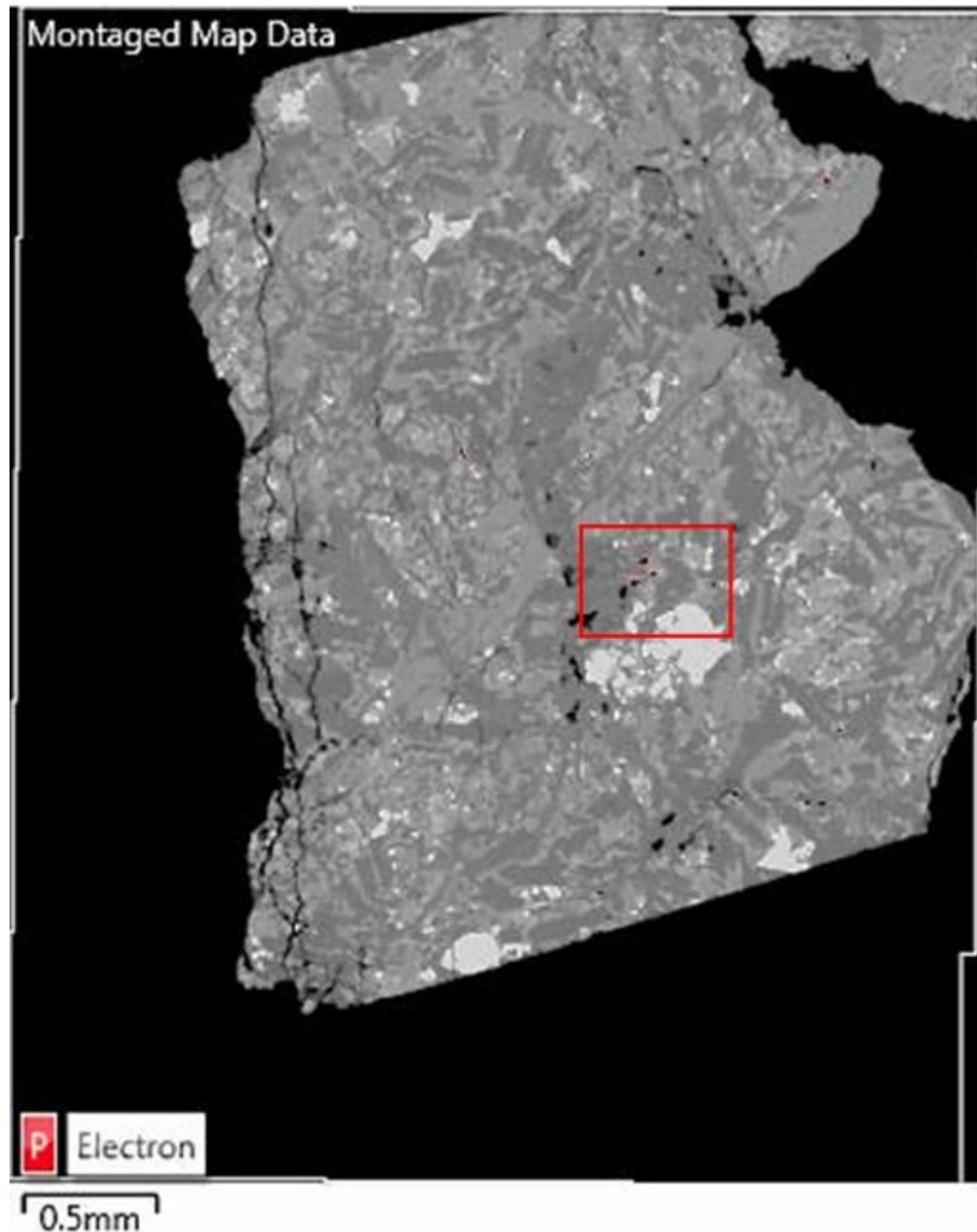


Figure 25: Energy-dispersive X-ray analysis compositional map of NWA 8159. Composition: Phosphorous: red. The red grains indicated in the EDS map are apatite. Because this meteorite contains very small apatite (<20 μ m) it is hard to detect them. The red box in the figure indicates the area containing the larger apatites within this sample.

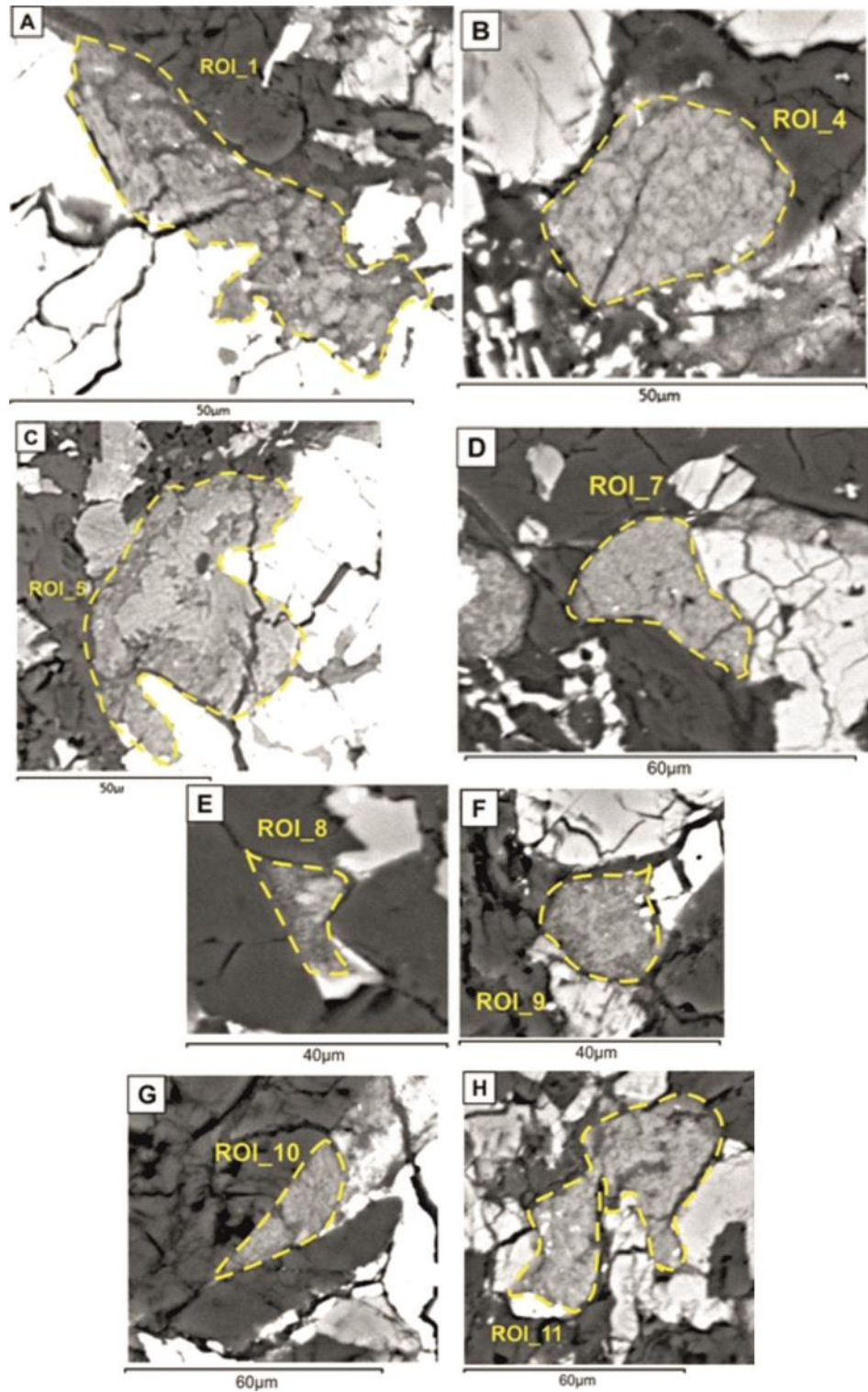


Figure 26: BSE image of apatites of interest in NWA 8159. Yellow dashes outline the grain boundary of the apatite to surrounding minerals and matrix material. Each apatite was selected as a “region of interest” (ROI). (A)-(H) Highlight the anhedral and altered appearance of apatites within NWA 8159.

3.2.2 Volatile Abundances from Triplot Data

The volatile abundance results from analysis via SEM-EDS is displayed in figure 27. As previously mentioned the data presented in the triplot (table 8) has been calculated using stoichiometry (section 2.3.3) and therefore represents a proportional ratio of the Cl: F: OH components within the apatite.

NWA 8159 apatites dominantly occupy the F-rich region of the triplot, something not typical of martian apatite. Values of F and Cl abundances are highlighted in blue in table 8. F values range from 2.79-4.83 wt. % and Cl values range from 0.03- 0.44 wt. %. Highlighted yellow in table 8 are the values that were plotted in figure 27. The calculated F values are considerably higher than Cl values, with little to no OH calculated. F enrichment at this level is predominately associated with terrestrial apatites (figure 5). The total wt. % for all apatite analysis exceeds 101% (table 8). It is important to note that high totals and F enrichment could be a result of F migration towards the beam (section 2.3.1). However, since SEM-EDS apatite analysis was conducted on NWA 7034 and yielded valid measurements, it is unlikely that F migration has largely effected the data since both NWA 7034 and NWA 8159 were analysed under the same SEM-EDS conditions.

The matrix chemistry of NWA 8159 was also analysed in ROI_5 (table 9). These analyses yielded Si values between 24.93-25.81 wt. % and P values between 0.33-0.46 wt. % and indicated that the matrix of NWA 8159 is F poor.

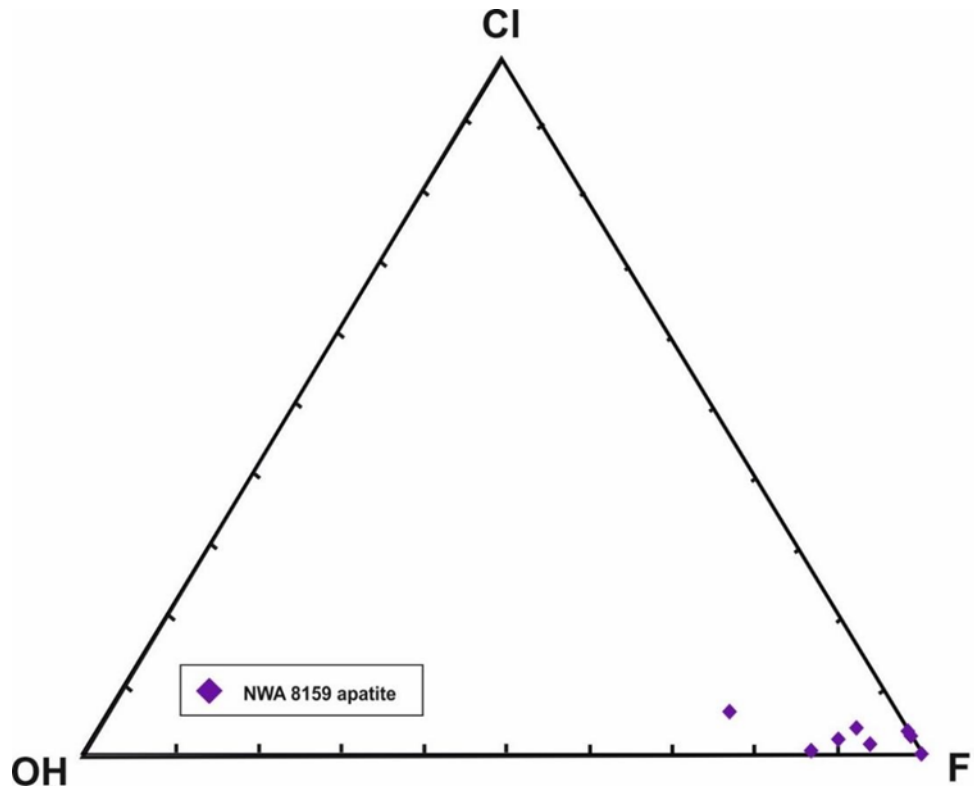


Figure 27: Plotted volatile abundances on a relative volatile abundance (RVA) diagram from apatites in NWA 8159. The values used in this plot were calculated using stoichiometry methods previously discussed in section 2.3.3 and displayed in table 8. The spreadsheet for this triplot can be viewed on the supplementary disk.

A	Oxide (wt.%)	ROI 1	ROI 4	ROI 5	ROI 7	ROI 8	ROI 9	ROI 10	ROI 11
	SiO ₂	4.41	6.50	14.72	9.30	6.38	12.61	10.62	5.81
	TiO ₂	0.05	0.09	0.08	0.07	0.07	0.08	0.06	0.04
	Al ₂ O ₃	1.78	2.33	2.55	2.96	2.83	5.76	3.95	2.23
	Cr ₂ O ₃	0.05	0.07	0.12	0.04	0.06	0.09	0.08	0.02
	FeO	2.06	2.30	1.91	3.92	0.86	2.82	1.95	4.13
	MnO	0.02	0.26	0.00	0.42	0.00	0.28	0.00	0.19
	MgO	0.87	0.71	2.67	1.19	0.23	1.05	1.08	0.50
	CaO	51.12	49.19	44.49	45.91	52.84	44.33	47.42	50.65
	Na ₂ O	0.17	0.11	0.36	0.14	0.10	0.14	0.14	0.10
	K ₂ O	0.08	0.13	0.20	0.15	0.11	0.23	0.21	0.11
	P ₂ O ₅	38.91	37.40	33.62	33.82	36.97	31.83	33.63	37.51
	S	0.43	0.36	0.93	0.42	0.21	0.49	0.41	0.22
	Cl	0.17	0.26	0.05	0.44	0.03	0.17	0.12	0.22
	F	3.87	3.23	3.46	2.79	4.83	3.47	3.61	4.33
	-O=F	1.63	1.36	1.46	1.17	2.04	1.46	1.52	1.83
	-O=Cl	0.04	0.06	0.01	0.10	0.01	0.04	0.03	0.05
	Total	105.66	104.37	106.63	102.84	107.57	104.84	104.85	107.93

B		ROI 1	ROI 4	ROI 5	ROI 7	ROI 8	ROI 9	ROI 10	ROI 11
	Si	0.36	0.53	1.16	0.78	0.51	1.02	0.86	0.47
	Ti	0.00	0.01	0.00	0.00	0.00	0.00	0.00	0.00
	Al	0.17	0.23	0.24	0.29	0.27	0.55	0.38	0.21
	Cr	0.00	0.00	0.01	0.00	0.00	0.01	0.00	0.00
	Fe	0.14	0.16	0.13	0.27	0.06	0.19	0.13	0.28
	Mn	0.00	0.02	0.00	0.03	0.00	0.02	0.00	0.01
	Mg	0.11	0.09	0.31	0.15	0.03	0.13	0.13	0.06
	Ca	4.49	4.34	3.76	4.12	4.55	3.85	4.14	4.39
	Na	0.03	0.02	0.06	0.02	0.02	0.02	0.02	0.02
	K	0.01	0.01	0.02	0.02	0.01	0.02	0.02	0.01
	P	2.70	2.61	2.25	2.40	2.52	2.18	2.32	2.57
	S	0.00	0.00	0.00	0.00	0.00	0.00	0.00	0.00
	∑ Cations	8.01	8.01	7.94	8.09	7.97	7.99	8.01	8.02
	Cl	0.02	0.04	0.01	0.06	0.00	0.02	0.02	0.03
	F‡	1.00	0.84	0.86	0.74	1.23	0.89	0.93	1.11
	∑ X-site	1.03	0.88	0.87	0.80	1.23	0.91	0.95	1.14
	OH†	0.00	0.12	0.13	0.20	0.00	0.09	0.05	0.00

Table 8: Stoichiometry calculations from SEM-EDS data from apatites within NWA 8159. (A) Displays the oxide wt. % of each element analysed, along with the oxygen equivalent (-O=F and -O=Cl, previously discussed in section 2.3.3). Values of Cl and F wt. % abundances from each analysis are highlighted in blue. (B) Displays the structural formula based on 13 anions for each analysed element. The Cl, F and OH values, calculated from stoichiometry, are highlight in yellow. These values are plotted in figure 27.

Weight %	ROI_5 Spec 2	ROI_5 Spec 3
Si	24.94	25.81
Ti	0	0.03
Al	0.51	0.54
Cr	0	0
Fe	27.16	22.59
Mn	1.34	0.93
Mg	8.11	10.69
Ca	0.70	0.61
Na	0.21	0.22
K	0.03	0.03
P	0.33	0.46
S	0.09	0.04
O	43.28	44.66
Cl	0.04	0.34
F	0	0
Total wt.%	106.75	106.95

Table 9: Elemental abundances of NWA 8159 matrix material in ROI_5 from SEM-EDS analysis. Spectrum (Spec) 2 and 3 where two separate spot analyses on the matrix. No F was measured in the these analyses indicating a F-poor matrix.

Chapter 4 Hydrogen Isotope Data

4.1 Deuterium/Hydrogen Ratios from NWA 8159

Unfortunately collection of hydrogen isotope data within this study was not possible from apatites within NWA 8159 as they are $<20\mu\text{m}$ and therefore too small for analysis using the ion microprobe technique. Analyses of hydrogen isotopes using the Nano SIMS technique may be possible, but again the size of these apatites make it difficult to collect accurate and valid results from them.

4.2 NWA 7034 Targets for Hydrogen Isotope Analysis

Apatites were selected for hydrogen isotope analysis if they were $>25\mu\text{m}$ to try to ensure that matrix material would not be incorporated into the data. The least fractured and most pristine (i.e. no inclusions) apatites were prioritised. However, since this is a meteorite that has experienced impact/ejection forces and secondary alteration on the martian surface it was difficult to find “perfect” apatites. Unfortunately, not all of the pre-selected apatites were analysed using the SIMS as some were too close to the edge of the sample and many contained too many fractures for an accurate measurement to be taken. Therefore, eight apatites in total were analysed, four from NWA 7034 (In) (ROI_1,2,4,8) and four from NWA 7034 (Epoxy) (ROI_3, 5, 7,8a). The targeted apatites come from different regions within the both samples (indicated by the red boxes present in figure 28 and 29), with area 1 apatites: ROI_1, 2 and 4, area 2 apatite: ROI_8, area 3 apatites: ROI_7 and 8a, area 4 apatite: ROI_3 and area 5 apatite: ROI_5. A lithological mix (i.e. matrix and clast) of apatites was attempted, but only three of the apatites analysed (ROI_1,2 and 8a) were contained in a clast due to size constraints. All apatites selected for analysis are displayed previously in figures 18A, 18B, 18C, 19I, 19K, 20M and 20N.

Anhydrous minerals were analysed to determine if degassing from the samples surfaces or terrestrial contamination was a significant component within the data. Two pyroxenes were analysed for D/H from both samples of NWA 7034.

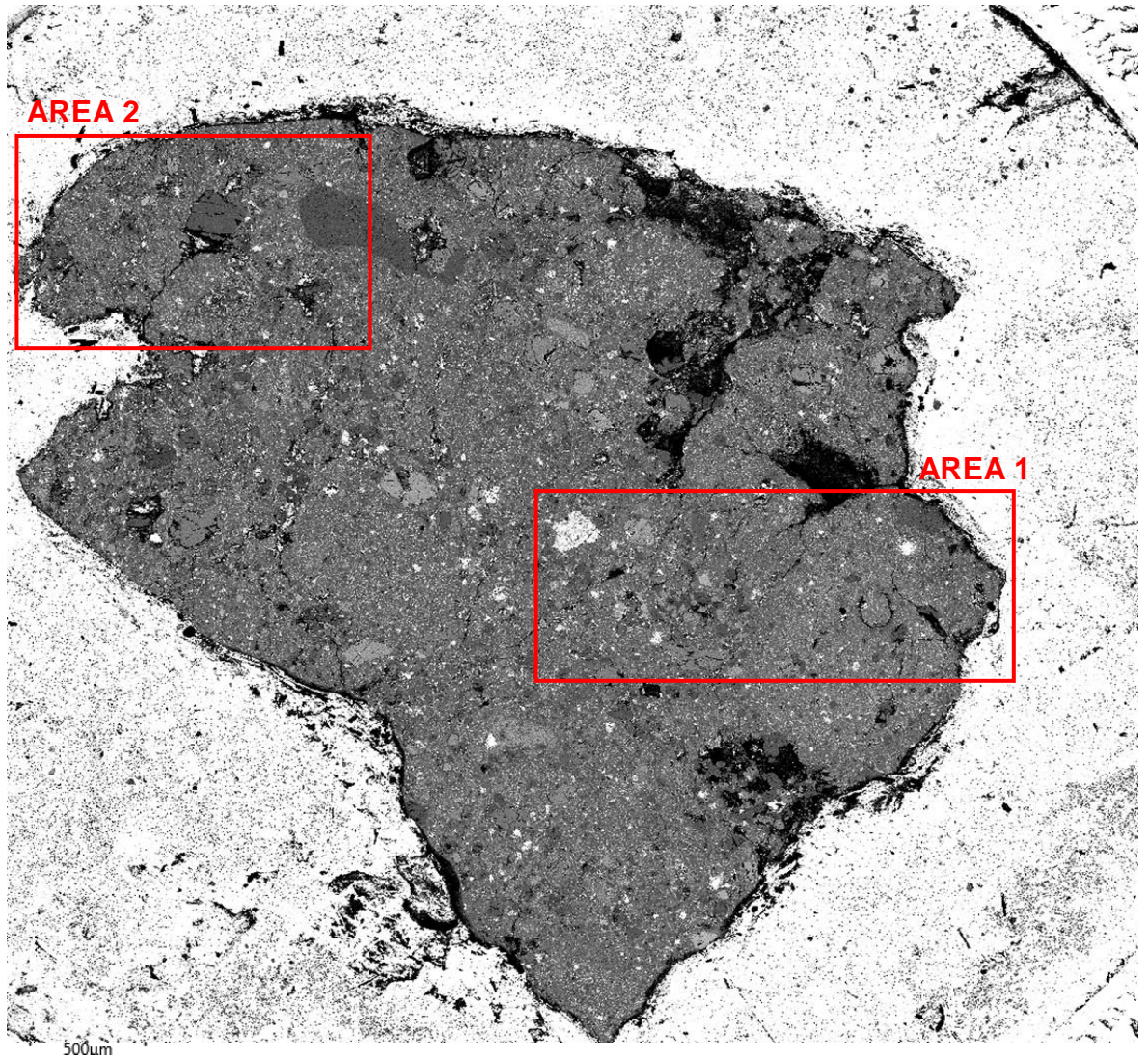


Figure 28: BSE image of NWA 7034 (Indium mounted sample) taken by the SEM @ ISAAC Facility, University of Glasgow. The red boxes indicated the regions containing the targeted apatites for hydrogen isotope analysis at the University of Hawaii.

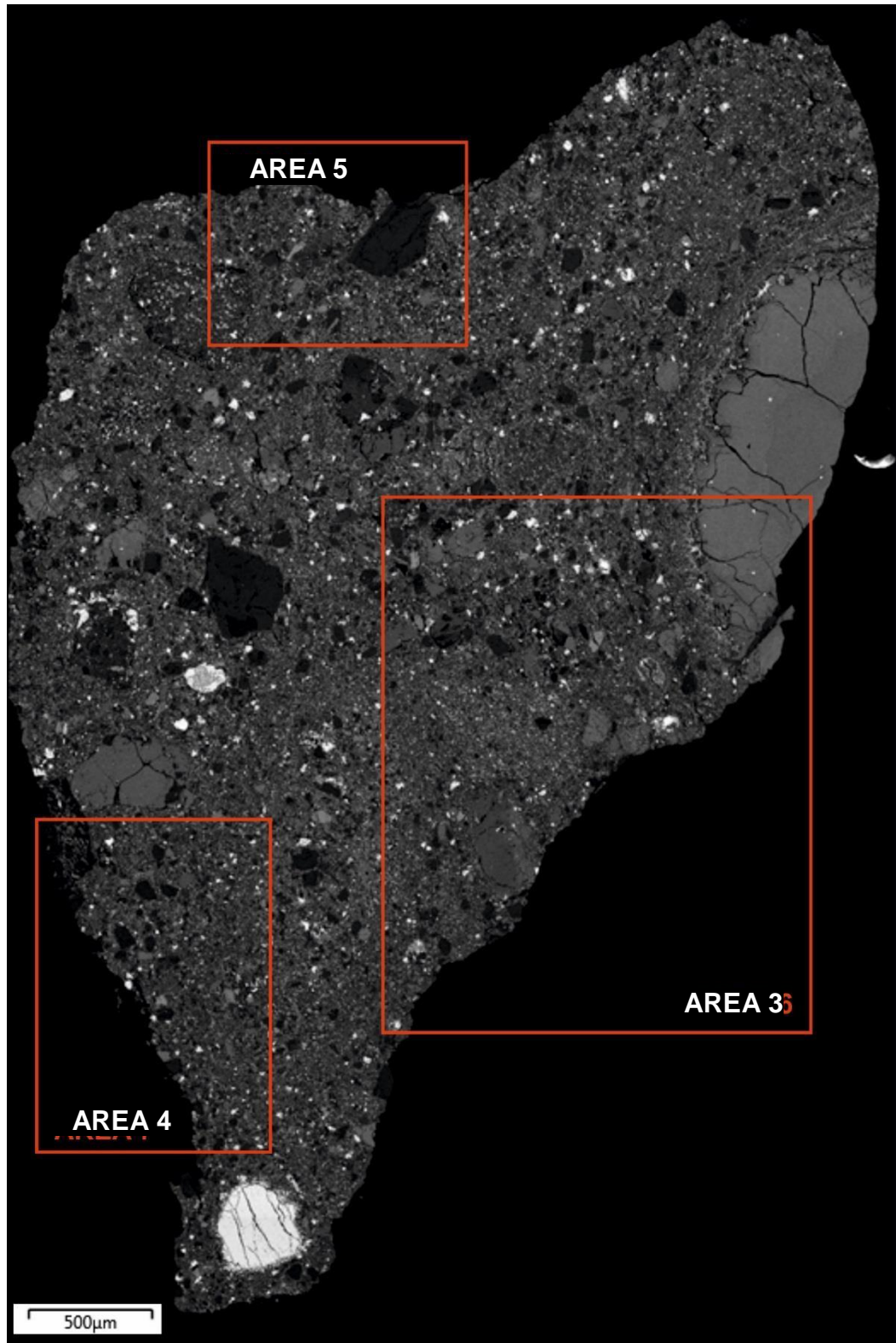


Figure 29: BSE image of NWA 7034 (epoxy mounted sample) taken by the SEM @ ISAAC Facility, University of Glasgow. The red boxes indicated the regions containing the targeted apatites for hydrogen isotope analysis at the University of Hawaii.

4.2.1 Pit Images from Targeted Apatites

To ensure that hydrogen isotope analysis was successful in measuring the targeted apatites, SEM imaging of the apatites was conducted to collect pit images from each analysed apatite. Figure 30 shows the pit produced in ROI_1. The pit indicates that the apatite was targeted successfully. Figures 31, 32 and 33 highlight the pits produced in ROI_2, ROI_4 and ROI_8. These pits were successful and did not include matrix in the analysis. Figure 34 displays the pit produced in ROI_3. The apatite was successfully targeted however, a hole can be observed in the bottom of the pit, indicating that matrix material may have been incorporated at the end of the analysis as the beam penetrated further into the apatite. Figure 35 indicates the pit produced in ROI_5. Two pits can be seen in this figure 35 as it was discovered during analysis that the matrix (pit 5a) had been targeted instead of the apatite and therefore a second pit was made (pit 5b). Figure 36 shows the pit produced in ROI_7. The selected apatite was targeted however; it is possible that some of the matrix was incorporated into this analysis as the pit edge on the right hand side is slightly off the apatite. Figure 37 highlights the pit produced in ROI_8a. This pit did not include matrix into the analysis.

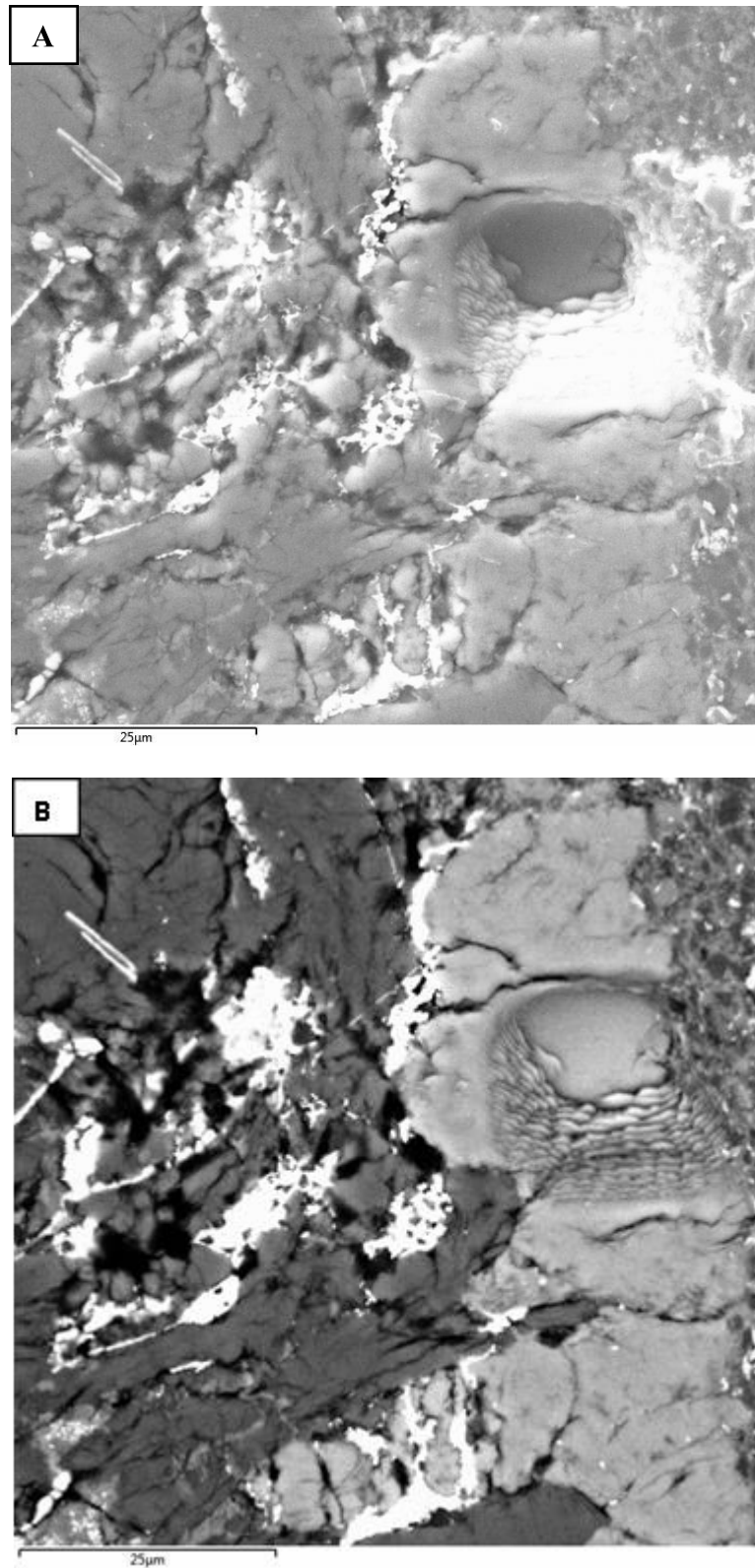


Figure 30: A Secondary Electron image (A) and a BSE image (B) of pit produced in apatite ROI_1 NWA 7034 (In). The edge of the pit may have incorporated matrix material into the analysis.

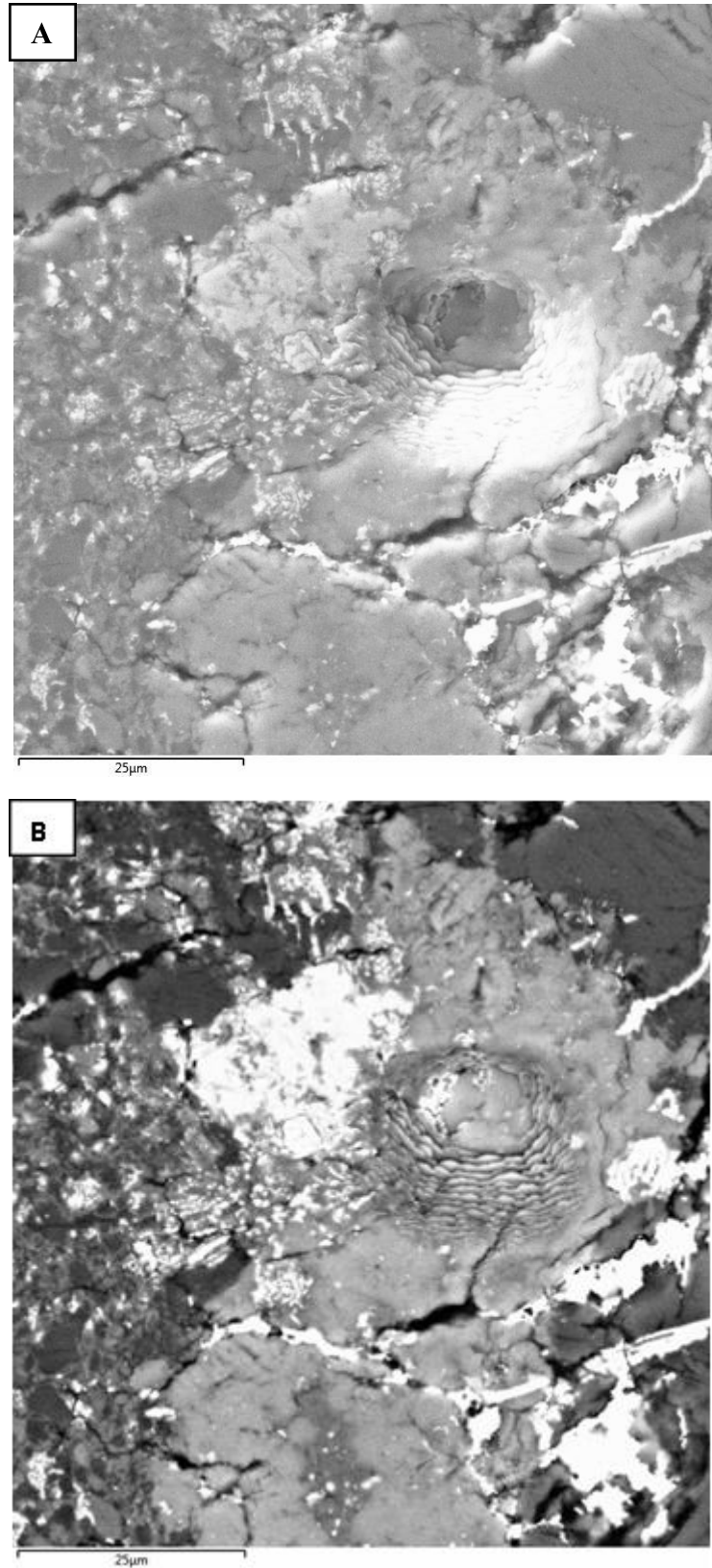


Figure 31: A Secondary Electron image (A) and a BSE image (B) of the pit produced in apatite ROI_2 NWA 7034 (In).

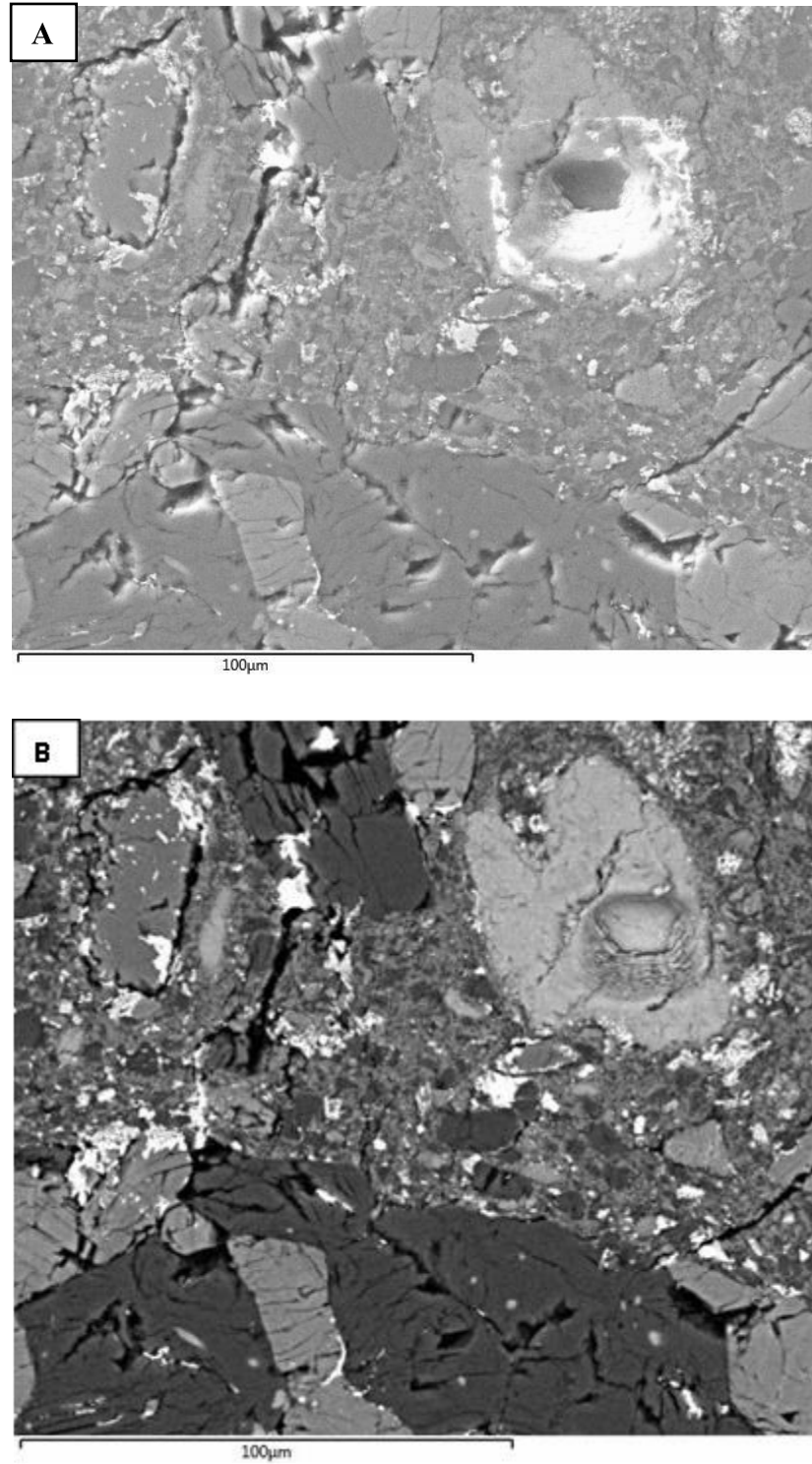


Figure 32: A Secondary Electron image (A) and a BSE image (B) of the pit produced in apatite ROI_4 NWA 7034 (In).

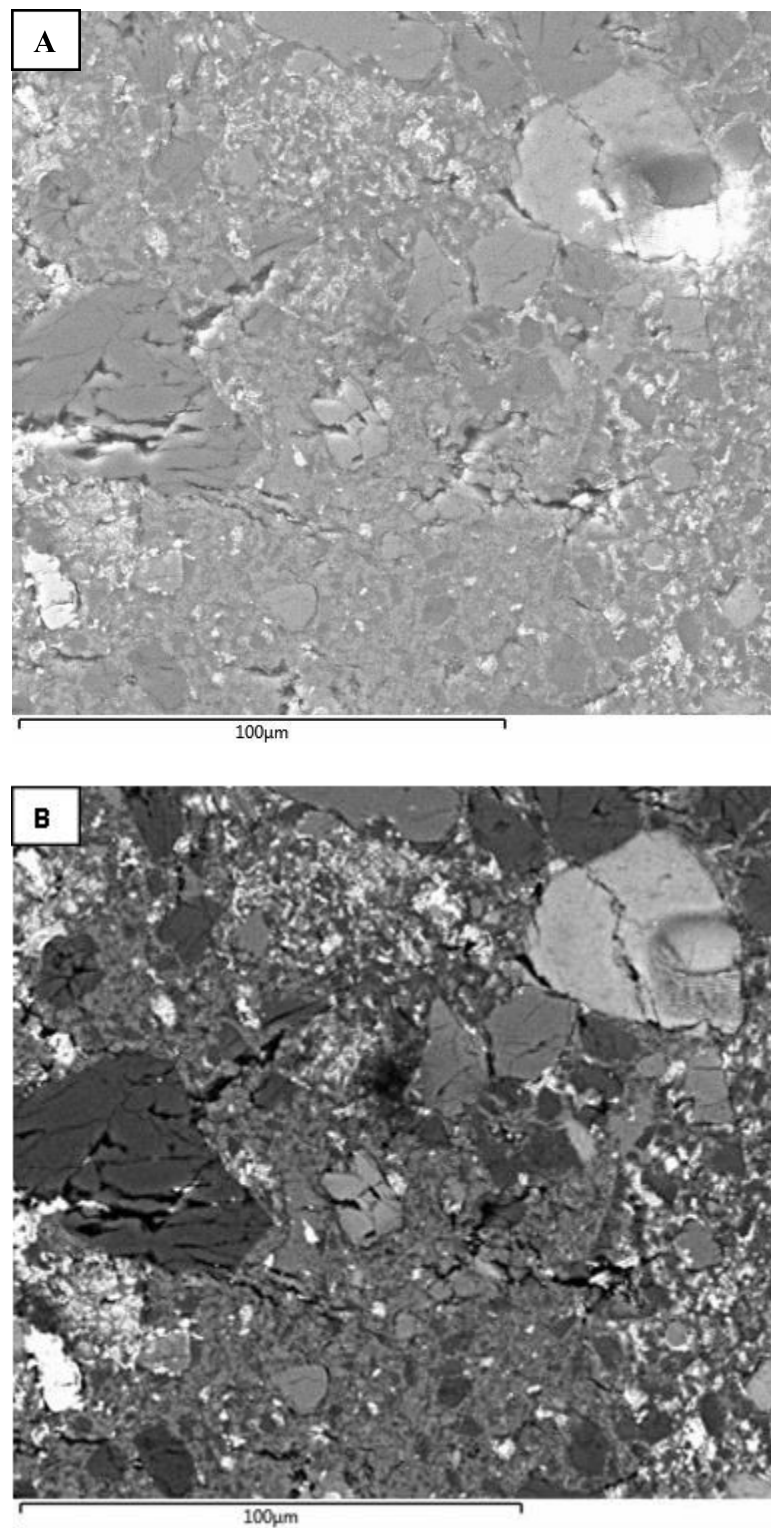


Figure 33: A Secondary Electron image (A) and a BSE image (B) of the pit produced in apatite ROI_8 NWA 7034 (In).

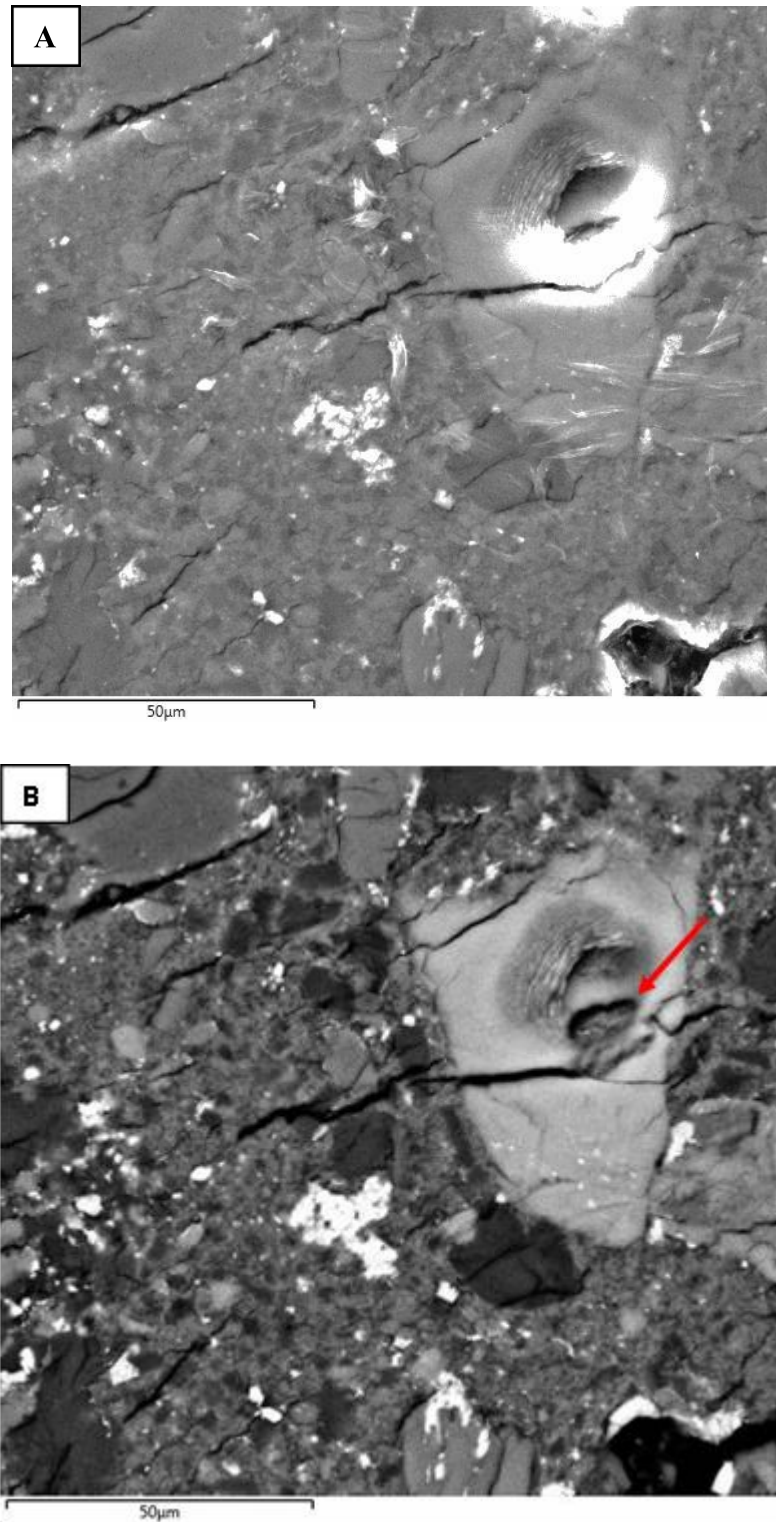


Figure 34: A Secondary Electron image (A) and a BSE image (B) of the pit produced in apatite ROI_3 NWA 7034 (Epoxy). A hole can be observed in the bottom of the pit (indicated by the red arrow), indicating that matrix material may have been incorporated at the end of the analysis as the beam penetrated further into the apatite.

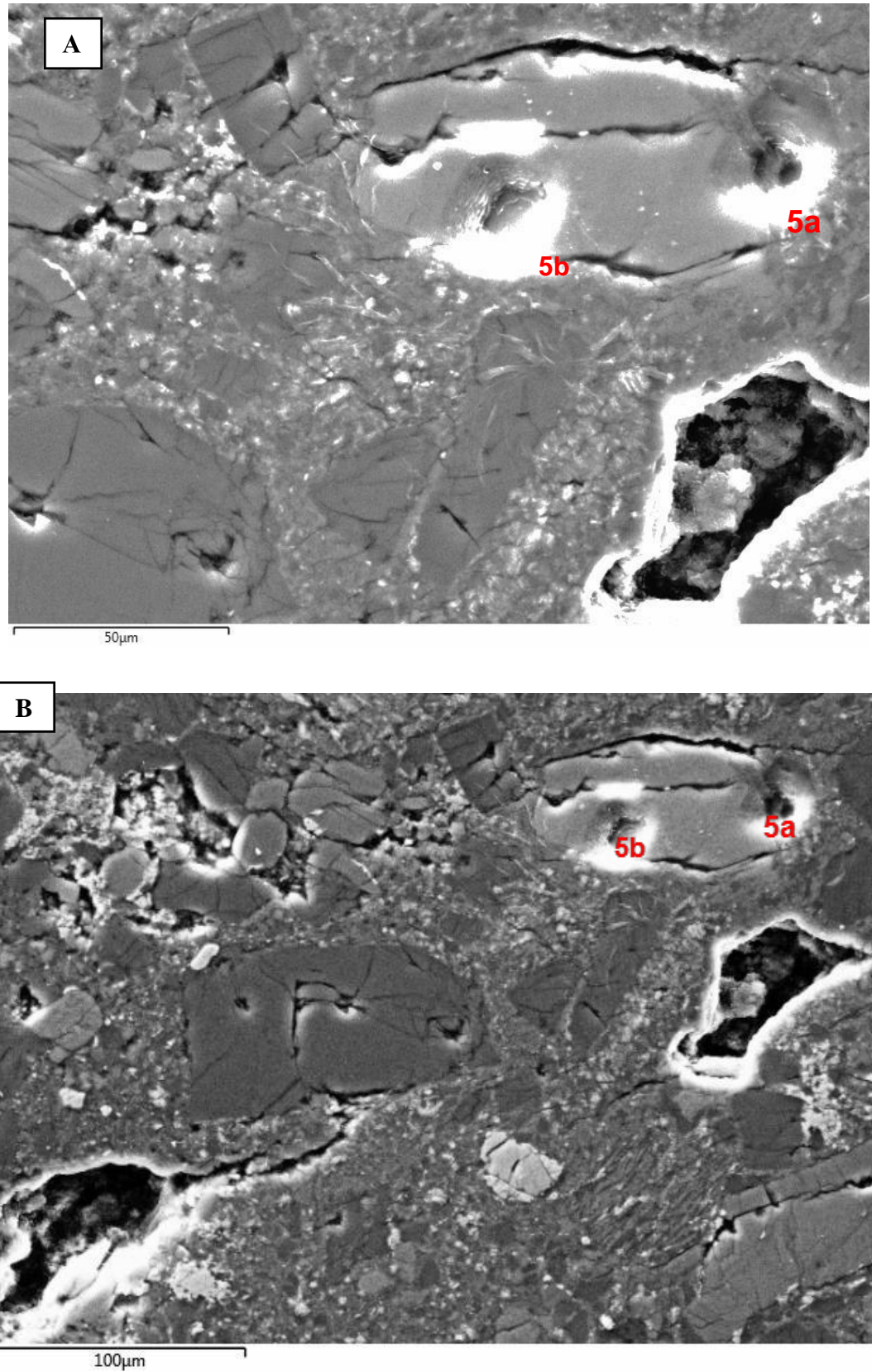


Figure 35: A Secondary Electron image (A) and a BSE image (B) of the pits produced in apatite ROI_5 NWA 7034 (Epoxy). Two pits can be seen in this figure as during analysis it was discovered that the matrix (pit 5a) had been targeted instead of the apatite and therefore a second pit was made (pit 5b).

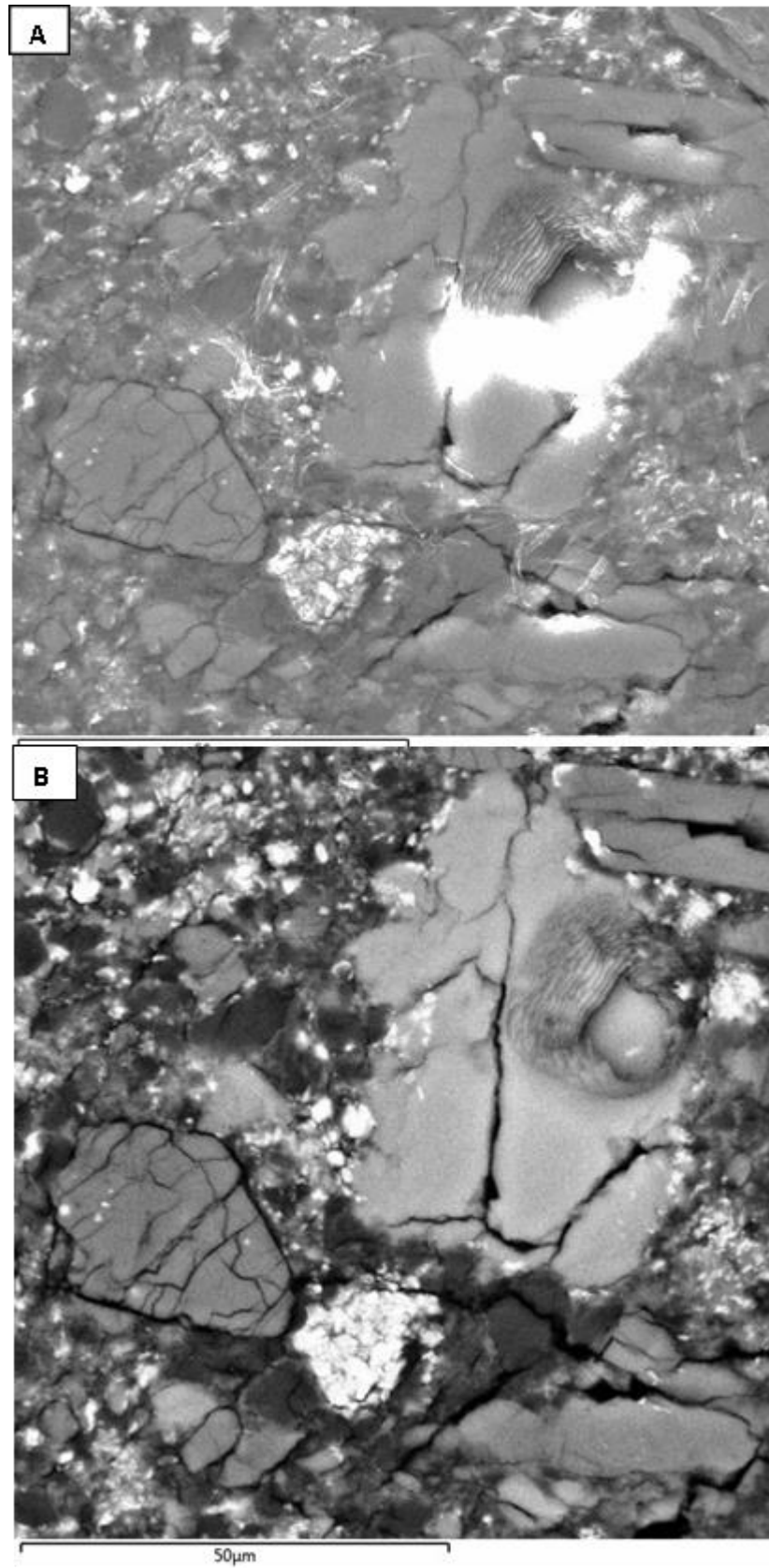


Figure 36: A Secondary Electron image (A) and a BSE image (B) of the pit produced in apatite ROI_7 NWA 7034 (Epoxy).

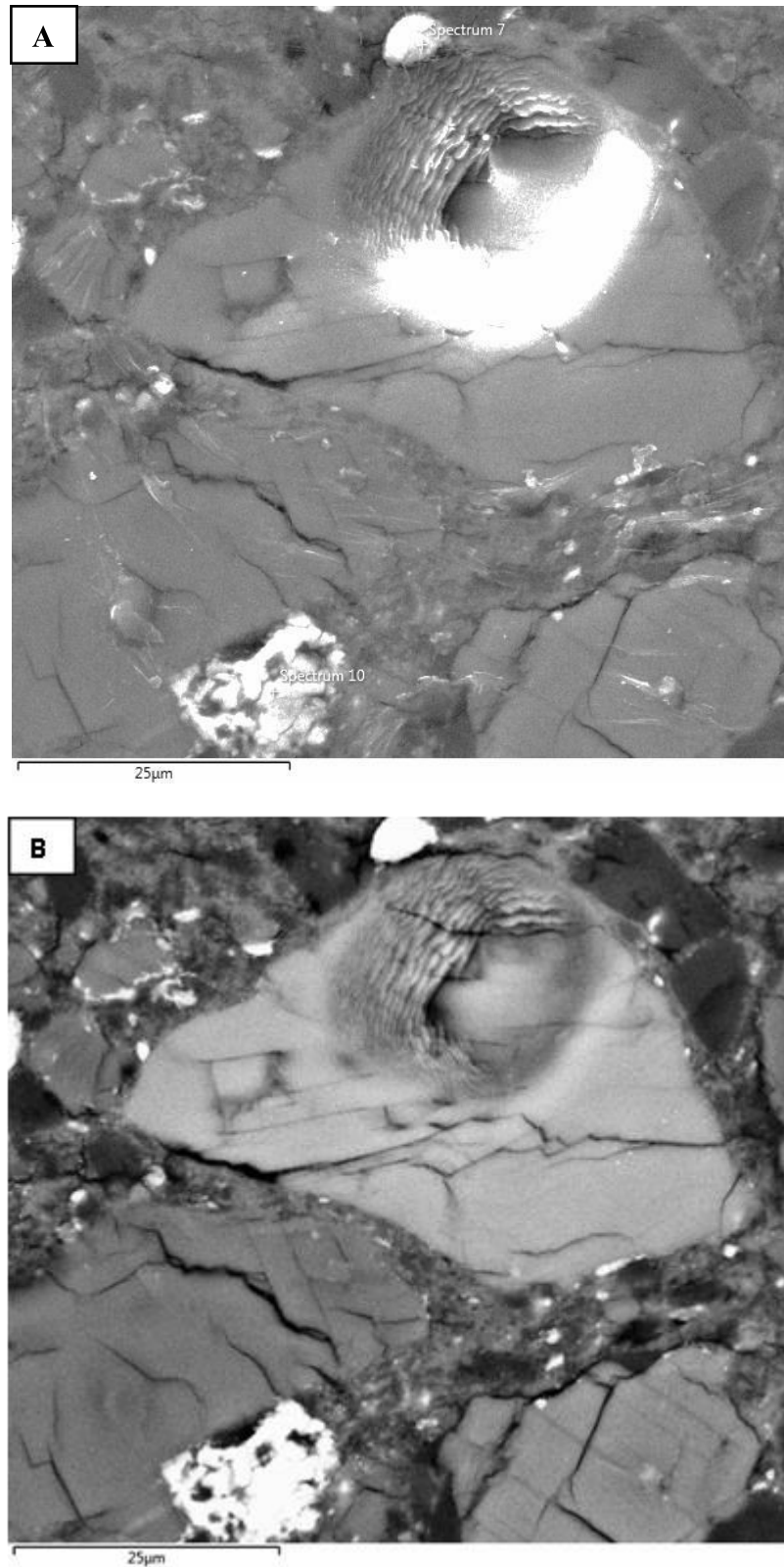


Figure 37: A Secondary Electron image (A) and a BSE image (B) of a pit produced in apatite ROI_8a NWA 7034 (Epoxy).

4.2.2 Pit Images from Anhydrous Minerals

To ensure that hydrogen isotope analysis was successful in measuring the targeted pyroxenes, SEM imaging of the pyroxenes was conducted to collect pit images. Two pyroxenes were selected for hydrogen analysis, one from both samples of NWA 7034. After data collection, SEM imaging was conducted to ensure the beam had made a clean pit in the pyroxene and therefore an accurate analysis was acquired. Figure 38 displays the pit produced in the pyroxene from NWA 7034 (In). This analyses hit the target and did not incorporate any matrix material into the analysis. Figure 39 indicates the pit produced in the pyroxene from NWA 7034 (Epoxy). On the right hand side of the pit it appears that the beam may have penetrated into the matrix. The loose fragment that can be viewed in the pit was not present during hydrogen isotope analysis. The sample underwent re-polishing after hydrogen isotope analysis was conducted and this is likely to be a piece of debris from the sample that fell into the pit during polishing.

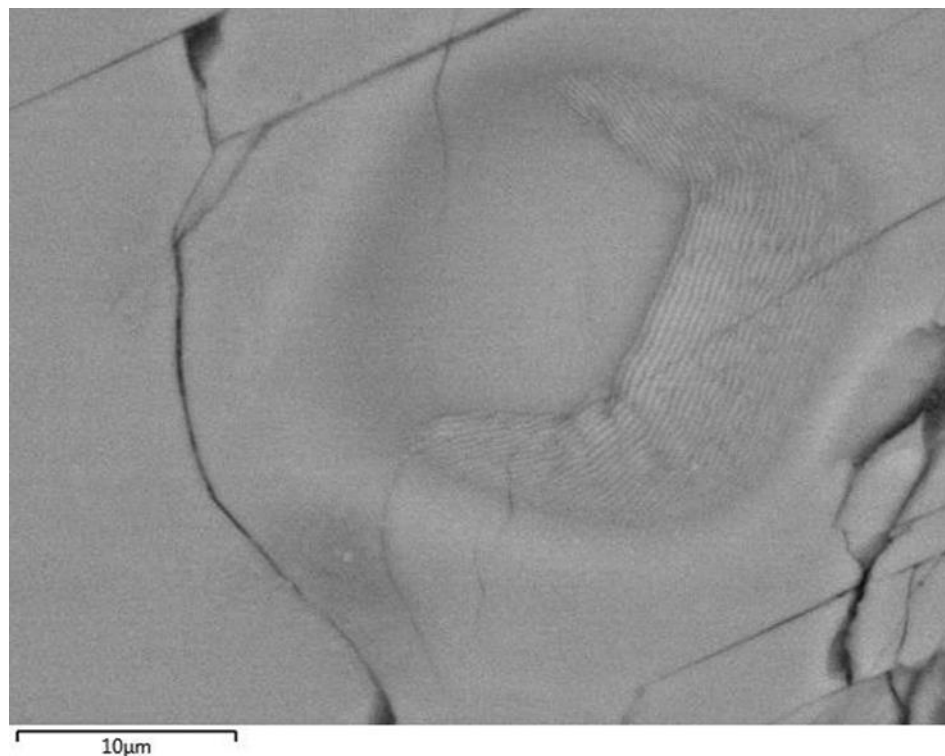


Figure 38: BSE image of the pyroxene pit from NWA 7034 (In).

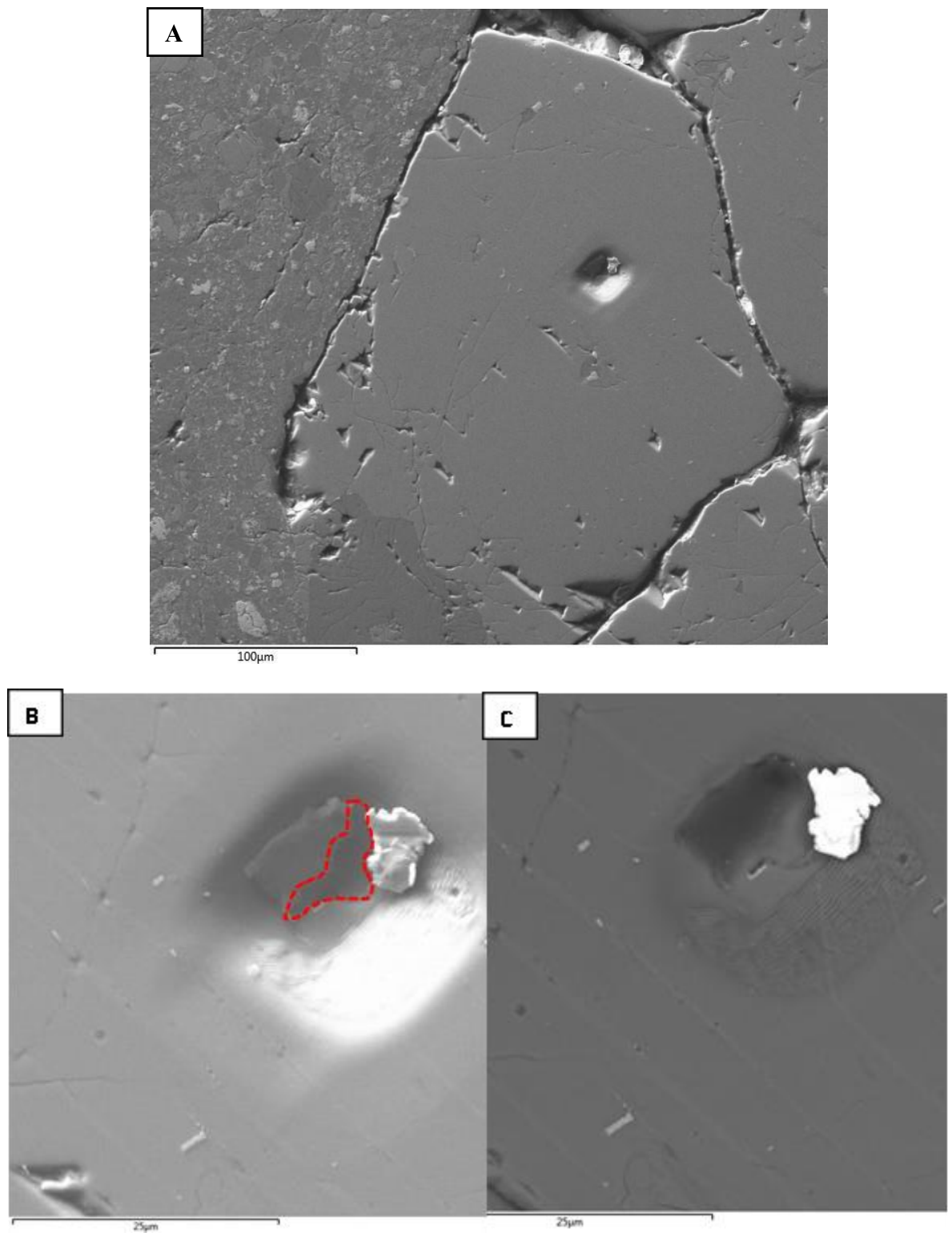


Figure 39: A Secondary Electron image (A and B) and a BSE image (C) of the pyroxene pit from NWA 7034 (Epoxy). The loose fragment on the right of the pit is a result of re-polishing after hydrogen isotope analysis. On the right hand side of the pit it appears that the beam may have penetrated the matrix (indicated by red dashed line).

4.3 NWA 7034 Hydrogen Isotope Results

There are possibly three distinct hydrogen reservoirs on Mars (atmosphere, intermediate and mantle reservoirs) which all exhibit characteristic δD values. The martian atmosphere displays high δD values between 2500‰-6000‰ (Webster et al., 2013; Usui et al., 2015). The martian mantle displays low δD values <275 ‰ (Usui et al., 2012) and the proposed intermediate reservoir has δD values 1000‰-2000‰ (Usui et al., 2015) The data collected in this study from NWA 7034 exhibits δD values between 52 ± 82 ‰ to 782 ± 83 ‰ (table 11) and are therefore are not a martian atmospheric values or values representing the intermediate reservoir. However, it is possible that the data in this study contains low δD values that are representative of the martian mantle (table 12); however, this will be fully discussed in Chapter 5.

4.3.1 Measured OH Component for Volatile Abundance Triplot

Hydrogen isotope analysis allowed for direct measurement of the OH component within selected apatites, and confirmed that apatites within NWA 7034 do contain water. This OH component could then be matched with the specific apatite Cl and F weight % to produce a relative volatile abundance triplot (blue in figure 40). NWA 7034 apatites were previously seen to occupy the Cl-rich region of the triplot based on stoichiometry (red in figure 40). A direct comparison cannot be made between these data sets as red diamonds represent proportional Cl: F: OH components via stoichiometry whereas blue diamonds represent the wt. % of Cl, F and OH (table 10). Despite this, the fact that they plot in similar regions in the triplot confirms that Cl-rich apatites are present in NWA 7034, with some more Cl-rich (ROI_2, 3, 5, 7, 8a), and some more Cl-poor (ROI_1 and 4). Despite hydrogen isotope analysis conducted on ROI_8 (NWA 7034(In)), it could not be represented in the triplot below due to wt. % totals < 96 %.

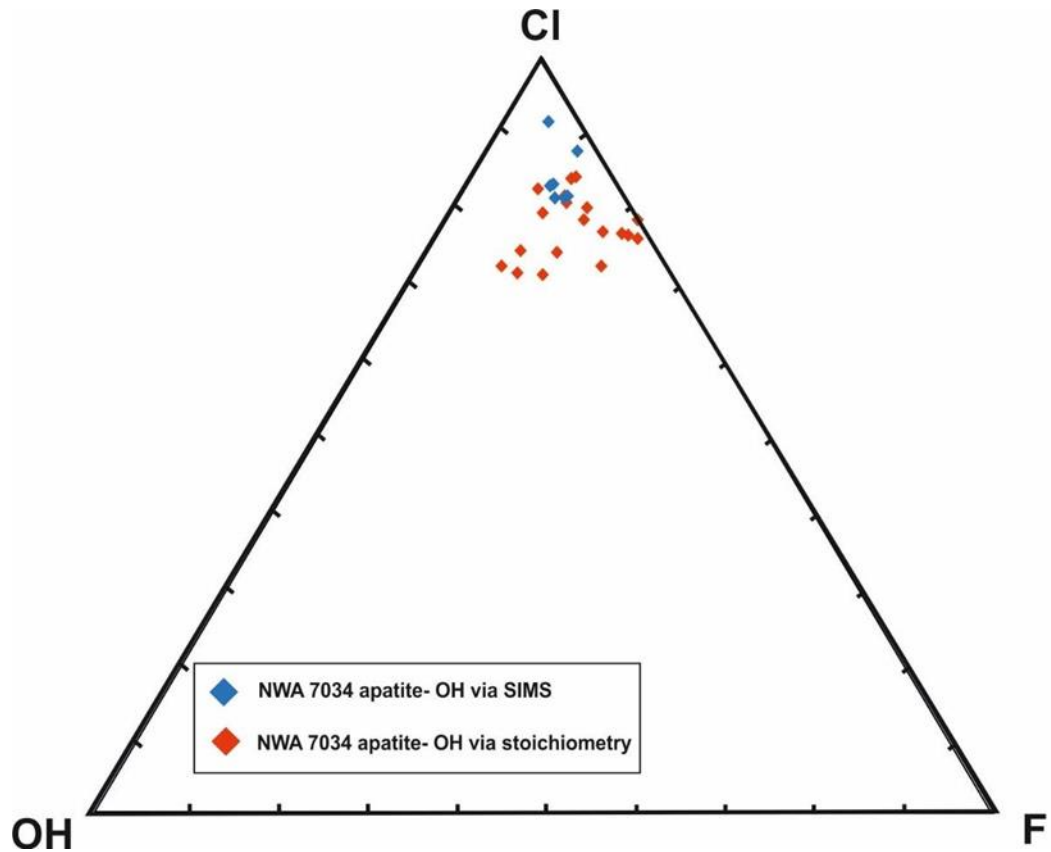


Figure 40: Plotted volatile abundances on a relative volatile abundance (RVA) diagram from apatites in NWA 7034. Blue diamonds represent apatites which OH components were measured by SIMS analysis. Red diamonds (previously shown in figure 21) represent apatites where the OH component was calculated using stoichiometry methods previously discussed in section 2.3.3.

Apatite	Cl (wt.%)	H ₂ O wt. %	F (wt.%)
ROI_1	4.75	0.44	0.53
ROI_2	5.18	0.51	0.68
ROI_3	5.05	0.43	0.73
ROI_4	4.67	0.18	0.25
ROI_5	5.38	0.47	0.62
ROI_7	5.11	0.41	0.75
ROI_8a	5.21	0.14	0.60

Table 10: The wt. % abundances of Cl, F and H₂O for each analysed apatite in NWA 7034. The wt. % values for Cl and F were measured using SEM-EDS analysis. The H₂O wt. % values were directly measured using the SIMS at UH. These values are plotted as blue diamonds in figure 40 above.

4.3.2 Cameca ims 1280 Hydrogen Isotope Analyses

Apatite grains in NWA 7034 show δD values between 51.72‰ and 782.47‰ and water content values between 1379.85 ± 30 ppm and 5097.68 ± 100 ppm (table 11). Hydrogen isotope analysis was conducted on two pyroxene grains in NWA 7034. One from NWA 7034(In) and the other NWA 7034 (Epoxy). The pyroxene grain from NWA 7034 (In) displays a δD value of -136.14 ± 88 ‰ and water content of 465.62 ± 30 ppm whereas the pyroxene grain from NWA 7034 (Epoxy) displays a δD value of -98.02 ± 88 ‰ and water content of 190.20 ± 10 ppm. It is unusual that a pyroxene mounted in In displays a much higher δD and water content than a pyroxene mounted in epoxy as you would expect the epoxy sample to have degassed and likely increased the values. However, as NWA 7034 is a polymict breccia it may be expected that different pyroxene grains have different water contents- especially because NWA 7034 contains evidence of aqueous alteration in certain clasts (McCubbin et al., 2016).

Sample	δD (‰)	2σ	H ₂ O(wt. %)	2σ	H ₂ O(ppm)
Standards					
Crystal Lode 1 ap005	-72.99	3.65	0.370	0.03	3703.91
Crystal Lode 2 ap005	-72.99	3.65	0.370	0.03	3703.91
Crystal Lode 3 ap005	-72.99	3.65	0.370	0.03	3703.91
Crystal Lode 4 ap005	-72.99	3.65	0.370	0.03	3703.91
Russia 1 ap018	-89.60	14.41	0.204	0.04	2041.41
Russia 2 ap018	-89.60	14.41	0.204	0.04	2041.41
San Carlos Olivine	N/A	N/A	0.001	0.04	1.10
NWA 7034 (In)					
ROI 1	512.50	82.49	0.436	0.09	4358.89
ROI 2	264.04	82.18	0.510	0.10	5097.68
ROI 4	782.47	83.09	0.182	0.04	1824.28
ROI_8	631.48	85.27	0.171	0.03	1718.29
NWA 7034 (Epoxy)					
ROI 3	51.72	81.96	0.431	0.08	4307.96
ROI 5	52.10	81.89	0.468	0.09	4677.33
ROI 7	390.85	82.12	0.408	0.08	4083.15
ROI_8a	556.89	83.61	0.138	0.03	1379.85
Anhydrous Minerals					
Pyroxene (In)	-136.14	87.95	0.05	0.03	465.62
Pyroxene (Epoxy)	-98.02	88.46	0.02	0.01	190.20

Table 11: Hydrogen isotope data from all analysed standards, apatites and anhydrous minerals. δD is represented in ‰. H₂O is represented in both wt. % and ppm(‰). The 2σ uncertainties for δD and H₂O values are also displayed. All numbers have been rounded to 2 decimal places, with the exception of the H₂O wt. % column which has been rounded to 3 decimal places. The calculations involved in this table can be viewed in the supplementary disk provided.

Three distinct groupings of apatites can be inferred through δD , water content and texture of apatite (table 12). Group 1 consists of ROI_4, 8 and 8a, highlighted green in table 12. This group is characterised by high δD values ($782.47 \pm 83\%$, $631.48 \pm 85\%$ and $556.89 \pm 84\%$ respectively) paired with low water contents (1842.28 ± 40 ppm, 1718.29 ± 30 ppm and 1379.85 ± 30 ppm respectively). Group 2 consists of ROI_1, 2 and 7 (highlighted blue in table 12), with intermediate δD values ($512.50 \pm 82\%$, $264.04 \pm 82\%$ and $390.8582 \pm \%$ respectively) and high water contents (4358.89 ± 90 ppm, 5097.68 ± 100 ppm and 4083.15 ± 80 ppm respectively). It should be noted here that there appears to be a correlation with spongy texture and high water content. Group 3 consists of ROI_3 and 5, highlighted in orange in table 11. Group 3 is characterised by low δD values ($51.72 \pm 82\%$ and $52.10 \pm 82\%$) and high water contents similar to Group 2 (4307.96 ± 80 ppm and 4677.33 ± 90 ppm).

These groupings are even more prominent when the δD versus the water content is plotted (figure 41). The apatites in NWA 7034 show a slight trend of increasing δD with decreasing water content (previously discovered for SNCs and ALH 84001 by Hallis et al., 2016).

APATITE	δD (‰)	H ₂ O (ppm)	TEXTURE	PIT NOTES
ROI_1	512.50	4358.89	Spongey	Hit apatite
ROI 2	264.04	5097.68	Spongey	Hit apatite
ROI 4	782.47	1824.28	Anhedral	Hit apatite
ROI 8	631.48	1718.29	Euhedral	Hit apatite
ROI 3	51.72	4307.96	Euhedral	Hole in the bottom of the pit into matrix
ROI 5	52.10	4677.33	Euhedral	Hit apatite
ROI 7	390.85	4083.15	Anhedral	Edge of pit may have incorporated matrix
ROI 8a	556.89	1379.85	Euhedral	Hit apatite

Table 12: Groupings of apatite within NWA 7034 based on δD , water content (H₂O) and texture. Group 1 is highlighted in green, Group 2 is highlighted in blue and Group 3 is highlighted in orange. For uncertainty values refer to table 11.

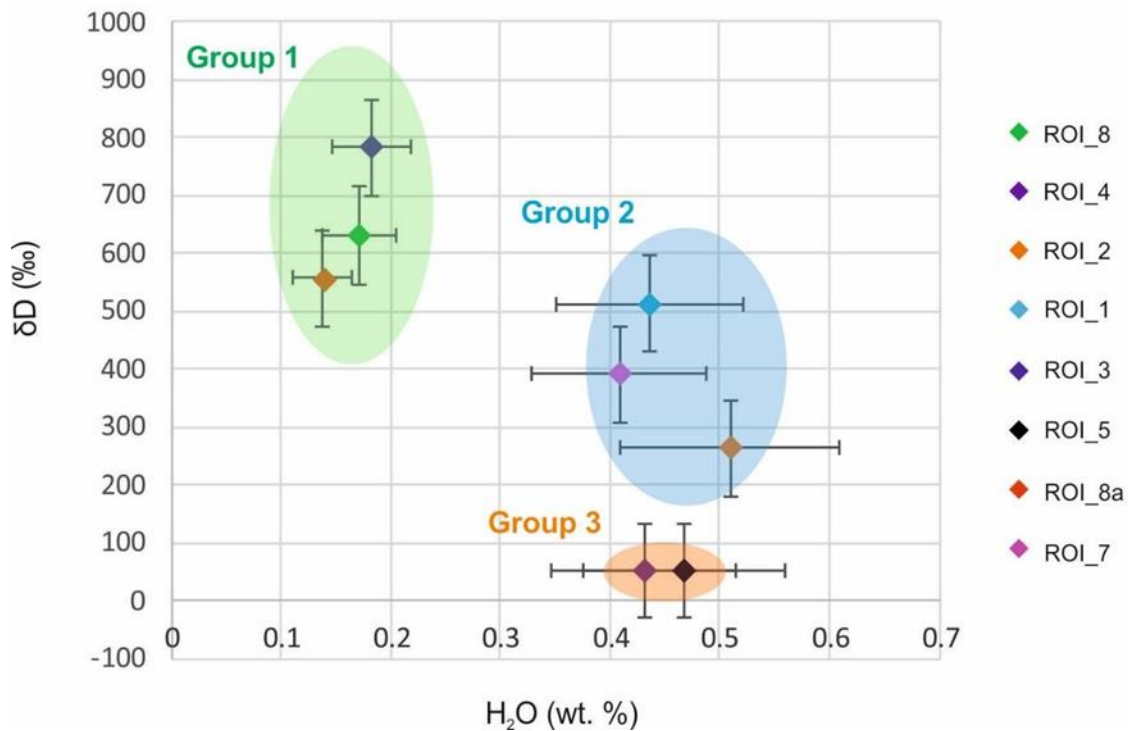


Figure 41: Groupings of apatite based on δD versus water content (H₂O wt.%). Group 1 (ROI_4,8 and 8a) is contained within the green region, Group 2 (ROI_1, 2 and 7) in the blue region and Group 3 (ROI_3 and 5) in the orange region. These colours relate to the information from table 12. 2 σ uncertainties are shown as error bars in the graph above, these errors can be viewed in table 11 and in the supplementary disk provided.

Chapter 5 Discussion

5.1 Volatile Abundances in NWA 7034

Apatites from NWA 7034 are Cl-rich, which is consistent with the martian geochemical model of Cl enrichment (Filiberto and Treiman, 2009; McCubbin and Jones, 2015) and with previous studies on martian apatite (Greenwood, 2005; Patino Douce and Roden, 2006; McCubbin and Nekvasil, 2008; Filiberto and Trieman, 2009; Patino Douce et al., 2011; Santos et al., 2013; McCubbin et al., 2013; McCubbin and Jones, 2015). The volatile content of NWA 7034 is in fact uncharacteristically uniform for a polymict breccia (i.e., no groupings of apatite can be seen in terms of their volatile abundances (Cl: F: OH)), indicating post-crystallisation processes- possibly a thermal event (McCubbin et al., 2016)- have overprinted the original Cl, F and OH contents of these apatites. However, this could also be the result of the uncertainties on measurements from SEM analysis compared to uncertainties from SIMS analysis. The uncertainty on each SEM-EDS analysis is 0.1 wt. % (i.e., 1000ppm), therefore it is possible that the SEM is not precise enough to detect small differences in apatite volatile abundances.

The most obvious component, which separates the volatile abundance of NWA 7034 apatites, is their varying OH content. When the data from this study were compared to the data of Santos et al. (2013) it was noted that apatites from this study predominately plotted in the Cl dominated melt region, with a few apatites plotting in the OH dominated melt region. Because of the spread of apatite across these two regions of the triplot, it is possible that there are two distinct groups of apatite that formed from different melts (i.e., a Cl>OH>F melt and a OH>Cl>F melt) or that all the apatites came from the same melt in which the dominant volatile of the melt varied (Santos et al., 2013).

The OH component of apatites from NWA 7034 was further investigated by in-situ measurement using an ion microprobe. A direct comparison between stoichiometrically calculated OH and SIMS measured OH cannot be made as the former is based on proportions (the number of anions) whereas the latter is based on wt. %. However, Cl-rich apatites, with a confirmed water content was provided from both stoichiometry and SIMS.

5.2 Volatile Abundances in NWA 8159

Apatites from NWA 8159 are F-rich, unlike those reported in many previous martian apatite study, as martian apatites are dominantly Cl-rich (Greenwood, 2005; Patino Douce and Roden, 2006; McCubbin and Nekvasil, 2008; Filiberto and Trieman, 2009; Patino Douce et al., 2011; McCubbin et al., 2013). However, as previously mentioned, recent studies conducted by Slaby et al. (2016; 2017) have found that primary F-rich apatites in martian meteorites is possible yet currently rare. The lack of F-rich apatites within our martian sample suite can possibly be attributed to the sample bias of martian meteorites. F values in NWA 8159 range from 2.79-4.83 wt.%. However, the maximum F content in apatite allowed by stoichiometry is ~3.7 wt.% (Ruff, 2018). This indicates that an analytical error may have occurred during SEM-EDS analysis. This high F content combined with the high totals (in excess of 101%, table 8) of the conducted analysis can be explained by the small size of the apatites (<20µm). SEM-EDS analysis is difficult to conduct on small grains, as there is a higher likelihood that matrix material will be incorporated into your data.

However it is possible that the observed F enrichment could be explained by terrestrial contamination, which has occurred in NWA 8159 (Agee et al., 2014a; Agee et al., 2014b). Since SEM-EDS analysis is difficult to conduct on small grains, as previously mentioned, the resulting analysis will not accurately represent the chemistry of the apatite. Since matrix material is more prone to terrestrial contamination it is possible the matrix of NWA 8159 has been altered. The matrix of NWA 8159 was analysed using SEM-EDS (table 9). The analyses indicated the matrix was F-poor. However, since only two measurements of the matrix were conducted, an F-rich matrix source cannot be completely ruled out as a factor in F-enrichment of apatite. Fluorite formation, associated with some evaporates, can occur in the Northwest Africa desert environment, which could produce a F-rich matrix (Deer et al., 1966; Glennie, 1987). If terrestrial alteration has occurred then it will have overprinted any original chemical information preserved within NWA 8159 apatites and therefore cannot provide insight into the volatile abundances of the parental source region for this meteorite, resulting in F-rich apatites that are not representative of Mars. However, if NWA 8159 apatites had been terrestrially altered, the associated sulphides would have shown signs of alteration also as sulphides are more susceptible to alteration than apatite (Hallis and Taylor, 2011). From the data, it is difficult to determine whether the F-enrichment is martian or terrestrial.

5.3 Hydrogen Isotope Results from NWA 7034

5.3.1 Factors Affecting Deuterium/Hydrogen Ratios

Multiple factors such as; crustal material assimilation; terrestrial contamination/weathering; hydrogen degassing; spallation by cosmic rays; and shock pressures have been found to effect the D/H ratio within minerals (Hallis et al., 2012). These factors can all affect the interpretation of D/H ratios in martian meteorites, meaning most martian meteorites do not record a martian mantle signal ($\delta D < 275\text{‰}$) and instead tend to contain crustal/atmospheric values (Hallis et al., 2012; Usui et al., 2012).

Martian meteorites experience high shock pressures when they are ejected from Mars, which can disturb their natural D/H ratio. Shock devolatilization (loss of H due to it being the lighter isotope and therefore preferentially lost) has been proven to decrease the water content and thus increasing the D/H ratio of a given mineral. Hallis (2017) highlighted a trend between increasing δD and decreasing water content within apatites in the Shergottites and ALH 84001, which implies hydrogen degassing. Whereas apatite within the nakhlites contain highly varied water contents with consistently low δD values, which likely represent a martian mantle signature.

5.3.2 Apatite Groupings

The hydrogen isotope data indicates three distinct groups of apatite in NWA 7034: Group 1 (high δD and low water content); Group 2 (intermediate δD and high water content); Group 3 (low δD and high water content).

Group 1, characterised by a high δD and a low water content (table 12), could be the result of shock effects. During shock, H is lost as a result of devolatilisation (Hallis et al., 2012, 2017). Therefore, loss of H would decrease the water content. It would also increase the D/H ratio of the apatites, due to the preferential loss of the lighter hydrogen isotope, resulting in the high δD values recorded in this study. Alternatively, devolatilisation may have occurred as a result of thermal alteration (possibly the thermal event inferred by McCubbin et al. (2016) at ~ 1.5 Ga. Evidently, devolatilisation has occurred in Group 1. The mechanism that caused this devolatilisation is hard to constrain since NWA 7034 has experienced both shock and thermal heating. A combination of both shock and thermal heating is also possible.

Group 2 is characterised by intermediate δD values and high water contents. Despite the pit in ROI_7 possibly incorporating matrix into the analysis, the other pits from this group (ROI_1 and 2) are uncontaminated. Therefore, since ROI_7 displays similar values to those from ROI_1 and 2 (table 12) it is likely that the analysis from ROI_7 is not significantly affected by matrix contamination, and is thus a representative measurement of Group 2 apatite. By comparing the δD and water contents values of each group (figure 41), it can be concluded that despite the fact that Group 2 have intermediate δD values, it is not a mix of Group 1 and Group 3. If Group 2 were a mix of Group 1 and Group 3, these apatites would exhibit an intermediate water content, which is not the case. The values exhibited by this group are unlikely to have resulted from thermal alteration as devolatilisation typically lowers water content.

A likely explanation for the intermediate δD values and high water contents displayed by this group is hydrothermal alteration. The dominant textural type in Group 2 is spongy (with the exception of ROI_7 having an anhedral texture), whereas the texture of apatite in Groups 1 and 3 is predominantly euhedral. Therefore, the spongy texture of Group 2 apatites may be a direct result of hydrothermal alteration or deposition by a fluid with, an intermediate δD value. McCubbin et al. (2016) previously provided evidence for hydrothermal alteration from a protobreccia clast within NWA 7034. The timing of the hydrothermal alteration was inferred to have occurred before the protobreccia clasts were incorporated into the matrix of NWA 7034.

Group 3 is dominated by low δD values and high water contents. It is important to note that both apatite grains within this grouping are from the epoxy mounted sample. Therefore, possible epoxy contamination to this group has to be evaluated. The pit image collected from ROI_3 (figure 34) indicates that the beam penetrated the matrix during hydrogen isotope analysis. However, the pit of ROI_3 did not visibly include matrix material, and yields δD values and water contents very similar to ROI_5. Hydrogen isotope measurements from a pyroxene in NWA 7034(Epoxy) display a δD value of $-98.02 \pm 88\%$ and a low water content of 190.20 ± 10 ppm, suggesting that degassing of hydrogen from epoxy did not have a significant effect on the analysis of apatites within Group 3. High water contents and low δD values are diagnostic of terrestrial contamination. However, this hypothesis is difficult to fully determine due to the extent of terrestrial contamination in NWA 7034 being unknown and with no D/H datasets available for other hydrous minerals or glass within the sample to compare with.

Alternatively, the low δD values and high water contents observed in the group are possibly a martian mantle signal, as the martian mantle displays low $\delta D < 275\text{‰}$ values (Hallis et al., 2012; Usui et al., 2012). If this is the case, the high water content from this group implies that the parental melt in which the apatites came from had a high water content.

Both of these interpretations can be backed up by comparing the δD content with water content (figure 42) with conclusions based from Hallis (2017). When the data range of Group 3 (ROI_3: $\delta D = 51.72 \pm 82\text{‰}$, water content = $4307.96 \pm 80\text{ppm}$ and ROI_5: $\delta D = 52.10 \pm 82\text{‰}$, water content = $4677.33 \pm 90\text{ppm}$) is compared with apatites measured from Hallis et al. (2017), they plot within the orange region. The orange region on the plot indicates δD values similar to the martian mantle and terrestrial signatures ($< 275\text{‰}$). Therefore, it is difficult to determine whether the δD values observed in Group 3 are martian mantle or an effect of terrestrial alteration.

The three distinct groupings of apatite grains within the two NWA 7034 samples implies that the thermal event at ~ 1.5 Ga (McCubbin et al., 2016) did not completely overprint the volatile signatures within these apatites.

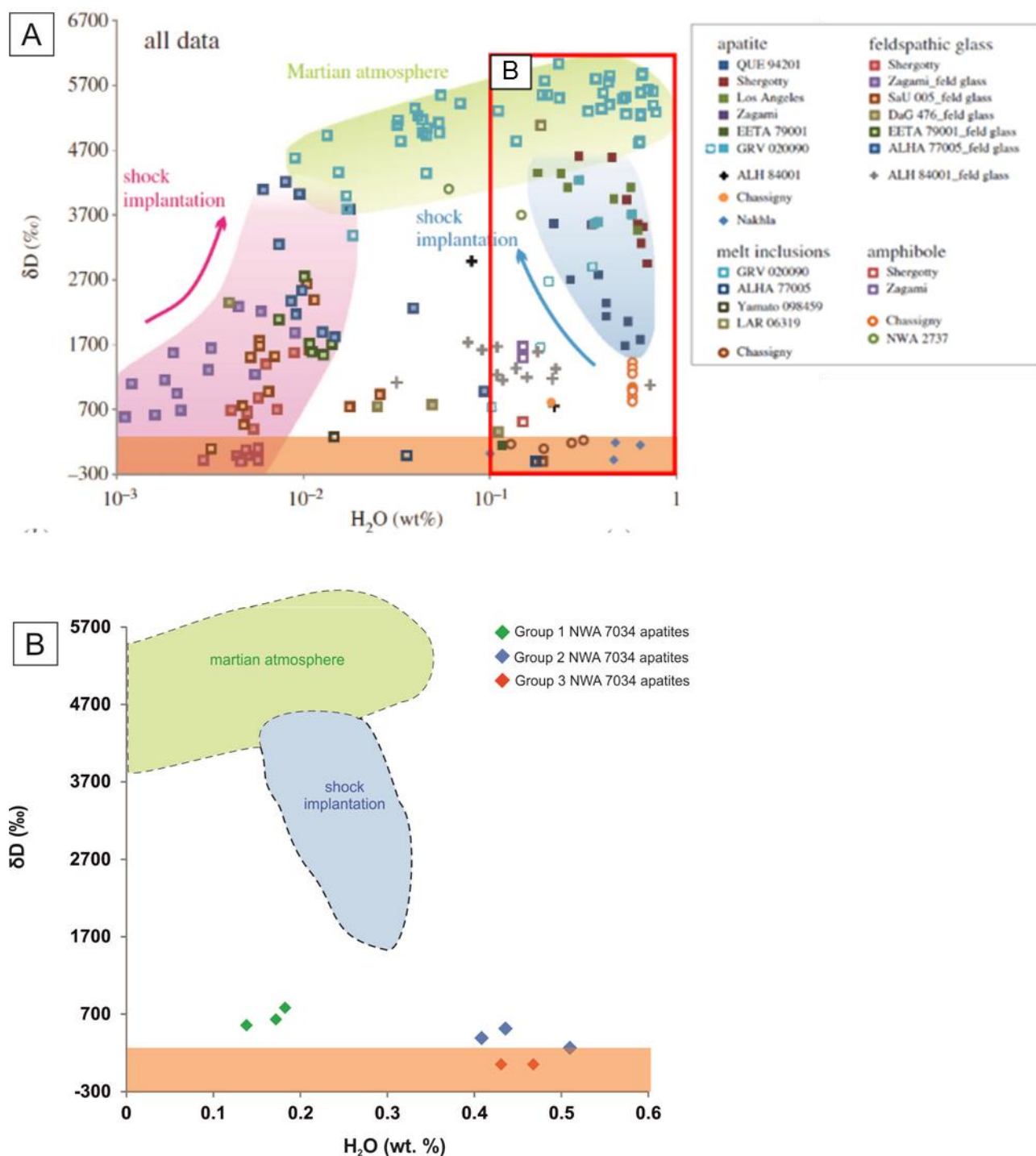


Figure 42: (A) The water content (H_2O wt. %) versus δD for apatites from Hallis et al. (2016) (see paper for the range of martian meteorites measured) and (B) apatite data from this study of NWA 7034. The orange region represents martian mantle and terrestrial values (i.e., $<275\text{‰}$). Group 3 apatites all plot within this orange region, indicating that they record either martian mantle or terrestrial signatures. Group 1 apatites all plot above the orange region, indicating shock implantation of hydrogen. Most of Group 2 apatites plot above the orange region, however ROI_2 partially falls into it. This may suggest some terrestrial contamination in this apatite.

5.3.3 *Effect of Terrestrial Contamination*

Terrestrial lowering of originally high δD values from all apatites in NWA 7034 is unlikely to be an influencing factor for this data. Despite NWA 7034 experiencing terrestrial alteration, apatite is a structurally robust mineral and therefore, is less effected by terrestrial alteration compared to matrix material. If all the values had been terrestrially lowered, groupings of apatites with similar δD values would not be expected, as the terrestrial environment would have lowered them at differing rates creating highly varied results with no distinct correlation. Therefore, it is likely that the δD values collected in this study are martian signatures.

However, high water contents and low δD values are diagnostic of terrestrial contamination, thus in Group 3 terrestrial contamination may have been an influencing factor. This hypothesis is difficult to fully determine due to the extent of terrestrial contamination in NWA 7034 being unknown and with no D/H datasets available from other hydrous minerals or glass within the sample to compare with.

5.3.4 *Deuterium/Hydrogen Values from Anhydrous Minerals in NWA 7034*

Hydrogen isotope analysis conducted on two pyroxene grains from NWA 7034(In and Epoxy) yielded δD values of -136.14‰ and -98.02‰ and water contents of 465.62 ppm and 190.20 ppm respectively (table 11). It is unusual that a pyroxene mounted in indium displays a higher water content than a pyroxene mounted in epoxy as indium mounts usually restrict water contamination to the sample. Generally, epoxy mounted samples tend to yield higher water contents for anhydrous minerals, as epoxy degassing can be a problem in the high vacuum sample chamber of the SIMS.

The pit image from NWA 7034(In) (figure 38) indicates that no matrix material was incorporated into the analysis. Therefore, the elevated water content cannot be attributed to a contaminated analysis. The indium mounted pyroxene was loaded and analysed at the end of a day, thus the high vacuum in the ion microprobe may have not reached similar levels as the vacuum that the epoxy mounted pyroxene was measured under. This could explain the higher water content of the indium mounted pyroxene. Alternatively, as mentioned in section 4.3.2 the two pyroxenes within this polymict breccia could actually have two different water contents.

Chapter 6 Conclusions

6.1 Summary

The presence of water within our Solar System, is a primary focus in planetary science due to the astrobiological significance of this compound. Mars is a prime candidate to find water as recent Mars orbiter and lander missions have revealed evidence for the presence of liquid water early in Mars's history in the form of geomorphological features (e.g., fluvial valleys), water rich sediments and minerals (e.g. clays) and evaporates (e.g. gypsum). Studying water rich martian meteorites such as NWA 7034, via hydrogen isotope analysis, helps determine how much water was on the surface of Mars in the past and the source of that water (e.g., parental melt water sourced from the Martian interior, crustal water sourced from the cryosphere or atmospheric water). Understanding the physical state of surficial water on Mars throughout its history is crucial in interpreting how Mars's climate evolved and whether life had the potential to flourish in these climates (McCubbin et al., 2012). Furthermore, investigating water rich martian meteorites aids in the understanding of the role of water during the formation of the Solar System- late accreted veneer versus wet planetary building blocks.

The discovery of both NWA 7034 and NWA 8159 has undoubtedly expanded the diversity of the martian meteorites beyond the common SNC types. Studying these unique meteorites gives great insight into previously unseen rock types present at the martian surface and allows for a more detailed understanding of martian geology to be determined.

Cl-rich apatites, with a significant OH component were found in NWA 7034, both through stoichiometry and in situ hydrogen isotope analysis. Hydrogen isotope data collected for this study exhibits δD values between 51.72‰-782.47‰ (table 11). Three distinct groupings of apatites can be noted on the basis of δD , water content and texture of apatite. This implies that there are at least two different apatite histories that have been recorded. Group 1 is characterised by high δD values paired with low water contents, and inferred to be the result of devolatilisation during shock and/or thermal heating. Group 2 consists of intermediate δD values and high water contents, which could be controlled by hydrothermal alteration. Group 3 is characterised by low δD values and high water contents, probably caused by terrestrial contamination, but possibly representative of a martian mantle signature.

The discovery of F-rich apatites in NWA 8159 in this study is a particularly important find since F-rich apatites, are not characteristic of martian meteorites. This rare finding along with previous F-rich apatite discoveries (Slaby et al., 2016, 2017) highlights that a F-rich source region for martian magma is present. This F-rich parental source region has, until recently, been unstudied due to the sample bias in the martian meteorite suite. However, this finding is significant and highlights that Mars is more geochemically complex than previously thought.

The observed F-enrichment of apatites in NWA 8159 could be either martian or an effect of terrestrial contamination. More high-resolution data needs to be collected to determine the origin of the F-enrichment in NWA 8159.

6.2 Future Work

6.2.1 Northwest Africa 7034

Additional hydrogen isotope analysis should be conducted on NWA 7034 apatites to see if the 3 groupings discovered in this study are consistent throughout the whole meteorite or if more groups/variations exist.

Group 2 apatites need to be further investigated to see if they contain signs of hydrothermal alteration at a submicron level. The only textural evidence for these apatites experiencing hydrothermal alteration is their spongy appearance compared to other apatites within NWA 7034. Definitive submicron evidence of hydrothermal alteration would strengthen the notion that Group 2 apatites experienced hydrothermal alteration prior to incorporation into NWA 7034.

The full extent of terrestrial contamination in Group 3 is difficult to fully determine due to the extent of terrestrial contamination in NWA 7034 being unknown and with no D/H datasets available to compare with. Studies should aim to attain δD values from other hydrous phases in NWA 7034 to determine if any show terrestrial contamination values (i.e., low δD and high water content) as if they do it may explain the values exhibited by Group 3.

All of the above would strengthen the interpretation of NWA 7034's petrogenesis and give a more valuable insight into the histories of apatites prior to incorporation into the NWA 7034 breccia.

6.2.2 Northwest Africa 8159

It would be beneficial for future work to be conducted on NWA 8159, as little is known about this unique martian meteorite. An Amazonian age of NWA 8159 2.37 ± 0.25 Ga (Herd et al., 2017) has not been previously represented in other martian meteorites therefore this meteorite contains valuable information on processes occurring late in Mars' history.

From the data, it is difficult to determine whether the F-enrichment present with apatite grains is martian or terrestrial and therefore high-resolution studies such as transmission electron microscopy are needed to confirm the origin of the enrichment.

Gaining hydrogen isotope compositions of NWA 8159 apatites has the potential to yield information on the water content of this meteorite, as it is currently unknown. Hydrogen isotope analysis could also possibly confirm the extent of terrestrial contamination in this meteorite.

References

Agee, C. B., Wilson, N., McCubbin, F., Ziegler, K., Polyak, V., Sharp, Z., Asmerom, Y., Nunn, M., Shaheen, R., Thiemens, M., Steele, A., Fogel, M., Bowden, R., Glamoclija, M., Zhang, Z. and Elardo, S. (2013). Unique Meteorite from Early Amazonian Mars: Water- Rich Basaltic Breccia Northwest Africa 7034. *Science*, 339(6121), pp.780-785.

Agee, C. B., Muttik, N., Ziegler, K., McCubbin F. M., Herd, C. D. K., Rocheete, P. and Gattacceca, J. (2014a). Discovery of a New Martian Meteorite Type: Augite Basalt-Northwest Africa 8159. *45th Lunar and Planetary Science Conference*, abstract # 2036.

Agee, C. B., Muttik, N., Ziegler, K., Walton, E. L., Herd, C. D. K., McCubbin, F. M.,

Sanots, A. R., Burger, P. V., Simon, J. I., Peters, T. J., Tappa, M. J., Sanborn, M. E. and Yin, Q. Z. (2014b). New Meteorite Type NWA 8159 Augite Basalt: Specimen From A Previously Unsampled Location on Mars. *77th Annual Meteoritical Society Meeting*, abstract # 5397.

Alexander, C.M.O.D., Bowden, R., Fogel, M.L., Howard, K.T., Herd, C.D.K. and Nittler, L.R. (2012). The provenances of asteroids, and their contributions to the volatile inventories of the terrestrial planets. *Science*, (377), pp. 721-723.

Aoki, K., Ishiwaka, K. and Kanisawa, S. (1981). Fluorine geochemistry of basaltic rocks from continental and oceanic regions and petrogenetic application. *Contributions to Mineralogy and Petrology*, 76(1), pp.53-59.

Aoudjehane, H., Avice, G., Barrat, J., Boudouma, O., Chen, G., Duke, M., Franchi, I., Gattacceca, J., Grady, M., Greenwood, R., Herd, C., Hewins, R., Jambon, A., Marty, B., Rochette, P., Smith, C., Sautter, V., Verchovsky, A., Weber, P. and Zanda, B. (2012). Tissint Martian Meteorite: A Fresh Look at the Interior, Surface, and Atmosphere of Mars. *Science*, 338(6108), pp.785-788.

Baziotis, I. P., Liu, Y., DeCarli, P. S., Melosh, H. J., McSween, H. Y., Bodnar, R. J. and Taylor, L. A. (2013). The Tissint Martian meteorite as evidence for the largest impact excavation. *Nature Communication*, 4(1404).

Bogard, D. and Johnson, P. (1983). Martian Gases in an Antarctic Meteorite? *Science*, 221(4611), pp.651-654.

Borg, L., Nyquist, L., Taylor, L., Wiesmann, H. and Shih, C. (1997). Constraints on Martian differentiation processes from Rb Sr and Sm Nd isotopic analyses of the basaltic shergottite QUE 94201. *Geochimica et Cosmochimica Acta*, 61(22), pp.4915-4931.

Borg, L. and Draper, D. (2003). A petrogenetic model for the origin and compositional variation of the Martian basaltic meteorites. *Meteoritics & Planetary Science*, 38(12), pp.1713-1731.

Borg, L. and Drake, M. J. (2005). A review of meteorite evidence for the timing of magmatism and of surface or near-surface liquid water on Mars. *Journal of Geophysical Research*, 110(E12).

Boyce, J., Tomlinson, S., McCubbin, F., Greenwood, J. and Treiman, A. (2014). The Lunar Apatite Paradox. *Science*, 344(6182), pp.400-402.

Brownlow, A. (1996). *Geochemistry*. New Jersey: Prentice Hall.

Cartwright, J., Ott, U., Herrmann, S. and Agee, C. (2014). Modern atmospheric signatures in 4.4 Ga Martian meteorite NWA 7034. *Earth and Planetary Science Letters*, 400, pp.77-87.

Clayton, R. and Mayeda, T. (1996). Oxygen isotope studies of achondrites. *Geochimica et Cosmochimica Acta*, 60(11), pp.1999-2017.

Day, J., Taylor, L., Floss, C. and Mccween, H. (2006). Petrology and chemistry of MIL 03346 and its significance in understanding the petrogenesis of nakhlites on Mars. *Meteoritics & Planetary Science*, 41(4), pp.581-606.

Deer, W., Howie, R. and Zussman, J. (1992). *An introduction to the rock-forming minerals*. Harlow: Longman. pp.663-680.

Filiberto, J. and Treiman, A. (2009). Martian magmas contained abundant chlorine, but little water. *Geology*, 37(12), pp.1087-1090.

Filiberto, J., Gross, J. and McCubbin, F. (2016). Constraints on the water, chlorine, and fluorine content of the Martian mantle. *Meteoritics & Planetary Science*, 51(11), pp.2023-2035.

Fisher, D. (2007). Mars' water isotope (D/H) history in the strata of the North Polar Cap: Inferences about the water cycle. *Icarus*, 187(2), pp.430-441.

Franchi, I., Wright, I., Sexton, A. and Pillinger, C. (1999). The oxygen-isotopic composition of Earth and Mars. *Meteoritics & Planetary Science*, 34(4), pp.657-661.

Glennie K. W. (1987). Desert sedimentary environments, present and past: A summary. *Sedimentary Geology*, 50, pp.135–165.

Goderis, S., Brandon, A., Mayer, B. and Humayun, M. (2016). Ancient impactor components preserved and reworked in martian regolith breccia Northwest Africa 7034. *Geochimica et Cosmochimica Acta*, 191, pp.203-215.

Gooding, J., Wentworth, S. and Zolensky, M. (1991). Aqueous alteration of the Nakhla meteorite. *Meteoritics*, 26(2), pp.135-143.

Greenwood, J., Blake, R. and Coath, C. (2003). Ion microprobe measurements of $^{18}\text{O}/^{16}\text{O}$ ratios of phosphate minerals in the Martian meteorites ALH84001 and Los Angeles. *Geochimica et Cosmochimica Acta*, 67(12), pp.2289-2298.

Greenwood, J. P. (2005) Chlorine-rich apatites in SNCs: Evidence for magma-brine interactions on Mars? *Meteoritics and Planetary Science* (40).

Greenwood, J., Itoh, S., Sakamoto, N., Vicenzi, E. and Yurimoto, H. (2008). Hydrogen isotope evidence for loss of water from Mars through time. *Geophysical Research Letters*, 35(5).

Gross, J., Filiberto, J. and Bell, A. (2013). Water in the martian interior: Evidence for terrestrial MORB mantle-like volatile contents from hydroxyl-rich apatite in olivine–phyric shergottite NWA 6234. *Earth and Planetary Science Letters*, 369-370, pp.120-128.

Hallis, L. and Taylor, G. (2011). Comparisons of the four Miller Range nakhlites, MIL 03346, 090030, 090032 and 090136: Textural and compositional observations of

primary and secondary mineral assemblages. *Meteoritics & Planetary Science*, 46(12), pp.1787-1803.

Hallis, L., Taylor, G., Nagashima, K. and Huss, G. (2012a). Magmatic water in the martian meteorite Nakhla. *Earth and Planetary Science Letters*, 359-360, pp.84-92.

Hallis, L., Taylor, G., Nagashima, K., Huss, G., Needham, A., Grady, M. and Franchi, I. (2012b). Hydrogen isotope analyses of alteration phases in the nakhlite martian meteorites. *Geochimica et Cosmochimica Acta*, 97, pp.105-119.

Hallis, L. (2013). Alteration assemblages in the Miller Range and Elephant Moraine regions of Antarctica: Comparisons between terrestrial igneous rocks and Martian meteorites. *Meteoritics & Planetary Science*, 48(2), pp.165-179.

Hallis, L., Huss, G., Nagashima, K., Taylor, G., Halldorsson, S., Hilton, D., Mottl, M. and Meech, K. (2015). Evidence for primordial water in Earth's deep mantle. *Science*, 350(6262), pp.795-797.

Hallis, L. J., Simpson, S., Mark, D. And Lee., M. R. (2016). Martian Alteration in Unique Meteorite NWA 8159? *79th Annual Meeting of the Meteoritical Society*, abstract # 6422.

Hallis, L. (2017). D/H ratios of the inner Solar System. *Philosophical Transactions of the Royal Society A: Mathematical, Physical and Engineering Sciences*, 375(2094).

Harlov, D. (2015). Apatite: A Fingerprint for Metasomatic Processes. *Elements*, 11(3), pp.171-176.

Henderson, C. E. (2011). Protocols and Pitfalls of Electron Microprobe Analysis of Apatite, Master of Science in Geology, The University of Michigan.

Herd, C., Borg, L., Jones, J. and Papike, J. (2002). Oxygen fugacity and geochemical variations in the martian basalts: implications for martian basalt petrogenesis and the oxidation state of the upper mantle of Mars. *Geochimica et Cosmochimica Acta*, 66(11), pp.2025-2036.

Herd, C. (2003). The oxygen fugacity of olivine-phyric martian basalts and the components within the mantle and crust of Mars. *Meteoritics & Planetary Science*, 38(12), pp.1793-1805.

Herd, C., Walton, E., Agee, C., Muttik, N., Ziegler, K., Shearer, C., Bell, A., Santos, A., Burger, P., Simon, J., Tappa, M., McCubbin, F., Gattacceca, J., Lagroix, F., Sanborn, M., Yin, Q., Cassata, W., Borg, L., Lindvall, R., Kruijjer, T., Brennecka, G., Kleine, T., Nishiizumi, K. and Caffee, M. (2017). The Northwest Africa 8159 martian meteorite: Expanding the martian sample suite to the early Amazonian. *Geochimica et Cosmochimica Acta*, 218, pp.1-26.

Higp.hawaii.edu. (2017). *HIGP/W. M. Keck Cosmochemistry Laboratory Ion Microprobe-Facility Description*. [online] Available at: <https://www.higp.hawaii.edu/cosmochemistry/labdesc.html> [Accessed 13 Sep. 2017].

Howarth, G., Pernet-Fisher, J., Bodnar, R. and Taylor, L. (2015). Evidence for the exsolution of Cl-rich fluids in Martian magmas: Apatite petrogenesis in the enriched lherzolithic Shergottite Northwest Africa 7755. *Geochimica et Cosmochimica Acta*, 166, pp.234-248.

Hughes, J. and Rakovan, J. (2015). Structurally Robust, Chemically Diverse: Apatite and Apatite Supergroup Minerals. *Elements*, 11(3), pp.165-170.

Humayun, M., Nemchin, A., Zanda, B., Hewins, R., Grange, M., Kennedy, A., Lorand, J., Göpel, C., Fieni, C., Pont, S. and Deldicque, D. (2013). Origin and age of the earliest Martian crust from meteorite NWA 7533. *Nature*, 503(7477), pp.513-516.

Hutchison, R. (2004). *Meteorites*. Cambridge, UK: Cambridge University Press.

Jakosky, B. and Jones, J. (1997). The history of Martian volatiles. *Reviews of Geophysics*, 35(1), pp.1-16.

Jambon, A., Déruelle, B., Dreibus, G. and Pineau, F. (1995). Chlorine and bromine abundance in MORB: the contrasting behaviour of the Mid-Atlantic Ridge and East Pacific Rise and implications for chlorine geodynamic cycle. *Chemical Geology*, 126(2), pp.101-117.

Kayzar, T. M., Borg, L., Kruijjer, T. S., Kleine, T., Brennecka, G. and Agee, C. (2015). Neodymium and Tungsten Isotope Systematics of Mars Inferred from the Augite Basaltic Meteorite NWA 8159. *46th Lunar and Planetary Science Conference*, abstract # 2357.

Kurokawa, H., Sato, M., Ushioda, M., Matsuyama, T., Moriwaki, R., Dohm, J. and Usui, T. (2014). Evolution of water reservoirs on Mars: Constraints from hydrogen isotopes in martian meteorites. *Earth and Planetary Science Letters*, 394, pp.179-185.

Lancet, M. and Lancet, K. (1971). Cosmic-ray and gas-retention ages of the Chassigny meteorite. *Meteoritics*, 6(2), pp.81-85.

Lentz, R., Taylor, G. and Treiman, A. (1999). Formation of a martian pyroxenite: A comparative study of the nakhlite meteorites and Theo's Flow. *Meteoritics & Planetary Science*, 34(6), pp.919-932.

Leshin, L., Epstein, S. and Stolper, E. (1996). Hydrogen isotope geochemistry of SNC meteorites. *Geochimica et Cosmochimica Acta*, 60(14), pp.2635-2650.

Lin, Y. T., Hu, S. and Zhang, T. (2016). U-Pb Dating of Zircon with Petrographic Settings from the Martian Regolith Breccia NWA 7034. *79th Annual Meeting of the Meteoritical Society*, abstract # 6248.

Lodders, K. (1997). An Oxygen Isotope Model for the Composition of Mars. *Icarus*, 126(2), pp.373-394. Martian Meteorite Compendium (2017). *Martian Meteorite Compendium*. [online] Curator. jsc.nasa.gov. Available at: <https://curator.jsc.nasa.gov/antmet/mmc/> [Accessed 14 Sep. 2017].

Mathez, E. and Webster, J. (2005). Partitioning behaviour of chlorine and fluorine in the system apatite-silicate melt-fluid. *Geochimica et Cosmochimica Acta*, 69(5), pp.1275- 1286.

McConnell, D. (1973). Apatite; its crystal chemistry, mineralogy, utilization, and geologic and biologic occurrences. *New York: Springer-Verlag*.

McCubbin, F. and Nekvasil, H. (2008). Maskelynite-hosted apatite in the Chassigny meteorite: Insights into late-stage magmatic volatile evolution in martian magmas. *American Mineralogist*, 93(4), pp.676-684.

McCubbin, F., Steele, A., Hauri, E., Nekvasil, H., Yamashita, S. and Hemley, R. (2010). Nominally hydrous magmatism on the Moon. *Proceedings of the National Academy of Sciences*, 107(25), pp.11223-11228.

McCubbin, F., Jolliff, B., Nekvasil, H., Carpenter, P., Zeigler, R., Steele, A., Elardo, S. and Lindsley, D. (2011). Fluorine and chlorine abundances in lunar apatite: Implications for heterogeneous distributions of magmatic volatiles in the lunar interior. *Geochimica et Cosmochimica Acta*, 75(17), pp.5073-5093.

McCubbin, F., Hauri, E., Elardo, S., Vander Kaaden, K., Wang, J. and Shearer, C. (2012). Hydrous melting of the martian mantle produced both depleted and enriched shergottites. *Geology*, 40(8), pp.683-686.

McCubbin, F., Elardo, S., Shearer, C., Smirnov, A., Hauri, E. and Draper, D. (2013). A petrogenetic model for the comagmatic origin of chassignites and nakhlites: Inferences from chlorine-rich minerals, petrology, and geochemistry. *Meteoritics & Planetary Science*, 48(5), pp.819-853.

McCubbin, F., Vander Kaaden, K., Tartèse, R., Boyce, J., Mikhail, S., Whitson, E., Bell, A., Anand, M., Franchi, I., Wang, J. and Hauri, E. (2015a). Experimental investigation of F, Cl, and OH partitioning between apatite and Fe-rich basaltic melt at 1.0–1.2 GPa and 950–1000 °C. *American Mineralogist*, 100(8-9), pp.1790-1802.

McCubbin, F. and Jones, R. (2015b). Extraterrestrial Apatite: Planetary Geochemistry to Astrobiology. *Elements*, 11(3), pp.183-188.

McCubbin, F., Vander Kaaden, K., Tartèse, R., Boyce, J., Mikhail, S., Whitson, E., Bell, A., Anand, M., Franchi, I., Wang, J. and Hauri, E. (2015c). Experimental investigation of F, Cl, and OH partitioning between apatite and Fe-rich basaltic melt at 1.0–1.2 GPa and 950–1000 °C. *American Mineralogist*, 100(8-9), pp.1790-1802.

McCubbin, F., Boyce, J., Novák-Szabó, T., Santos, A., Tartèse, R., Muttik, N., Domokos, G., Vazquez, J., Keller, L., Moser, D., Jerolmack, D., Shearer, C., Steele, A., Elardo, S., Rahman, Z., Anand, M., Delhaye, T. and Agee, C. (2016). Geologic history of Martian regolith breccia Northwest Africa 7034: Evidence for hydrothermal activity and lithologic diversity in the Martian crust. *Journal of Geophysical Research: Planets*, 121(10), pp.2120-2149.

McSween, H. (1984). SNC meteorites: Are they Martian rocks? *Geology*, 12(1), p.3.

McSween, H. (1994). What we have learned about Mars from SNC meteorites. *Meteoritics*, 29(6), pp.757-779.

McSween, H., Taylor, G. and Wyatt, M. (2009). Elemental Composition of the Martian Crust. *Science*, 324(5928), pp.736-739.

Muttik, N., McCubbin, F., Keller, L., Santos, A., McCutcheon, W., Provencio, P., Rahman, Z., Shearer, C., Boyce, J. and Agee, C. (2014). Inventory of H₂O in the ancient Martian regolith from Northwest Africa 7034: The important role of Fe oxides. *Geophysical Research Letters*, 41(23), pp.8235-8244.

National Geographic (2017). *Martian Meteorites*. [online] National Geographic Society. Available at: <https://www.nationalgeographic.org/media/martian-meteorites-wbt/> [Accessed 14 Sep. 2017].

Oxford-labs.com. (2017). *Oxford Labs - X-ray fluorescent analysis*. [online] Available at: <http://oxford-labs.com/> [Accessed 13 Sep. 2017].

Papike, J., Karner, J., Shearer, C. and Burger, P. (2009). Silicate mineralogy of Martian meteorites. *Geochimica et Cosmochimica Acta*, 73(24), pp.7443-7485.

Patiño Douce, A. and Roden, M. (2006). Apatite as a probe of halogen and water fugacities in the terrestrial planets. *Geochimica et Cosmochimica Acta*, 70(12), pp.3173-3196.

Patiño Douce, A., Roden, M., Chaumba, J., Fleisher, C. and Yogodzinski, G. (2011). Compositional variability of terrestrial mantle apatites, thermodynamic modeling of apatite volatile contents, and the halogen and water budgets of planetary mantles. *Chemical Geology*.

Peres, P., Chambost, E. and Schuhmacher, M. (2008). CAMECA IMS 7f-GEO: Specialized SIMS tool for geosciences. *Applied Surface Science*, 255(4), pp.1472-1475.

Podosek, F. (1973). Thermal history of the nakhlites by the ⁴⁰Ar-³⁹Ar method. *Earth and Planetary Science Letters*, 19(2), pp.135-144.

Pyle, J., Spear, F. and Wark, D. (2002). Electron Microprobe Analysis of REE in Apatite, Monazite and Xenotime: Protocols and Pitfalls. *Reviews in Mineralogy and Geochemistry*, 48(1), pp.337-362.

Reed, S. (2010). *Electron microprobe analysis and scanning electron microscopy in geology*. Cambridge: Cambridge University Press.

Rmets.org. (2013). *Royal Meteorological Society*. [online] Available at: <https://www.rmets.org/> [Accessed 13 Sep. 2017].

Robinson, L. (2000). *Revision Notes for Higher Physics*. 1st ed. East Kilbride: Chemcord Inch Keith.

Romanek, C., Grady, M., Wright, I., Mittlefehldt, D., Socki, R., Pillinger, C. and Gibson, E. (1994). Record of fluid–rock interactions on Mars from the meteorite ALH84001. *Nature*, 372(6507), pp.655-657.

Rruff.info. (2018). *Doclib - RRUFF Database: Raman, X-ray, Infrared, and Chemistry*. [online] Available at: <http://rruff.info/doclib/hom/fluorapatite.pdf>. [Accessed 15 Feb. 2018].

Santos., A. R., Agee, C. B., McCubbin, F. M., Shearer, C. K., Burger, P. V., Sharp, Z. D. and Zimmer, M. (2013). Apatite and Merrillite from Martian Meteorite NWA 7034. *44th Lunar and Planetary Science Conference*, abstract # 2601.

Santos, A., Agee, C., McCubbin, F., Shearer, C., Burger, P., Tartèse, R. and Anand, M. (2015). Petrology of igneous clasts in Northwest Africa 7034: Implications for the petrologic diversity of the martian crust. *Geochimica et Cosmochimica Acta*, 157, pp.56-85.

Sarbadhikari, A. B., Day, J., Liu, Y., Rumble, D. and Taylor, L. (2009). Petrogenesis of olivine-phyric shergottite Larkman Nunatak 06319: Implications for enriched components in martian basalts. *Geochimica et Cosmochimica Acta*, 73(7), pp.2190-2214.

Sarbadhikari, A. B., Goodrich, C., Liu, Y., Day, J. and Taylor, L. (2011). Evidence for heterogeneous enriched shergottite mantle sources in Mars from olivine-hosted melt inclusions in Larkman Nunatak 06319. *Geochimica et Cosmochimica Acta*, 75(22), pp.6803- 6820.

SERC. (2017). *SERC*. [online] Available at: <https://serc.carleton.edu/index.html> [Accessed 13 Sep. 2017].

Sharp, T. G., Walton, E. L., and Hu, J. (2015). Shock effects in NWA 8159: Evidence for a modest shock pressure and a large impacting body. *45th Lunar Planet. Science Conference*, abstract #1939

Shearer, C. K., Bell, A. S., Burger, P. V., McCubbin, F. M., Agee, C., Simon, J. and Papike, J. J. (2015). The mineralogical record of fO_2 variation and alteration in Northwest Africa 8159 (NWA 8159). Evidence for the interaction between a mantle derived Martian basalt and a crustal component(s). *46th Lunar and Planetary Science Conference*, abstract #1483.

Simon, J. I., Peters, T. J., Tappa, M. J. and Agee, C. B. (2014). Northwest Africa 8159: An ~2.3 Billion Year Old Martian Olivine-Bearing Augite Basalt. *77th Annual Meeting of the Meteoritical Society*, abstract # 5363.

Słaby, E., Koch-Müller, M., Förster, H., Wirth, R., Rhede, D., Schreiber, A. and Schade, U. (2016). Determination of volatile concentrations in fluorapatite of Martian shergottite NWA 2975 by combining synchrotron FTIR, Raman spectroscopy, EMPA, and TEM, and inferences on the volatile budget of the apatite host-magma. *Meteoritics & Planetary Science*, 51(2), pp.390-406.

Słaby, E., Förster, H., Wirth, R., Giera, A., Birski, Ł. and Moszumańska, I. (2017). Validity of the Apatite/Merrillite Relationship in Evaluating the Water Content in the Martian Mantle: Implications from Shergottite Northwest Africa (NWA) 2975. *Geosciences*, 7(4), p.99.

Smith, M., Laul, J., Ma, M., Huston, T., Verkouteren, R., Lipschutz, M. and Schmitt, R. (1984). Petrogenesis of the SNC (shergottites, nakhlites, chassignites) meteorites: Implications for their origin from a large dynamic planet, possibly Mars. *Journal of Geophysical Research*, 89(S02), p.B612.

Stormer, J. C., Milton, J., Pierson, L. And Tacker, C. (1993). Variation of F and Cl X-ray intensity due to anisotropic diffusion in apatite during electron microprobe analysis. *American Mineralogist*, (78), pp. 641-648.

Summerson, I., Greshake, A., Fritz, J. and Reimold, U. (2013). High-pressure phases in a melt pocket within olivine macrocryst in the Tissint Martian meteorite. *44th Lunar and Planetary Science Conference*, abstract # 1974.

Swindle, T. D. and Olson, E. K. (2004). ^{40}Ar - ^{39}Ar studies of whole rock nakhlites: Evidence for the timing of formation and aqueous alteration on Mars. *Meteoritics and Planetary Science*, (39), pp. 755-766.

Symes, S., Borg, L., Shearer, C. and Irving, A. (2008). The age of the martian meteorite Northwest Africa 1195 and the differentiation history of the shergottites. *Geochimica et Cosmochimica Acta*, 72(6), pp.1696-1710.

Tartèse, R., M., McCubbin, F. M., Santos, A. R. and Delhaye, T. (2014). Zircons in Northwest Africa 7034: recorders of crustal evolution on Mars. *45th Lunar Planet. Science Conference*, abstract #2020.

Taylor S. R. and McLennan S. M. (2009). *Planetary Crusts: Their Composition, Origin, and Evolution*. Cambridge University Press, Cambridge.

Treiman, A. (1998). The history of Allan Hills 84001 revised: Multiple shock events. *Meteoritics & Planetary Science*, 33(4), pp.753-764.

Treiman, A., Gleason, J. and Bogard, D. (2000). The SNC meteorites are from Mars. *Planetary and Space Science*, 48(12-14), pp.1213-1230.

Usui, T., Alexander, C., Wang, J., Simon, J. and Jones, J. (2012). Origin of water and mantle–crust interactions on Mars inferred from hydrogen isotopes and volatile element abundances of olivine-hosted melt inclusions of primitive shergottites. *Earth and Planetary Science Letters*, 357-358, pp.119-129.

Usui, T., Alexander, C., Wang, J., Simon, J. and Jones, J. (2015). Meteoritic evidence for a previously unrecognized hydrogen reservoir on Mars. *Earth and Planetary Science Letters*, 410, pp.140-151.

Vaci, Z., Newsom, H. E., Agee, C. B., Brearley, A. J., Tschanuner, O. and Herd, C. D. K. (2016). Electron Probe Microanalysis, Micro X-Ray Diffraction, and Deuterium-Hydrogen Analysis of Hydrous Al-teration in Martian Meteorites Northwest Africa 10416 and 8159. *44th Lunar and Planetary Science Conference*, abstract # 2538.

Villanueva, G., Mumma, M., Novak, R., Kaufl, H., Hartogh, P., Encrenaz, T., Tokunaga, A., Khayat, A. and Smith, M. (2015). Strong water isotopic anomalies in the martian atmosphere: Probing current and ancient reservoirs. *Science*, 348(6231), pp.218-221.

Watson, L., Hutcheon, I., Epstein, S. and Stolper, E. (1994). Water on Mars: Clues from Deuterium/Hydrogen and Water Contents of Hydrous Phases in SNC Meteorites. *Science*, 265(5168), pp.86-90.

Webster, C. R. (2013) Isotope Ratios of H, C, and O in CO₂ and H₂O of the Martian Atmosphere. *Science*, 341(260), pp. 260-263.

Wood, C. A. and Ashwal, L. D. (1981). SNC meteorites: Igneous rocks from Mars? *Lunar and Planetary Institute*, pp.1359-1375.

Wright, S., Christensen, P. and Sharp, T. (2011). Laboratory thermal emission spectroscopy of shocked basalt from Lonar Crater, India, and implications for Mars orbital and sample data. *Journal of Geophysical Research*, 116(E9)